Modal-Based Design Techniques for Circular Quadruple-Ridged Flared Horn Antennas

by

Theunis Steyn Beukman

Dissertation presented for the degree of Doctor of Philosophy in Engineering at the University of Stellenbosch

Promoter: Prof. P. Meyer

Department of Electrical and Electronic Engineering

March 2015

Declaration

By submitting this dissertation, I declare that the entirety of the work contained therein is my own, original work, that I am the sole author thereof (save to the extent explicitly otherwise stated), that reproduction and publication thereof by Stellenbosch University will not infringe any third party rights and that I have not previously in its entirety or in part submitted it for obtaining any qualification.

Signed: _____ Date: _____

T.S. Beukman

Abstract

Keywords – Quadruple-Ridged Flared Horns, Ridged Waveguides, Ridge-Loaded Cylindrical Modes, Reflector Antenna Feeds, Ultra Wideband Antennas

This dissertation presents modal-based techniques for the effective systematic design of quadruple-ridged flared horns (QRFHs) as reflector feeds for radio astronomy applications.

A new excitation technique is proposed, consisting of a quadraxial line that terminates in the quad-ridges through the back lid of the QRFH, which allows for the integration with differential low-noise amplifiers. An equivalent circuit of this quadraxial feed is presented that allows fast synthesis of optimal feeding designs for QRFHs. In addition, the quadraxial feeding network suppresses higher-order modes significantly. The effect of eliminating these unwanted modes are investigated and the quadraxial feed is shown to outperform the coaxial feed in the known detrimental aspects of the QRFH – beamwidth narrowing for increased frequency, beamwidth variation over the upper bandwidth, high cross-polarisation levels, high co-polar sidelobes and variable phase centre – for the specific QRFH designs.

Ridge-loaded modes are analysed and a large number of cut-off frequencies presented which are unavailable in literature. The pure-mode excitation of the quadraxial feed allows more effective control over the modal content in the QRFH. This is exploited in a proposed design technique where the cut-off frequencies throughout the horn are used to synthesise the ridge taper profile, in order to achieve the desired modal distribution in the aperture.

The proposed feeding solution is compact and therefore is also attractive for use with cryo-coolers, typically employed with front-end electronics in telescopes for radio astronomy. A prototype was successfully manufactured and the mechanical implementation of the quadraxial feed proved to be much more simple than that of the conventional feed – consisting of a coaxial line realised within the thin ridges.

Opsomming

Sleutelwoorde – Viervoud Gerifte Oopgesperde Horings, Rifgolfleiers, Rifgelaaide Silindriese Modusse, Weerkaatser Antenne Voere, Ultrawyeband Antennes

Hierdie proefskrif stel modus gebasseerde tegnieke voor vir die effektiewe sistematiese ontwerp van viervoud gerifte oopgesperde horings (VGOHs) as weerkaatser voere vir radio astronomie toepassings.

'n Nuwe voertegniek word voorgestel, wat bestaan uit 'n kwadraksiale lyn wat termineer in die vier riwwe deur die agterkant van die VGOH, wat die integrasie met differensiële laeruis versterkers toelaat. 'n Ekwivalente stroombaan van hierdie kwadraksiale voer word aangebied vir die vinnige sintese van optimale voer ontwerpe vir VGOHs. Boonop onderdruk die kwadraksiale voer netwerk ook beduidend hoër orde modusse. Die effek van die uitskakeling van hierdie ongewensde modusse word ondersoek en die kwadraksiale voer oortref die gedrag van die koaksiale voer in die bekende nadelige aspekte van die VGOH – bundelwydte vernouing met toenemende frekwensie, bundelwydte variasie oor die boonste bandwydte, hoë kruispolarisasie vlakke, hoë kopolarisasie sybande en wisselvallige fase senter – vir die spesifieke VGOH ontwerpe.

Rifgelaaide modusse word geanaliseer en 'n groot aantal afsnyfrekwensies word aangebied wat nie beskikbaar is in literatuur nie. Die suiwermodus opwekking van die kwadraksiale voer bied meer effektiewe beheer oor die modusinhoud in die VGOH. Hierdie aspek word benut in 'n voorgestelde tegniek waar die afsnyfrekwensies deur die horing gebruik word om die rif tapsheid profiel te sintetiseer, sodat die gewensde modale distribusie in die stralingsvlak behaal word.

Die voorgestelde voer oplossing is kompak en daarom ook aantreklik vir die gebruik met krioverkoelers, wat tipies gebruik word met die voorkant elektronika in teleskope vir radio astronomie. 'n Prototipe was suksesvol vervaardig en die meganiese implimentasie van die kwadraksiale voer toon dat dit eenvoudiger is as met die gebruiklike koaksiale voer – wat bestaan uit 'n koaksiale lyn bewerkstellig binne die dun riwwe.

Acknowledgements

I would like to acknowledge the following persons and institutions for their support and contributions, without which this work would not have been possible.

- My Lord and Saviour Jesus Christ for His unfailing wisdom, favour and provision.
- My wife, Coba, for the immense understanding and love with which she continuously supported me.
- Prof. Petrie Meyer, my promoter, for his insight, advice and encouragement. He has been a true inspiration and mentor.
- Profs. Rob Maaskant and Marianna Ivashina for their insight, advice and the collaboration throughout this work. Their doors were always wide open to me and for that I'm very grateful.
- Dr. Dirk de Villiers for his advice and technical support. Without it this work would have taken much longer to complete.
- Oleg Iupikov and Carlo Bencivenni for their technical support – in particular Oleg's GRASP toolbox used in this work.
- Prof. Per-Simon Kildal and the rest of the antenna group for hosting me during my two research visits at Chalmers University of Technology.
- Wessel Croukamp for his advice and workmanship with the manufacturing of the prototype.
- My friends and family, in particular my parents, for being understanding in their support and encouragement.
- Everyone from the office for their advice and contributions over the past few years – David, Shamim, Dewald, Ryno, Shilong and Satyam.
- SKA South Africa and the NRF for the financial support.
- MIDPREP for the financial support of my last research visit.

Contents

List of Figures

List of Tables

Chapter 1

Introduction

1.1 Motivation and context for research

The Square Kilometre Array (SKA) project is an international collaboration to build the world's most sensitive telescope for radio astronomy. Different technologies are proposed for the different frequency bands ranging from 70 MHz to 20 GHz. For the frequencies above 350 MHz, reflector antenna systems are proposed that would consist of about 3000 units, with the first phase of development currently under way. In this phase the aim is to employ as many as 5 single-pixel feeds on each of the initial 256 reflector antennas, in order to cover a bandwidth from 350 MHz to 13.8 GHz [1].

There are significant drawbacks in using multiple feeds for such a large number of reflector systems – more power is required as each feed would have its own cryocooler and set of low-noise amplifiers (LNAs), and during observations only a single band could be covered. Thus, for the second phase it is envisaged to replace most or even all of these feeds with a minimum number of ultra-wide bandwidth feeds. This is an extremely difficult task as the requirements for each of the multiple SKA science cases are reliant on different feed performance metrics. To achieve all the required metrics over a bandwidth of more than an octave with a single feed has thus far proved a challenging task. Currently there are several wideband single-pixel feeds aimed at solving this. One such feed is the quadruple-ridged flared horn (QRFH).

The main advantage of using a QRFH compared with a classical (near-) octave horn is its large operational bandwidth – i.e. in the order of a 6:1 bandwidth ratio. The price paid for a wider bandwidth is however the quality of the radiation performance. Below is a list of aspects [2, 3, 4, 5, 6] on the performances of QRFHs which are detrimental to reflector systems – particularly in radio astronomy applications.

- Beamwidth narrowing in the H-plane as frequency increases.
- Rapid beamwidth variation at the mid and highest frequencies.
- High cross-polarisation levels.
- High co-polar sidelobes.
- Variable phase centre.

Almost all of these can in some way be traced back to the interaction of higher-order modes in the QRFH. As the structure is essentially a quad-ridged waveguide of varying cross-section, a large number of waveguide modes in addition to the fundamental TE_{11} mode are typically above cut-off in certain sections of the horn. Over such a wide bandwidth control of these modes are very challenging, as the cut-off frequency and propagation constant of each mode are functions of the varying horn cross-section as well as frequency. Modal aspects become even more important when coaxial probes are employed in the classical feeding of QRFHs, as these typically excite a large number of modes at the coaxial-to-waveguide interface. Due to the difficulty of modelling such a complex modal environment, the standard procedure in designing QRFHs therefore makes use of a combination of analytical functions which describes the tapering profile, as well as optimisation of the entire structure.

The aim of this work is to develop design techniques and a feed mechanism for QRFHs, which specifically focusses on controlling and utilising modal content inside the horn. Such a technique enables a systematic targeting of modal-related radiation effects, and therefore reduces the need for extensive, multi-variable electromagnetic optimisation.

1.2 Contributions

In this dissertation a new feeding technique is firstly proposed for the QRFH, which consists of a quadraxial line terminated in the quad-ridges through the back lid of the horn. This feed presents the possibility of integrating differential LNAs (dLNAs) directly to the terminals of the antenna, in order to reduce unnecessary losses and thus to achieve higher sensitivity. It is shown that all of the radiation issues typically experienced with the QRFH (as listed above) are improved with this feeding technique compared to the conventional coaxial feed. An equivalent circuit model of the proposed quadraxial feed is derived to simplify the design process.

Ridge-loaded cylindrical modes are analysed in this work, as the field distributions of such are not immediately obvious. A large number of the modal cut-off frequencies are also presented that are unavailable in literature.

A prototype antenna is systematically designed, which employs a quadraxial feed, through various modal considerations. The cut-off frequencies throughout the QRFH are utilised for the synthesis of the ridge tapering profile, in order to ensure a desired modal distribution in the circular aperture. The design techniques are confirmed by the measured results of the manufactured prototype. A theoretical aperture efficiency of more than 50% from 2 to 12 GHz is achieved in an unshaped offset Gregorian reflector system – as proposed for the SKA. The phase centre varies only with 30 mm and above 6 GHz with less than 10 mm.

The primary contributions of this dissertation are:

- A quadraxial feeding technique for the QRFH that allows for integration of dLNAs and significantly improves the modal purity [7].
- Design techniques for the QRFH through modal considerations [8].

The secondary contributions of this dissertation are:

- Equivalent circuit for the proposed quadraxial feed [9].
- Analysis of ridge-loaded cylindrical modes with regards to the QRFH.
- Cut-off frequencies of a large number of higher-order ridge-loaded cylindrical modes that are unavailable in literature.

1.3 Overview

In Chapter 2 the main aspects of a receiver, which are important to reflector-based radio astronomy applications, are considered. The main figure of merit is derived, i.e. the receiver sensitivity, followed by a discussion on the noise contributions in the system. The desired radiation properties are considered and the significant reflector efficiencies presented. Requirements for the SKA front-end is given and the reflector optics presented. The chapter ends with a summary of the state-of-the-art in wideband single pixel-feeds.

Chapter 3 begins with the analysis of ridge-loaded cylindrical modes and the implications that it has for the commercial numerical codes used. The quadraxial feed is proposed and developed through the equivalent circuit. The modal content is analysed and evaluated with respect to the conventional feeding technique.

In Chapter 4 the modal effects in the QRFH are discussed. The modal content in the aperture is calculated and used to evaluate the radiation performance. Different QRFHs are designed and used to evaluate the proposed and conventional feeding techniques. A parameter study is also completed in order to obtain a starting point for the final prototype design.

In Chapter 5 the strategy for the design approach and prototype specifications are outlined. The flared section of the antenna is developed through modal considerations, and an improved aperture efficiency is achieved over the 6:1 bandwidth. The modal purity of the basic quadraxial feed is improved and implemented with the synthesised horn. The manufacturing process of the prototype is discussed with the final antenna performances presented.

The dissertation is concluded in Chapter 6 with brief remarks on possible future work.

Chapter 2

Receiver Considerations for Radio Astronomy Applications

In radio astronomical observations the signals that are received from outer space are very weak and therefore require telescopes with high performance. At microwave frequencies, reflector antennas are typically employed to achieve the maximum gain. In addition to the high sensitivity required of such a system, it is also beneficial to facilitate wide bandwidth observations.

In this chapter fundamental concepts in antenna receivers are presented. These range from the figure of merit of the front-end system to the requirements for reflector antennas. The chapter is concluded with practical considerations for the Square Kilometre Array (SKA) project.

2.1 Figure of merit for radio astronomy receivers

The signal-to-noise ratio (SNR) is generally considered as the figure of merit for a communications receiver. In radio astronomy on the other hand, the figure of merit is the receiver sensitivity defined as the ratio of the effective receiving area to the system noise temperature. An illustration of a typical receiver is given in Fig. 2.1 where all the relevant parameters are shown.

The IEEE definition for the effective area (A_{eff}) of an antenna [10] is: "*in a given direction, the ratio of the available power at the terminals* (S_1) *of a receiving antenna to the power flux density* (S_{sig}) *of a plane wave incident on the antenna from that direction and with a specified polarization differing from the receiving polarization of the antenna*". Thus, according to this definition it is clear that the signal power at the antenna terminal is $A_{eff}\ S_{sig}$. The noise power per unit bandwidth is defined in terms of the system noise temperature (T_{sys}) according to the *Rayleigh-Jeans* approximation for high frequencies, i.e. $k_B\ T_{sys}$. This noise power is referred to the input of the LNA (i.e. reference plane $\sum = 1$) .

Using these definitions the SNR at the input of a noiseless LNA can be written as

$$\frac{S_1}{N_1} = \frac{S_{sig}}{k_B}\frac{A_{eff}}{T_{sys}}, \tag{2.1}$$

where k_B is Boltzmann's constant. The term S_{sig}/k_B in (2.1) is independent of the system

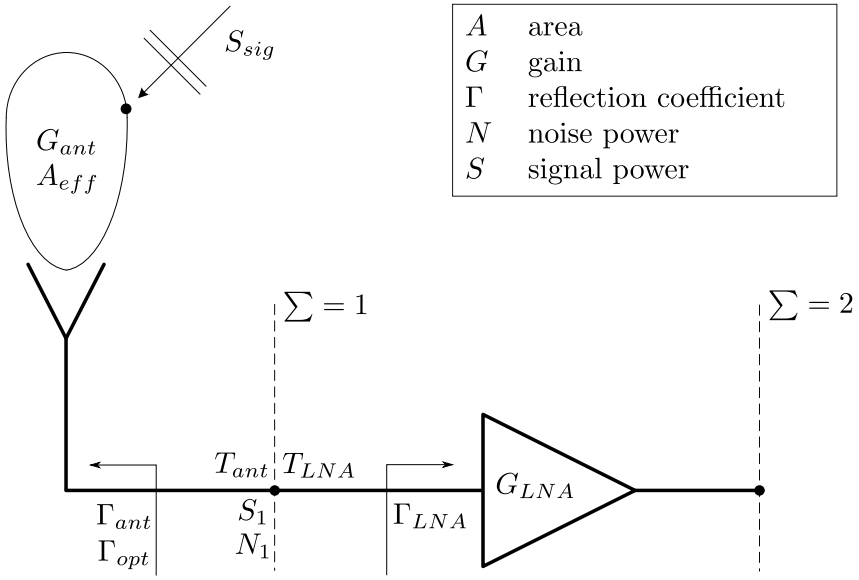

Figure 2.1: Representative model of the receiver – consisting of an antenna and LNA – with all the relevant parameters indicated.

and hence for a qualitative consideration of the system alone, the SNR can be replaced by the system sensitivity A_{eff}/T_{sys}. In the radar community the sensitivity is also referred to as G_{ant}/T_{sys} because the effective aperture area for any antenna is $\frac{\lambda^2}{4\pi}G_{ant}$, where G_{ant} is the gain of the antenna with a conjugately matched termination [10].

The noise temperature of the system is predominantly contributed by the first-stage components which are the antenna (T_{ant}) and the LNA (T_{LNA}) – given that the transducer power gain of the LNA (G_{LNA}) is sufficiently high. Both of these noise temperatures are with reference to the point between the antenna and LNA. Substituting with these parameters the sensitivity therefore becomes

$$\frac{A_{eff}}{T_{sys}} = \frac{\frac{\lambda^2}{4\pi}G_{ant}}{T_{ant} + T_{LNA}}. \tag{2.2}$$

2.2 Noise contributions

2.2.1 LNA noise characteristics

The LNA noise temperature can be described in terms of its widely used noise parameters [11]

$$T_{LNA} = T_{min} + \frac{4T_0R_n}{Z_0}\frac{|\Gamma_{ant} - \Gamma_{opt}|^2}{|1 + \Gamma_{opt}|^2\left(1 - |\Gamma_{ant}|^2\right)}, \tag{2.3}$$

where T_0 and Z_0 are the temperature and impedance references respectively, R_n is the equivalent noise resistance and Γ_{opt} is the optimal source reflection coefficient at which point the minimum noise temperature (T_{min}) of the LNA is achieved.

In [12] Pospieszalski proposed an equivalent noise model along with equations for the noise parameters of an intrinsic FET chip. Within good approximation it follows as

$$Z_{opt} = \frac{f_T}{f}\sqrt{\frac{K_g}{K_d}} + j\frac{1}{\omega C_{gs}}, \tag{2.4}$$

$$T_{min} = 2\frac{f}{f_T}\sqrt{K_g K_d}, \tag{2.5}$$

$$R_n = \frac{1}{T_0}(K_g + \frac{1}{g_m}K_d). \tag{2.6}$$

Note that Z_{opt} is the optimal source impedance related to Γ_{opt}. Equations (2.4) to (2.6) are given in terms of the small-signal parameters (C_{gs}, g_m) and two frequency independent noise constants (K_g, K_d). The latter is defined as $K_g = r_{gs}T_g$ and $K_d = g_{ds}T_d$, where T_g and T_d are the equivalent thermal noise temperatures of the intrinsic gate resistance r_{gs} and drain conductance g_{ds}, respectively. The cut-off frequency of the transistor is simply $f_T = g_m/(2\pi C_{gs})$.

The importance of these equations is that the noise parameters can be calculated at any frequency with only the knowledge of the measured noise parameters at a single frequency and the small-signal parameters, which are normally supplied by the vendor. Furthermore, these equations allow calculations of the typical behaviour of any FET – regardless of the type of technology [13]. From equation (2.4) it is clear that the real part of Z_{opt} reduces with increased frequency, while it can further be shown that Z_{opt} has a locus on the Smith chart that is equivalent to a network with a constant Q-factor of $1/g_m\sqrt{K_g/K_d}$. Most of the ultra low-noise transistors used in the $1-10\ GHz$ range are FETs and therefore these characteristics are of a typical LNA in this range.

2.2.2 Antenna receiver noise

The antenna noise temperature is given as [14]

$$T_{ant} = (1-\eta_{rad})T_0 + T_{sp} + \frac{\eta_{rad}}{4\pi}\oiint_{\Omega} D(\Omega)T_{sky}(\Omega)\ d\Omega, \tag{2.7}$$

where Ω is the solid angle calculated in the direction (θ, ϕ) in the coordinate system of the far-field. The antenna temperature is dependent on the radiation efficiency (η_{rad}) defined for a conjugately matched antenna. The first term in (2.7) is the noise temperature due to the ohmic losses, where T_0 is the physical temperature of the antenna. With reflector antennas the term T_{sp} represents the noise temperature that is due to the spillover radiation of the reflector. It is rather complex to obtain an exact representation for this, since it is dependent on the elevation angle of the spillover as well as the various noise sources and scattering from the ground.

Finally, the last term is the sky noise contribution where T_{sky} represents the sky noise temperature and D the directivity of the antenna which is equal to G_{ant}/η_{rad}. This is also referred to as the brightness temperature and is the noise intercepted by the antenna pattern pointing at the sky. The brightness temperature distribution consists of different sources such as gas emissions in the atmosphere and apparent temperature of the background sky [14].

2.2.3 Active receiver

One of the main requirements in radio astronomy is that the receiver must have high sensitivity. In order to maximise this it follows from equation (2.2) that the system noise have to be minimised. While possibilities for reducing the sky noise contribution is rather limited for earth based observations constituting reflector-based systems, the spillover noise can be controlled through careful design of the antenna feed and dish optics. Losses in the antenna due to cabling and lossy materials can have a large impact on the system noise. For this reason it is beneficial to integrate the LNA directly to the antenna terminals and in the case of differentially fed antennas, by removing the balun and introducing differential LNAs. In addition to this the active receivers are also typically integrated with cryocoolers to reduce thermal losses.

The final noise contribution in equation (2.2) is that of the LNA. This is not only dependent on the transistor characteristics but also on the match between the antenna and LNA [15]. Following equation (2.3) it is clear that the term $|\Gamma_{ant} - \Gamma_{opt}|$ is critical on a systems level. A reference impedance – that is not necessarily a standard 50 Ω value – has to be established according to these two individual subsystems for optimal noise performance.

2.3 Efficiencies in reflector system

2.3.1 Feed pattern

The electric far-field radiation pattern of an antenna can be described in the general form as

$$G_f(\theta, \phi) = G_\theta(\theta, \phi)\bar{u}_\theta + G_\phi(\theta, \phi)\bar{u}_\phi, \tag{2.8}$$

where the fields are defined in a spherical coordinate system. The unit vectors $\bar{u}_\theta$ and $\bar{u}_\phi$, of the field components are defined in the increasing polar angle (θ) and azimuthal angle (ϕ), respectively.

In this dissertation we are only concerned with axially symmetrical reflector antenna systems for radio telescopes, and therefore it is also beneficial to have a reflector feed with rotationally symmetric radiation patterns. Due to the 2π periodicity of the function in ϕ, the far-field pattern of (2.8) can be expanded as a Fourier-series in ϕ as [16]

$$G_f(\theta, \phi) = \sum_{m=1,3,5,..}^{\infty} A_m(\theta)sin(m\phi)\bar{u}_\theta + C_m(\theta)cos(m\phi)\bar{u}_\phi. \tag{2.9}$$

Linear polarisation is assumed here, and throughout this chapter, in the direction of the y-axis for the antenna feed. The summation of the series in (2.9) is only required for the odd values of m due to symmetry. It is shown in [16] that for such a feed only the first-order azimuthal variations, $A_1(\theta)$ and $C_1(\theta)$, contribute to the axially directed radiation field of the antenna (i.e. the main beam), while the other modes reduce the total efficiency. A rotationally symmetric structure, known as a body of revolution (BOR), excited by a short transverse current on the symmetry axis, will always produce the desired radiation pattern referred to as a BOR_1 pattern [17]. The subscript notation here refers to this first-order azimuthal variation, which functions in the same way as the first index of the modes in a circular cross-section waveguide, i.e. TE_{mn}

or TM_{mn} where $m = 1$. Thus a conical horn that is for example excited with the TE_{11} mode, is defined as a BOR_1 antenna.

Ludwig's third definition for cross-polarisation [18] is defined with co- and cross-polar unit vectors of

$$\bar{u}_{co} = sin\phi\bar{u}_\theta + cos\phi\bar{u}_\phi \quad \text{and} \quad \bar{u}_{xp} = cos\phi\bar{u}_\theta - sin\phi\bar{u}_\phi, \tag{2.10}$$

respectively. By applying this coordinate system, referred to as $Ludwig3$, to the BOR_1 pattern of the form in (2.9) with $m = 1$, the far-field becomes

$$G_f(\theta,\phi) = \left[CO(\theta) - XP(\theta)\ cos(2\phi)\right]\bar{u}_{co} + \left[XP(\theta)sin(2\phi)\right]\bar{u}_{xp}, \tag{2.11}$$

where the co- and cross-polar far-field patterns in the $\phi = 45°$ plane (or diagonal, D-plane) are respectively

$$CO(\theta) = \frac{1}{2}\left[A_1(\theta) + C_1(\theta)\right] \quad \text{and} \quad XP(\theta) = \frac{1}{2}\left[A_1(\theta) - C_1(\theta)\right]. \tag{2.12}$$

There are a few things to note from equation (2.11). Firstly, the E- and H-plane co-polar cuts of the pattern are equal to $A_1(\theta)$ and $C_1(\theta)$, respectively. Thus the complete pattern of a BOR_1 antenna can be reconstructed with the knowledge of the fields in these principle planes alone. Secondly, the maximum cross-polarisation field is obtained in the D-plane where $\phi = 45°$. From equation (2.12) it is clear that the cross-polar sidelobes in the D-planes are the difference between the E- and H-plane radiation patterns, and therefore can be caused by both their amplitude and phase differences.

2.3.2 Feed efficiency

The feed efficiency (η_{feed}) is a metric generally used to determine the performance of an antenna as a reflector feed. This consists of multiple sub-efficiencies suggested in [19] as

$$\eta_{feed} = \eta_{BOR1}\ \eta_{sp}\ \eta_{pol}\ \eta_{ill}\ \eta_{ph} \tag{2.13}$$

for a feed in an ideal paraboloidal reflector system, where the subscripts respectively designate a dependence on the higher order azimuthal modes, the spillover, the cross-polarisation, the aperture illumination and the phase errors due to defocusing of the reflector system.

The BOR_1 efficiency (η_{BOR1}) is defined as the ratio of the power in the first-order azimuthal modes to the total radiated power

$$\eta_{BOR1} = \frac{\pi \int_{\theta=0}^{\pi} \left[|A_1(\theta)|^2 + |C_1(\theta)|^2\right] sin\theta d\theta}{\int_{\phi=0}^{2\pi}\int_{\theta=0}^{\pi} \left[|G_\theta(\theta,\phi)|^2 + |G_\phi(\theta,\phi)|^2\right] sin\theta d\theta d\phi}. \tag{2.14}$$

This equation becomes unity for an ideal BOR_1 excitation and therefore the remaining sub-efficiencies are only defined with respect to the first-order azimuthal modes.

In a prime-focus reflector system the feed illuminates the paraboloid with a cone of half-angle

θ_e. This is also referred to as the subtended angle and is calculated as

$$\theta_e = 2\ tan^{-1}\left(\frac{0.25}{F/D}\right), \tag{2.15}$$

where F/D is the ratio of the focal length to the aperture diameter of the reflector. The spillover efficiency (η_{sp}) is therefore defined as the power within the subtended angle relative to the total power, given as

$$\eta_{sp} = \frac{\int_{\theta=0}^{\theta_e} \left[|CO(\theta)|^2 + |XP(\theta)|^2\right] sin\theta d\theta}{\int_{\theta=0}^{\pi} \left[|CO(\theta)|^2 + |XP(\theta)|^2\right] sin\theta d\theta}. \tag{2.16}$$

From the field components of the BOR_1 feed given in (2.11), it is clear that the polarisation efficiency (η_{pol}) – which is the power of the co-polar field relative to the total power within θ_e – is calculated as

$$\eta_{pol} = \frac{\int_{\theta=0}^{\theta_e} \left[|CO(\theta)|^2 + \frac{1}{2}|XP(\theta)|^2\right] sin\theta d\theta}{\int_{\theta=0}^{\theta_e} \left[|CO(\theta)|^2 + |XP(\theta)|^2\right] sin\theta d\theta}. \tag{2.17}$$

Using this definition for the polarisation efficiency[1], the illumination efficiency (η_{ill}) is

$$\eta_{ill} = 2\ cot^2(\theta_e/2)\ \frac{\left[\int_{\theta=0}^{\theta_e} |CO(\theta)|\, tan(\theta/2)\ d\theta\right]^2}{\int_{\theta=0}^{\theta_e} \left[|CO(\theta)|^2 + \frac{1}{2}|XP(\theta)|^2\right] sin\theta d\theta}. \tag{2.18}$$

This efficiency becomes unity when the aperture is uniformly illuminated. The final sub-efficiency in (2.13) is the phase efficiency (η_{ph}) defined as

$$\eta_{ph} = \frac{\left|\int_{\theta=0}^{\theta_e} CO(\theta)\ tan(\theta/2)\ d\theta\right|^2}{\left[\int_{\theta=0}^{\theta_e} |CO(\theta)|\, tan(\theta/2)\ d\theta\right]^2}. \tag{2.19}$$

Note that the numerator here is an absolute value. This efficiency accounts for the phase errors in the co-polar radiation field and is the only sub-efficiency that is dependent on the phase reference point of the feed (i.e. the location of the feed relative to the focal point of the reflector). This property can therefore be used to calculate the phase centre of the feed where η_{ph} is maximised [20]. If the co-polar far-field has constant phase, η_{ph} becomes unity. The phase centre can be viewed as the location where the fields radiate from, and thus for a point source an exact location exists.

[1] In [19] the definition for circular polarisation is used; however, here we are only concerned with linear polarisation.

2.3.3 Sub-reflector diffraction

Additional to the feed efficiency, a prime-focus paraboloid reflector system is also dependent on the blockage caused by the struts/feed, the surface roughness and the diffraction of the reflector. In the case of an offset dual-reflector system – such as the system proposed for SKA and outlined in Section 2.4 – only the diffraction caused by the sub-reflector is of interest for the feed design. There exists no blockage in this system and the surface roughness is dependent on the mechanical properties.

In [21] a technique is proposed to approximate the influence of the sub-reflector diffraction on the aperture efficiency for offset dual-reflector systems. The assumption is made that the feed pattern is axially symmetric and can be approximated by the far-field function

$$G_f(\theta) = \sqrt{n+1}\, cos^n\left(\frac{\theta}{2}\right), \tag{2.20}$$

where n determines the feed taper. By substituting (2.20) into (2.13) the feed efficiency reduces to

$$\eta_{feed} = 4\, cot^2\left(\frac{\theta_e}{2}\right)\left[1 - cos^n\left(\frac{\theta_e}{2}\right)\right]^2 \frac{n+1}{n^2}. \tag{2.21}$$

The sub-reflector diffraction is approximated by the diffraction efficiency (η_d) given as

$$\eta_d = \left|1 + \frac{n\, sin^2(\theta_e/2)\, cos^n(\theta_e/2)}{1 - cos^n(\theta_e/2)} \frac{(j-1)}{\sqrt{2\pi}} \frac{\Delta\rho}{D}\right|^2, \tag{2.22}$$

where D is the projected diameter of the main reflector on the xy-plane and $\Delta\rho$ is the approximate lateral extent of the transition region. This transition region parameter is given as

$$\Delta\rho = \sqrt{\frac{\lambda(\rho_{m0} + \sigma\, \rho_{s0})}{\pi}\left|\frac{\rho_{m0}}{\rho_{s0}}\right|}, \tag{2.23}$$

where λ is the wavelength and ρ_{m0} and ρ_{s0} are the distances along the central ray from the primary focus to the main and sub-reflectors, respectively (see [21, Fig.1] for geometrical parameters). Furthermore, for a Gregorian system $\sigma = 1$ while for a Cassegrain system $\sigma = -1$.

Therefore, it follows that the total aperture efficiency of the offset dual-reflector system is just the product of (2.21) and (2.22)

$$\eta_{ap} = \eta_{feed}\eta_d. \tag{2.24}$$

This closed-form solution for an offset dual-reflector system is beneficial for the design of both optics and antenna feeds. The approximation results of various systems are verified with physical optics simulations in TICRA's GRASP [22]. The proposed technique proves to be accurate for large reflectors, where an average error of 2% is obtained for a sub-reflector as small as 10λ.

2.4 SKA requirements

The SKA is intended to consist of various technologies used for different science cases. One of the main technologies is the reflector antennas that will be used for interferometry. The array configuration increases the collecting area, as opposed to using a large single dish, and thus produces higher sensitivity. Currently the notion is that multiple feeds will be used to cover the large frequency range. Moreover, one of the first phases which are referred to as 'SKA-mid' will have as many as five single-pixel feeds to cover the bands of 350–1050 MHz (Band 1), 950–1760 MHz (Band 2), 1.65–3.05 GHz (Band 3), 2.8–5.18 GHz (Band 4) and 4.6–13.8 GHz (Band 5).

2.4.1 Reflector optics

In the SKA1 baseline design [1] an offset Gregorian (OG) dual reflector system is specified for the dish design. This consists of a paraboloidal main reflector while the sub-reflector is an ellipsoidal shape as illustrated in Fig. 2.2. The SKA Dish Consortium have identified 18 possible OG dish designs as outlined in [23]. Each of the dishes consists of a combination of 3 main geometrical variables – these are a F/D ratio of 0.45, 0.5 or 0.55; a sub-reflector diameter (D_s) of 4, 5 or 6 meters; with and without a sub-reflector extension part between points P_2 and P_3. The latter is to minimise the spillover noise although at the cost of a more expensive sub-reflector. The F/D ratio in this dual reflector system refers to the effective focal length to the aperture diameter of the equivalent paraboloid as derived in [24]. The subtended angles are calculated with equation (2.15) for these specific ratios as 58°, 53° and 49°, respectively. The projected diameter of the main reflector (D_m) in the direction of the primary beam is 15 m, with a maximum paraboloid chord between Q_1 and Q_1 of 18.2 m.

In order to determine the optimal beam magnitude at the subtended angle for this reflector system, i.e. the edge taper on the sub-reflector that will give the best trade-off between the illumination and spillover, the sub-efficiencies are calculated for the BOR_1 pattern given by equation (2.20) where the cross-polarisation is assumed to be zero. This is done by using equations (2.16), (2.18), (2.21) and (2.22) for $\theta_e = 49°$. Note that equation (2.24) is assumed for the aperture efficiency of the OG system (η_{OG}). The results are shown in Fig. 2.3 for various edge tapers defined as

$$|A_0|_{dB} \equiv -20\ log\left(\frac{|G_{co}(\theta_e)|}{|G_{co}(0)|}\right). \tag{2.25}$$

This is related to the parameter n of the far-field function in (2.20) as

$$n = \frac{|A_0|_{dB}}{-20\ log\left(cos(\theta_e/2)\right)}. \tag{2.26}$$

It is clear from Fig. 2.3 that there exists a single edge taper that produces the highest aperture efficiency. This is found for the configuration of the OG system as 10.5 dB and for an ideal paraboloid it is slightly lower at 10 dB, which agrees with the results reported in [21, Fig. 6]. Furthermore, the influence of the diffraction in this case is clearly seen when comparing η_{OG}

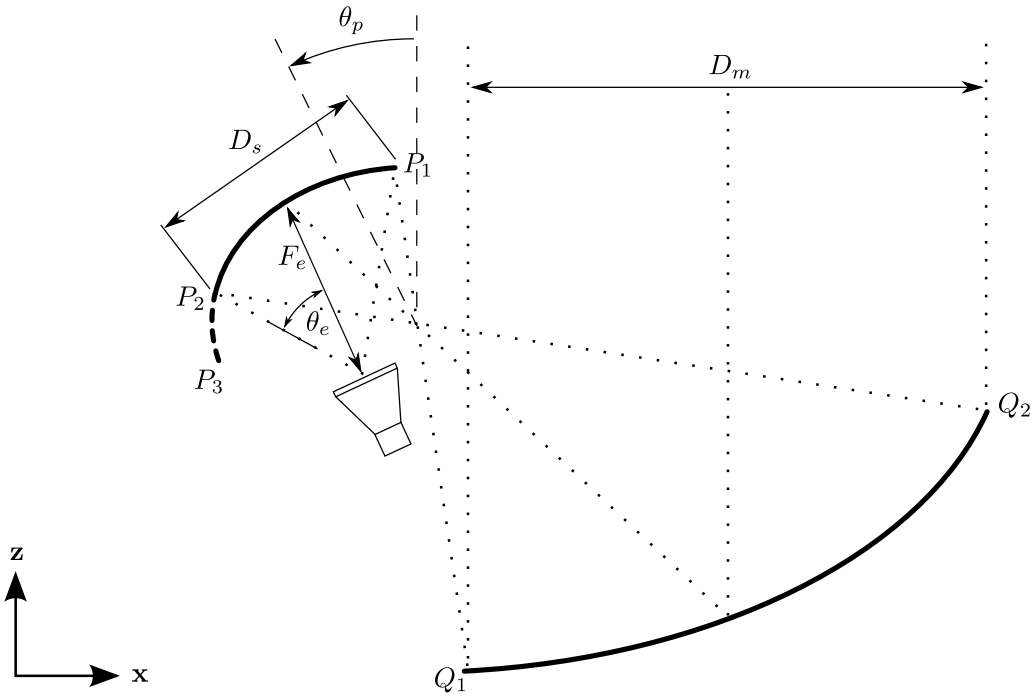

Figure 2.2: The offset Gregorian reflector system with the relevant parameters indicated. The illustration is shown in the xz-plane with the z-axis parallel to the optical axis.

to η_{feed}.

2.4.2 Receiver sensitivity

The effective aperture area of the antenna is given as [25]

$$A_{eff} = \eta_{rad}\, \eta_{ap}\, A, \tag{2.27}$$

where η_{rad} is defined for a conjugately matched antenna according to the IEEE standard definition [10], η_{ap} consists of the sub-efficiencies given in (2.13) along with η_d and A is the physical aperture projected area, which in this case is that of the main reflector.

The original goal of the complete SKA system was to achieve an effective aperture area of 1 km^2 with a system noise temperature of $\sim$ 100 K, which results in a sensitivity of 10,000 m^2/K. According to [26] $Band1$ for the first phase of SKA requires a receiver sensitivity per dish of 4.1 m^2/K. If it is assumed that $\eta_{rad} = 0.9$ and $\eta_{ap} = 0.5$ for the specified 15 m aperture diameter of the main reflector, it follows from equations (2.2) and (2.27) that $T_{sys} = 19.4$ K is required. Alternatively for a higher aperture efficiency such as $\eta_{ap} = 0.7$ the required temperature becomes $T_{sys} = 27.2$ K; however, this is more challenging to achieve over a wider bandwidth with a single antenna feed – see the performances of the possible wideband single-pixel feeds (WBSPF) outlined in Section 2.5.

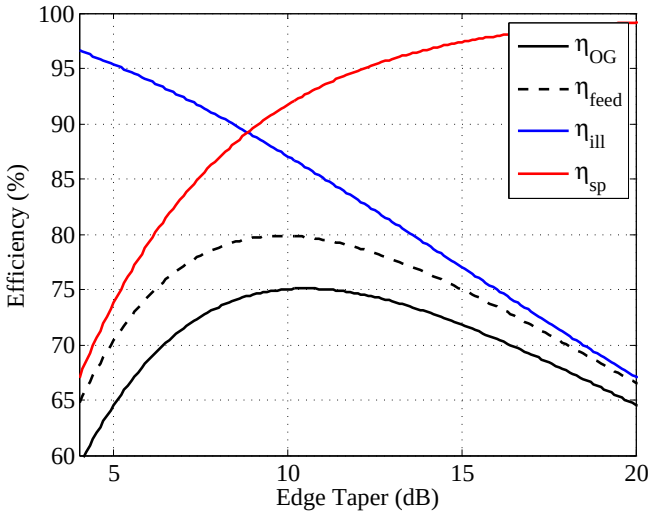

Figure 2.3: Different efficiencies calculated for the BOR_1 pattern given by equation (2.20) for the SKA optics where $\theta_e = 49°$. The plot illustrates how the efficiencies change for different magnitudes of the pattern at the edge of the reflector. Note that the efficiencies for the spillover, the illumination, the feed and the aperture of OG system are respectively depicted by η_{sp}, η_{ill}, η_{feed} and η_{OG}.

2.4.3 Polarisation

Different science cases requires different capabilities from the telescopes. One such requirement for pulsar timing [1] is low cross-polarisation around the centre of the main beam, which is normally specified within the half-power beamwidth (HPBW). On the other hand, for imaging observations astronomers require polarisation discrimination capabilities across a wider processed field-of-view (FoV). The polarisation capability is also very important for the calibration of the telescope.

In terms of an acceptable quantity for the purpose of the front-end design, few conclusive studies are found in literature. In a recent paper by Foster et. el. [27] such an attempt is made for high-precision pulsar timing, which is a key science project for the SKA. In this work it is suggested that the intrinsic cross-polarisation ratio (IXR) values [28] should be higher than 11.5 dB, although for values above 19.5 dB the additional benefit for pulsar timing is negligible. According to [29] the IXR and relative cross-polarisation levels are closely related for the quadruple-ridge flared horn (QRFH), and therefore $|XP| < -15\ dB$ over the HPBW guarantees acceptable performance. Here the relative cross-polarisation is defined as

$$|XP|_{dB} = 20\ log\left(\frac{|G_{xp}|}{|G_{co}|_{max}}\right), \tag{2.28}$$

where G_{xp} and G_{co} are the cross- and co-polarisation E-field components, respectively. Note that these pulsar experiments are in the decimetre wavelength range (i.e. up to $\sim 3\ GHz$) and therefore may only be applicable for the lower frequencies of the WBSPFs.

In [30] the cross-polar level of the L-band feed horn for the Karoo Array Telescope (MeerKAT) – a precursor interferometer for the SKA consisting of 64 dishes – is specified to be below $-25\ dB$ and $-30\ dB$ for the $-1\ dB$ and $-3\ dB$ main beam contours, respectively.

2.5 Wideband reflector feeds

In recent years there has been increased development of high-performance wideband reflector antenna feeds for radio astronomy applications. These feeds typically operate over $10:1$ bandwidths and require stringent characteristics such as stable phase centre and constant input impedance over the entire bandwidth, dual-polarisation and low losses. There are several feeds that attempt to achieve this, such as the non-planar quasi-self-complementary (QSC) antenna from Cornell University [31], the conical-shaped sinuous antenna from the University of Virginia [32] and the Eleven-feed from the Chalmers antenna group in Sweden [33].

Although these antenna-over-ground structures achieve very stable phase centres, it is only the non-planar QSC antenna that achieves an input match of $-9\ dB$ over a decade bandwidth ($0.4 - 4\ GHz$). This non-planar antenna is more difficult to manufacture than the Eleven-feed and conical-shaped sinuous antenna – since both of these only consist of two-dimensional printed elements that requires standard etching procedures. The QSC antenna has not yet been implemented with an active feeding device, although current work is under way towards an integrated cryocooled dLNA.

The conical-shaped sinuous antenna proposed in [32] has successfully been build and tested with balanced amplifiers. The operational band is from 1 to 3 GHz with less than 100 K system noise at room temperature and an antenna input match of $-9\ dB$ for a 260 Ω source impedance. In a prime-focus parabolic system with $\theta_e = 60°$ an aperture efficiency of more that 58% is achieved over this band. It is shown in [32] that the bandwidth of this antenna can be broadened to a decade ($0.3 - 3\ GHz$) by adding more resonator elements. The challenge with this antenna is to realise a feasible feeding network at higher frequencies where the element sizes are very small.

Work done by the Chalmers antenna group shows that it is possible to achieve the reported system sensitivity of $4.2\ m^2/K$ from 2.7 to 8 GHz using the Eleven-feed [34]. An updated design in the form of a circular shaped Eleven-feed was recently proposed [35]. This feed achieves an aperture efficiency of greater than 50 % for a parabolic reflector with subtended angle of 60° over the 1 to 14 GHz bandwidth. The centre puck of the antenna limits the input match at the lower frequencies and therefore from 1.6 to 14 GHz the match is reported as being smaller than $-6\ dB$, with 78% of this range below $-10\ dB$. Similar to the sinuous antenna, the Eleven-feed also requires high-precision with the feeding pins (centre puck) as the operational frequency increases. A drawback of this antenna is that it has 4 ports per polarisation which means that the complete dual-polarised system requires either 4 dLNAs or 8 single-ended LNAs with 4 baluns. Additional to this a 3 dB power combiner is also required per polarisation.

The non-planar log-periodic antenna used in the Allen Telescope Array [36] achieves an input match of $-14\ dB$ over a 20:1 bandwidth. This active feed achieves a measured system temperature of less than 85 K over the operating band from 0.5 to 10 GHz, using dLNA's that are cooled at 60 K. There are, however, two main drawbacks of this design – firstly the antenna is very complex to manufacture and secondly, it has a variable phase centre over the bandwidth which leads to defocussing of the reflector system.

Another class of wideband feeds, consisting of a quad-ridged structure also with variable

phase centre, have successfully been installed on the Goldstone Apple Valley Radio Telescope [37]. These, however, are multiple sub-band feeds with none covering the entire 1 to 10 GHz band.

Another feed of this class is the quad-ridged flared horn (QRFH) that has recently been developed at Caltech as a wideband feed for next-generation radio telescopes [2]. A few variations of this type of horn has been demonstrated as reflector feeds, with the conical type identified as the best candidate [38]. A high performing design of a circular QRFH is reported in [2] with an operational bandwidth from 2 to 12 GHz. This feed has a nominal 10 dB beamwidth of 85° and achieves an aperture efficiency of more than 50% in a shaped dual-reflector system. The phase centre varies with 50 mm over this band and the relative cross-polarisation level peaks at -6 dB with a mean of -10 dB. Both of these results are poorer than that of the Eleven-feed, conical-shaped sinuous and QSC antenna. The input match however is much better than these feeds at -15 dB over most of the bandwidth and -10 dB below 2.5 GHz, while it only requires one single-ended 50 Ω LNA per polarisation.

Furthermore, amongst the WBSPFs discussed here the QRFH is unique in that it can be designed for various beamwidths. In [39] it is reported that a 10 dB beamwidth ranging between 32° and 115° is achievable with this type of feed over a 6:1 bandwidth. This presents an important degree of freedom for reflector systems where different subtended angles are therefore possible. One of the main issues with this antenna is that the aperture efficiency deteriorates rapidly at higher frequencies due to beamwidth narrowing and therefore limits the operational bandwidth to a few octaves.

In conclusion, no WBSPF exists yet that achieves all of the demanding requirements of the SKA. This science project has set the bar in high performance wideband feeds and is therefore currently a great driving force behind these technologies.

Chapter 3

Quadraxial Feeding Network for the QRFH Antenna

A common requirement for all the new types of reflector antenna feeds consisting of pair(s) of interleaved spiral, log-periodical or other travelling-wave structures, which are currently being developed for radio astronomy instruments [2, 33, 32, 31], is that of ultra wideband balanced feed networks. These feed networks are commonly realised by using a balun interfacing the balanced antenna to single-ended amplifiers. However, practical designs of such passive networks are often bulky and lead to power dissipation losses, which reduces the antenna radiation efficiency and increases the system thermal noise temperature [15]. Another limiting factor is that the ultra wideband balun design restricts the reference impedance for the optimum noise matching between the antennas and LNAs. To obviate these disadvantages, differential LNAs (dLNAs), which can be directly integrated at the antenna terminals, have recently emerged as an interesting alternative solution.

In this chapter a new type of differential feed is introduced for the integration of dLNAs with the quadruple-ridged flared horn (QRFH) antenna shown in Fig. 3.1 [7, 9]. This consists of four pins feeding through the back lid of a QRFH, which forms a quadraxial transmission line, and terminates in the four respective ridges. These centre conductors are excited differentially in pairs to establish two orthogonal modes in the ridged waveguide. The bandwidth that is used for this work is from 2 to 12 GHz, though the travelling-wave structure is also scalable with frequency.

3.1 Ridge-loaded cylindrical modes

The field distributions of the modes in empty circular waveguides are extensively reported in [40]. As a reference the E-field distributions of a few cylindrical modes are shown in Fig. 3.2. These are typically excited in the aperture of a QRFH as discussed in the next chapter. Solving Maxwell's equations and the vector wave equation in a cylindrical coordinate system, the cut-off frequencies of the transverse electric and transverse magnetic modes in a circular cross-section waveguide can be derived as

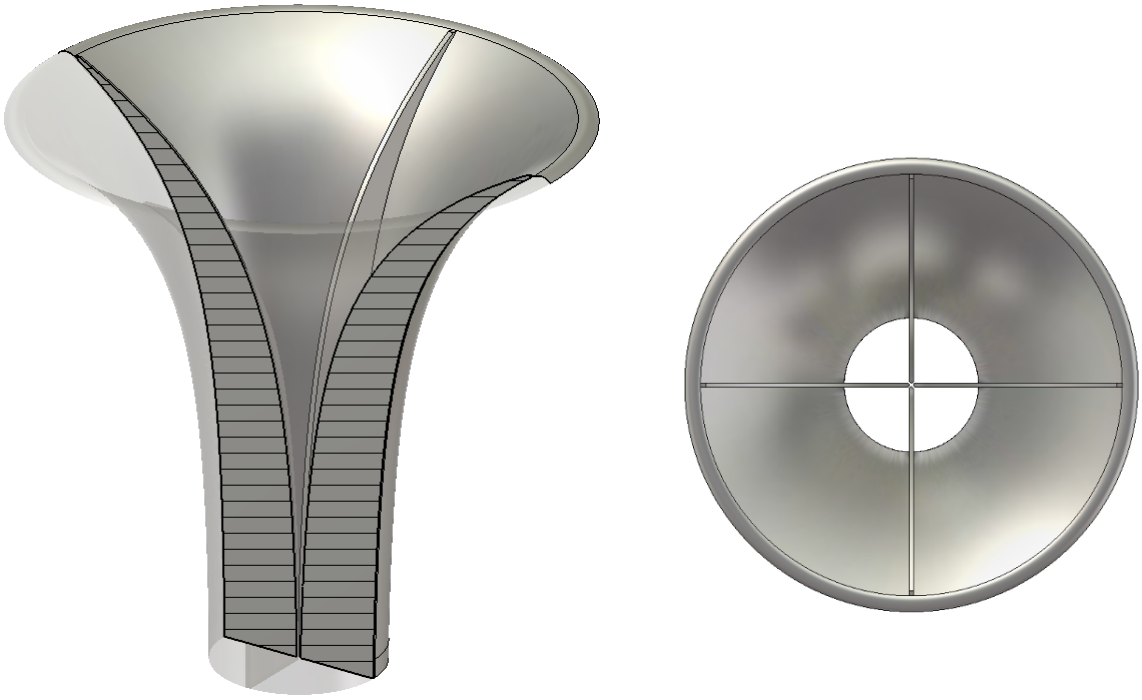

(a) (b)

Figure 3.1: CAD view of the flared section of a typical QRFH antenna. (a) Three dimensional cross-section view. (b) Front view of aperture. Note that the opening at the back is where the throat part connects to.

$$f_c^{TEmn} = \frac{\chi_{mn}^{'}}{2\pi a\sqrt{\mu\epsilon}} \tag{3.1}$$

and

$$f_c^{TMmn} = \frac{\chi_{mn}}{2\pi a\sqrt{\mu\epsilon}}, \tag{3.2}$$

respectively [41]. Here χ_{mn} represents the nth zero of the Bessel function of the first kind of order m, and $\chi_{mn}^{'}$ that of the derivative of the same Bessel function. The radius of the cylinder is a and the permeability and permittivity of the medium are μ and ϵ, respectively. In addition to the cut-off frequency, the field distribution, wave impedance and guided wavelength of each mode are available analytically [41].

With quad-ridged waveguides (QRWGs) however, there exist no analytical solutions for the field equations due to the complexity of such boundary conditions, and therefore numerical codes such as Computer Simulation Technology's Microwave Studio (CST-MWS) are used [42].

While studies of modal behaviour in QRWGs have been reported [43, 44, 45, 46], the cut-off frequencies of only the first few modes are typically given and very little is mentioned of the identification of such modes. This section presents a detailed study of the modes in a QRWG for various ridge heights and difficulties in identifying specific modes are highlighted. These results form the basis of the modal-based design that follow in Chapter 5.

All cylindrical modes are affected to some extent by the loading of the four ridges and as the

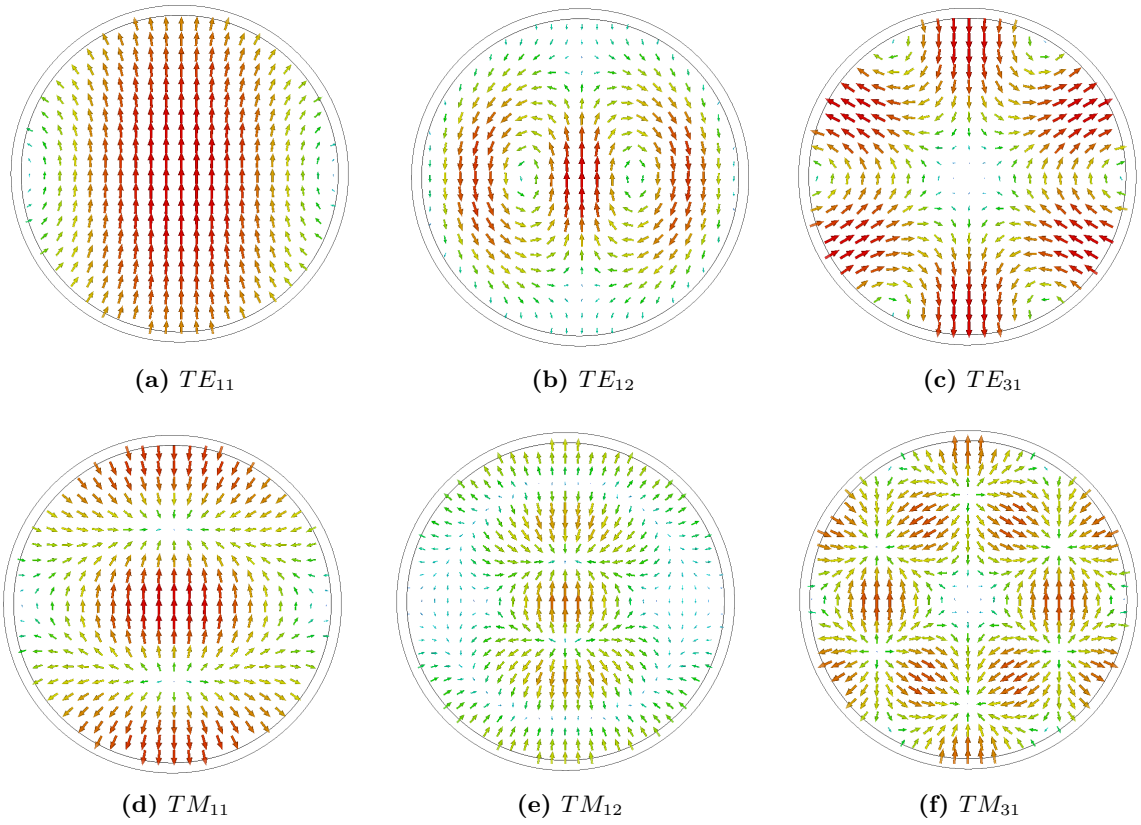

(a) TE_{11} **(b)** TE_{12} **(c)** TE_{31}

(d) TM_{11} **(e)** TM_{12} **(f)** TM_{31}

Figure 3.2: The E-field distributions of the significant cylindrical modes typically excited in the aperture of a low-gain QRFH.

gap becomes very narrow – such as the case is with a typical throat section of a QRFH – the cut-off frequencies of specific modes coincide. Furthermore, due to the inductive and capacitive loading of the ridges, the even-order modes with $m \geq 2$ split into a lower and an upper mode [44], depicted respectively by the notations L and U.

It should be noted that CST-MWS calculates the field distributions in the waveguide port as a superposition of degenerate modes according to its own criteria, and not necessarily based on the normal symmetry planes. In order to obtain the conventional field distributions as reported in [43], E- and H-plane symmetrical walls are therefore used. This is illustrated in Fig 3.3(a)-(c) by the E-field distributions of TM_{01}, TM_{11} and TM_{21L} which are obtained through combinations of the symmetry walls. In Fig. 3.3(d) the distribution is shown for one of the four modes calculated by CST-MWS when no symmetry walls applied. The consequence is that no symmetry is found in the field distributions around any of the ridge-aligned axes.

For clarity, the distributions of the significant degenerate modes are grouped together and referred to as either TM_{ϕ} or TE_{χ}. The TM_{ϕ} modes represent a superposition of TM_{01}, TM_{11} and TM_{21L}, as illustrated in Fig. 3.3; while the TE_{χ} modes represent TE_{22U}, TE_{32} and TE_{42L}. The numerical notations used with these depictions refer to each degenerate mode – e.g. $TM_{\phi}(1)$ in Fig. 3.3(d). Note that the Greek letter subscripts are not indications of any direction. Furthermore, in all of the simulation results presented in Subsection 3.3.4 the E-plane symmetrical wall was implemented, and thus the S-parameters are exclusively solved for both TE_{32} and

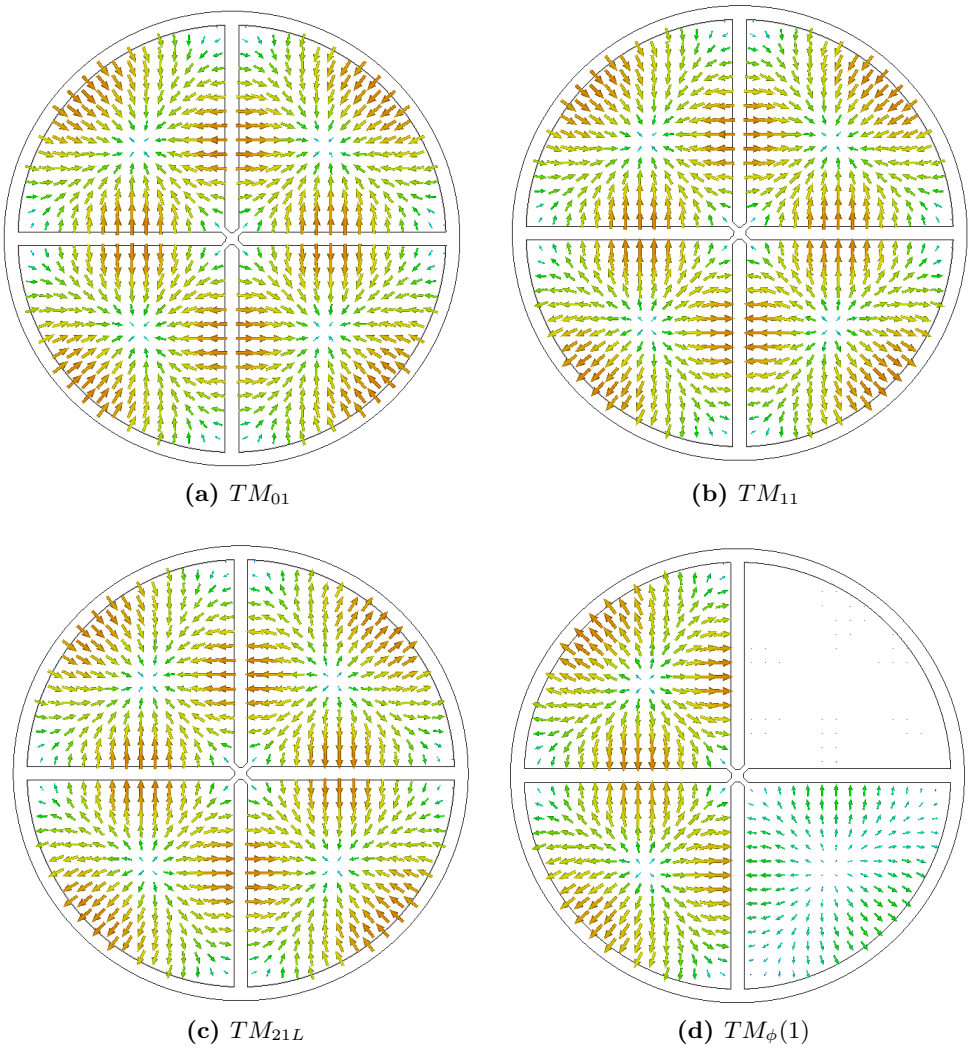

(a) TM_{01} **(b)** TM_{11}

(c) TM_{21L} **(d)** $TM_{\phi}(1)$

Figure 3.3: The E-field distributions of TM_{01}, TM_{11}, TM_{21L} and $TM_{\phi}(1)$, as calculated by CST-MWS.

TM_{11}, which are typically part of the degenerate modal groups.[1]

In CST-MWS it is much faster to use the Time Domain Solver (TDS) for non-resonant wide frequency ranges such as the operational bandwidth of this work. A further time reducing feature with the TDS is the Auto-Regressive filter (AR-filter), which requires only a certain window of the time domain signal. This works well with simple resonant structures; however, due to the complexity of higher-order modes present in the throat, the AR-filter produces numerical artefacts such as active S-parameters. Alternatively, the Frequency Domain Solver (FDS) could also be used, though it is found that for the electrically small coaxial line an oval-shaped field distribution of the TEM mode is calculated in the waveguide port of the coaxial termination. Therefore, the TDS without the AR-filter is used for simulations containing the multi-modal throat sections.

Furthermore, evanescent modes have reactive wave impedances and its field strength decays

[1]Note that only one pair of pins can be excited with an active symmetry wall and consequently the orthogonal pair is not terminated by the port. This approach is verified in simulation and no drastic differences between either the S-parameters or port impedances, with and without the walls, are found.

over distance. In the throat section of a QRFH, the evanescent modes are of no concern as it carries no real power. Therefore, a throat length of 40 mm is used – which is long enough for the sufficient decay of the significant modes – in all of the S-parameter simulations of the throat sections in this chapter. It is worth noting that the poles and zeros found in the transfer coefficients of the throat, as given in Section 3.3.4, are due to the fact that at the cut-off frequency the wave impedance of a TM or TE mode becomes 0 or ∞, respectively.

In order to analyse the modal propagation throughout a QRFH, it is imperative to determine the cut-off frequencies of modes in a circular waveguide for different ridge heights. This is done by using CST-MWS to calculate the modes for different sizes of the gap between opposing ridges as shown in Fig. 3.4. The QRWG, as illustrated by the inset in Fig. 3.4(b), has a fixed radius (a) of 33.55 mm with ridge thickness $t = 3$ mm. The ridge chamfer is fixed with a tip width $w = 1$ mm at the gap width $g = 2.5$ mm – i.e. the 45° chamfer is only present for small values of g.

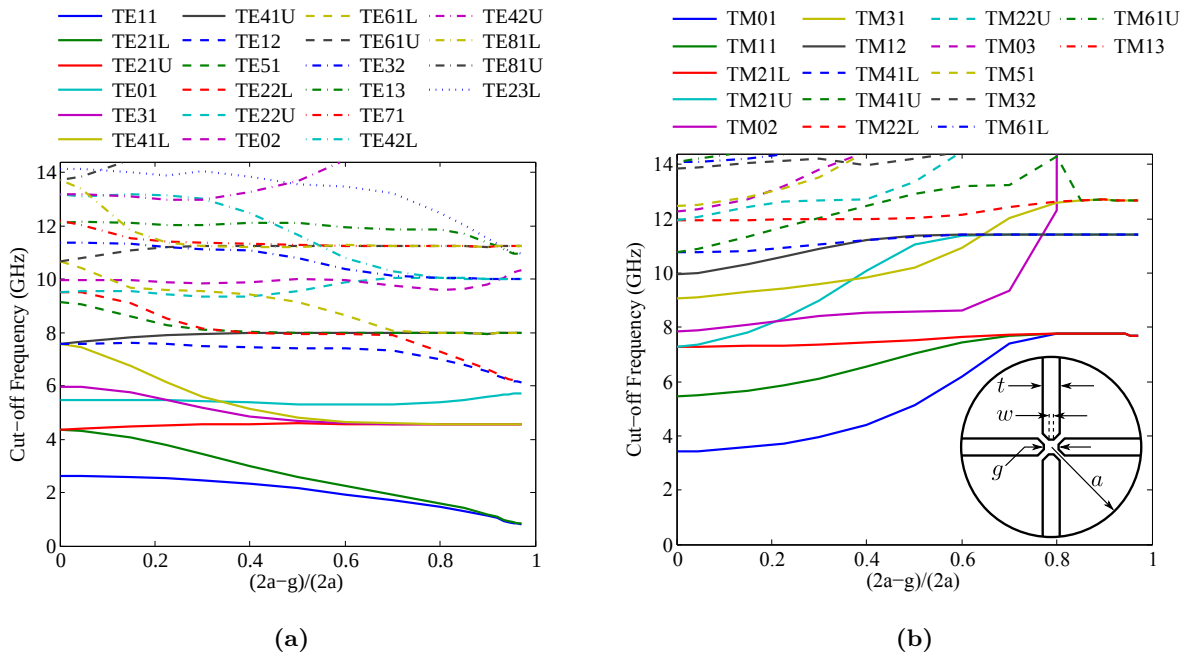

Figure 3.4: Cut-off frequencies of the cylindrical modes as the ridge loading increases. The QRWG has a fixed radius of 33.55 mm and ridge thickness of 3 mm. The ridge chamfer is fixed with a tip width $w = 1$ mm at the gap width $g = 2.5$ mm.

In Fig. 3.4(a) it is clearly seen how the cut-off frequency of the fundamental TE_{11} mode decreases with a smaller gap width. Conversely, most of the TM modes have rapid increases in their cut-off frequencies as a result of the heavy ridge-loading. The cut-off frequency of the TE_{21L} mode is almost identical to that of TE_{11} for a narrow gap; however, when this mode is sufficiently suppressed, the single-mode operation of TE_{11} has a bandwidth of 5.6:1. From the analysis of the feeding techniques presented in Section 3.4, it is normally found that the strongest excited mode after TE_{11} is TE_{12}. Therefore, the single-mode operational bandwidth can have a ratio as wide as 8.9:1 – for the QRWG dimensions of $Throat2$ as defined in Section 3.3. Note also that the wave impedance of TE_{11} approaches infinity as $f \to f_c$, and therefore

the lowest frequency that this QRWG is designed to operate at is $f_{lo} = 2.44 f_c$.

As the ridges load the different modes it is easy to mistake the field distribution of one mode for another. For example, in Fig. 3.4(b) it is seen that the cut-off frequencies of TM_{02}, TM_{31}, TM_{22L} are almost the same at $(2a - g)/(2a) = 0.8$. As this ratio is increased above 0.8, f_c^{TM02} increases suddenly while f_c^{TM41U} is lowered and converges with that of TM_{31} and TM_{22L}. Here it is easy to mistake TM_{41U} for TM_{02} as their f_c curves seem to fit better when their values are interchanged above the 0.8 ratio. The H-field distributions of these four modes are shown in Fig. 3.5 and seem very similar. The key therefore in identifying each mode correctly, is to follow the field distributions as the gap width is narrowed. This can best be achieved when highlighting some characteristics in the field distributions as illustrated in Fig. 3.6.

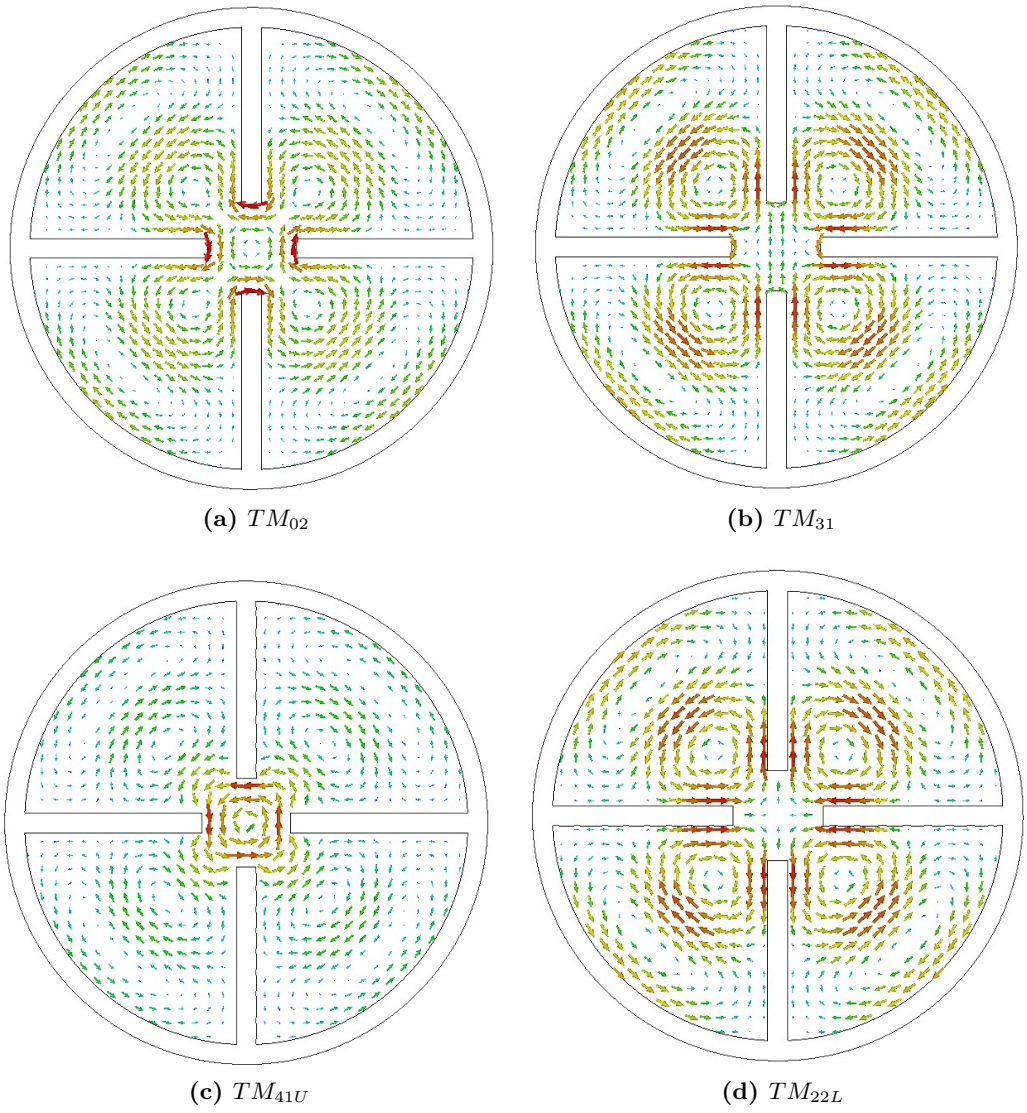

(a) TM_{02} **(b)** TM_{31}

(c) TM_{41U} **(d)** TM_{22L}

Figure 3.5: The H-field distributions of TM_{02}, TM_{31}, TM_{41U} and TM_{22L}.

A few other modes that are typically also mistaken are shown in Fig. 3.7. The TE_{22L} and TE_{42L} modes have similar E-fields as seen from Figs. 3.7(a) and (b); while the TM_{32} and TM_{51} modes have H-fields with similarities as seen from Figs. 3.7(c) and (d).

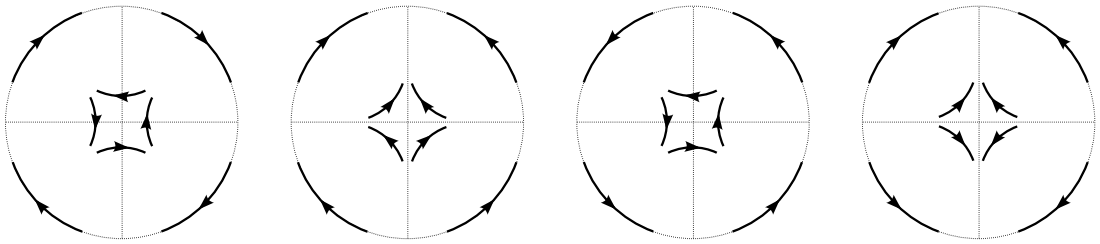

(a) TM_{02} **(b)** TM_{31} **(c)** TM_{41U} **(d)** TM_{22L}

Figure 3.6: Highlighted characteristics of the H-field distributions in Fig. 3.5 of TM_{02}, TM_{31}, TM_{41U} and TM_{22L}.

3.2 Feeding of QRFH antennas

3.2.1 Conventional feeding techniques

Many reflector antenna applications, including that of radio astronomy, require dual-polarisation over wide bandwidths. Different forms of the classical horn antenna (e.g. with corrugations, smooth-walls, tapered sections, etc.) are typically employed as reflector feeds due to their low losses and rotationally symmetric radiation patterns. In order to excite orthogonal modes in the throat of a horn – required for the dual-polarised operation – an ortho-mode transducer (OMTs) is used. A number of OMT topologies have been reported for this purpose; however, the QRWG type is typically favoured for its wideband performance [47].

The classical feed network of a QRWG, first reported in [48], consists of one coaxial port per polarisation, where a coaxial line feeds through one ridge with its centre conductor terminated in the opposing ridge, as illustrated in Fig. 3.8. This forms an unbalanced to balanced transition with a cavity at the back of the waveguide to establish a resonant structure which ensures propagation towards bore-side, referred to as the "back-short" as indicated in the illustration. Note that the two pins for the orthogonal polarisations are offset in the longitudinal direction, and therefore the back-short can not be an optimal solution for both excitations simultaneously [47].

The standard horn antenna is limited to a bandwidth ratio of about 2:1 due to the propagation of higher-order modes which degrade the radiation performance. In a QRWG the ridges load each mode and causes the cut-off frequency of the fundamental mode to decrease – thus establishing a wider single mode bandwidth. In [43] it is reported that by properly exciting the waveguide it is possible to achieve an operational bandwidth as large as 6:1. This characteristic is exploited in QRFH antennas.

The QRFH is in its simplest form a QRWG that matches free space to a ridged waveguide through the flaring of the sidewall and ridges, as illustrated in Fig. 3.1. Although it is possible to achieve an input match lower than $-10\ dB$ over an entire 6:1 bandwidth with the widely used coaxial feeding in Fig. 3.8, the radiation patterns are not rotationally symmetric, high sidelobe levels are obtained and the beamwidths vary over the frequency range [5, 49, 50].

Furthermore, the practical realisation of the long coaxial line inside the thin ridge is mechanically challenging, and high accuracy is required for good electrical performance. Possible

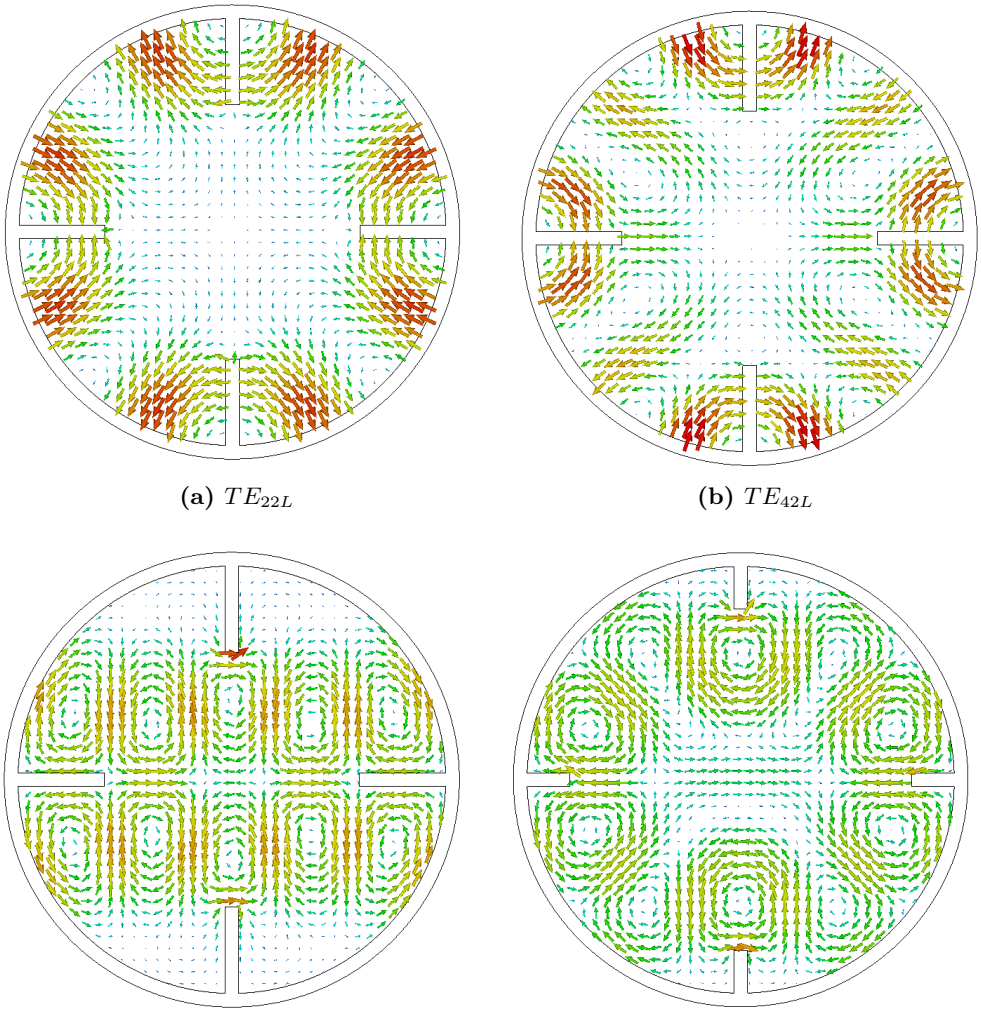

(a) TE_{22L} **(b)** TE_{42L}

(c) TM_{32} **(d)** TM_{51}

Figure 3.7: The E-field distributions of (a) TE_{22L} and (b) TE_{42L}; and the H-field distributions of (c) TM_{32} and (d) TM_{51}.

asymmetry in the coaxial feeding can easily excite the first unwanted even-mode, which typically has a very low cut-off frequency close to that of the fundamental mode due to the narrow gap between the ridges [44]. As the ridges are tapered out towards bore-side, the cut-off frequency increases rapidly and the even-mode becomes evanescent at some point.[2] This causes the mode to be trapped in the section between the back-short and cut-off point, which can cause unwanted resonances that degrades the performance [47].

3.2.2 Proposed feeding network

A new feeding network [7] for a QRFH antenna is proposed in this dissertation as shown in Fig. 3.9. It consists of a quadraxial line with each separate centre conductor connected to a corresponding ridge. The quadraxial line feeds through a cylindrical aperture in the back lid of the QRFH as illustrated in the inset of Fig. 3.9. The centre conductors are differentially excited

[2]This is reported in [47] for the QRWG OMTs; however, the same applies for the QRFH if the sidewall is not flared enough for such a mode to propagate above cut-off.

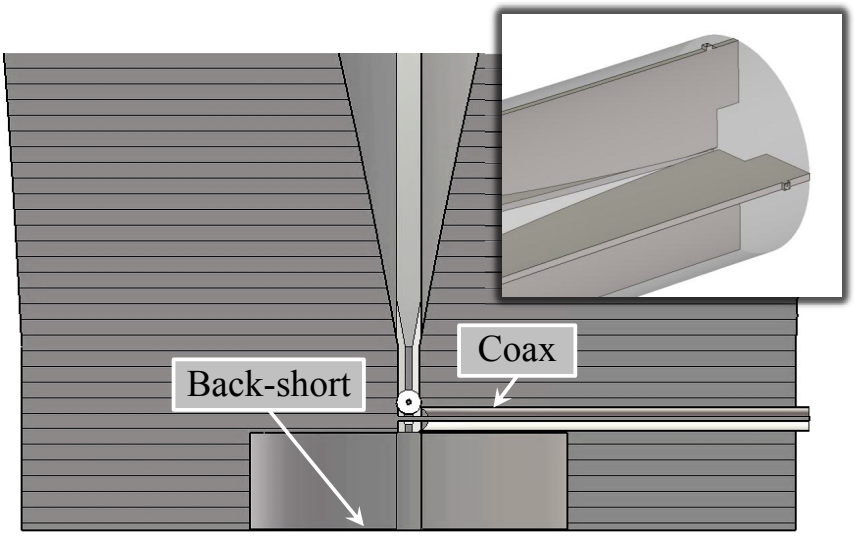

Figure 3.8: CAD view of the cross-section of a typical QRWG excited with a conventional coaxial feed. Each of the two excitations consists of a ridge-to-coax transition with a back-short section. The inset shows the four ridges inside the circular waveguide.

in pairs, which effectively forms two twinaxial transmission lines. This feeding technique allows the excitation of two orthogonal TE_{11} fundamental modes in the ridged waveguide which are required for the dual-polarisation operation of the QRFH.

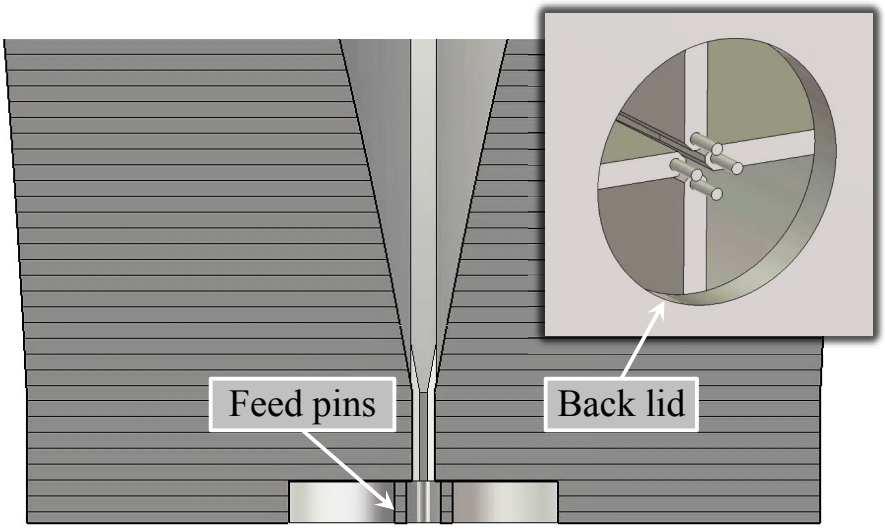

Figure 3.9: CAD view of the cross-section of a typical QRWG that is excited with the proposed feed. The inset shows the quadraxial pins that feed through the back lid and terminate in the ridges.

There are a few qualitative rules that need to be considered when designing the quadraxial feed:

(i) Each pin should be placed as close as possible to the inner edge of the corresponding ridge to minimise the excitation of higher-order modes.

(ii) The radius of the pin is limited by the ridge thickness – practically each pin has to be

inserted into a ridge and therefore cannot exceed this size.

(iii) The radius of the outer conductor of the quadraxial line must be small enough in order to avoid resonances of the TE_{11} mode in the quadraxial line and to minimise the excitation of higher-order modes in the throat section.

This new feeding technique presents the possibility of integrating dLNAs directly with the antenna and essentially eliminates the long lossy coaxial cable formerly required to connect the LNAs [2]. It is a compact solution and therefore is attractive for implementation using cryocoolers. Furthermore, with a purely differential excitation the radiation pattern is symmetrical in both the E- and H-planes.

3.3 Development of quadraxial feed

The QRFH has the useful feature of allowing the separation of the feeding/excitation part from the radiator part, when modelled electromagnetically. The former consists of the section in which the QRWG is uniform, as illustrated in Fig. 3.10(b), and is referred to as the throat of the horn antenna. The latter is the flaring waveguide part which typically looks like the horn illustrated in Fig. 3.1 and consequently is referred to as the flared section.

The throat section has little influence on the radiation properties and mainly determines the input impedance of the feeding network. Note that the back-short of a coaxial feed does however affect the radiation to some extent. The flared section is responsible for the modal excitation which ensures the radiation properties, and is typically a well matched guide between free-space and the throat section. This separation feature, similar to the approach used with tapered slot antennas [51], is exploited for the development of a quadraxial-fed throat. In Chapter 4 this throat is integrated with a radiator to form a functional QRFH antenna.

3.3.1 Configuration for the design and analysis

In order to aid the design process, this section presents an equivalent circuit model of the proposed feed [9]. In Fig. 3.10(a) the back view of the throat is shown where the pins terminate in the ridges. The important dimensions here include the ridge thickness t, the gap between opposing ridges g, the ridge tip width w due to the chamfering that allows a narrow ridge gap, the radius of the pin a_{pin}, the offset distance of the pin from the symmetry axis a_{sep} and the radius of the cylinder in the back wall a_{cyl} where the pins feed through. In Fig. 3.10(b) a cross-section cut in the yz-plane of the throat is shown. As seen the ridged waveguide is uniform with cylinder radius a_{th} and length L_{th}. The length of the cylinder of the quadraxial line is depicted by L_{cyl}.

For the purposes of this work, the QRFH needs only be excited differentially with two sets of excitations – one exciting the vertically orientated ridges and the other the horizontally orientated ridges. As the two resulting fields are simply rotated versions of each other, two separate and identical circuit models can be constructed. To set up a field solution corresponding to one of these excitations in CST-MWS, the structure in Fig. 3.10(b) is terminated at plane

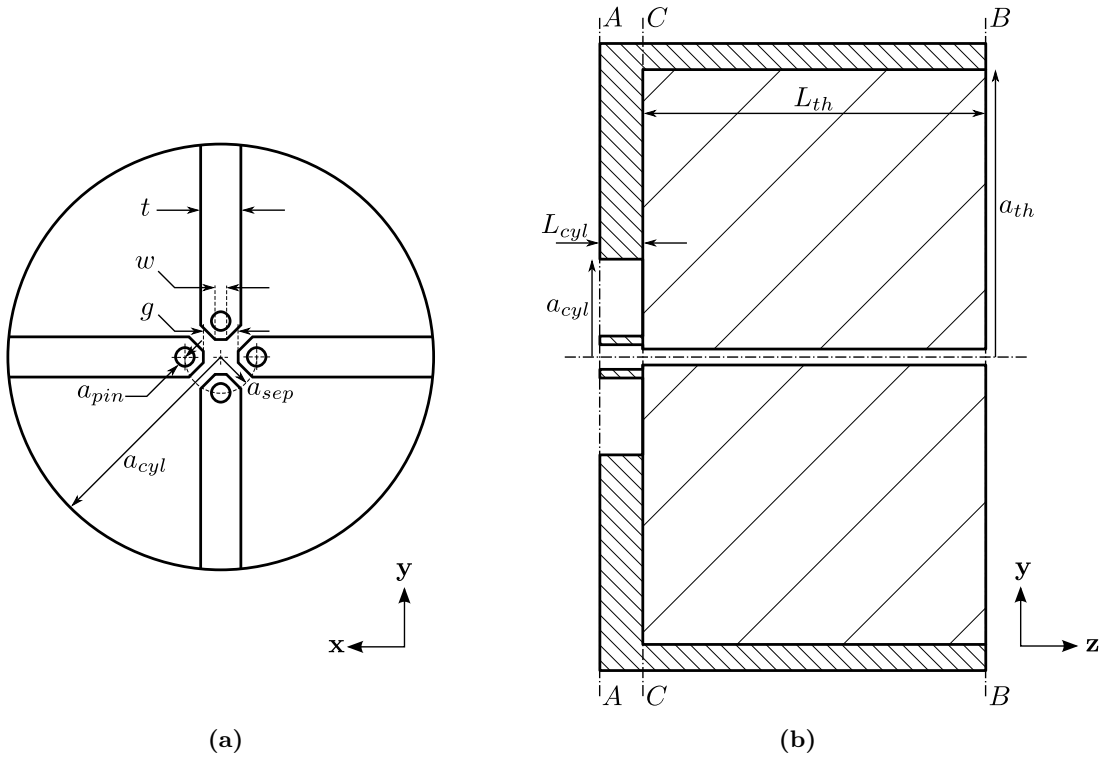

Figure 3.10: (a) View in the xy-plane of the quadraxial feed terminating in the ridges. (b) Cross-section view in the yz-plane of the throat with the quadraxial feed. Note that the illustration in (a) is the scaled-up view seen from looking into plane A-A from the left-side in (b).

B-B with a waveguide port allowing for all the propagating modes, and at plane A-A with a multi-pin feed exciting only two opposing pins differentially.

In order to evaluate the proposed circuit model, two different QRWGs are employed. The dimensions of these uniform waveguides are based on the throat sections of two existing QRFH antennas which were both designed for dual-reflector systems with similar subtended angles. The first throat, referred to as $Throat1$, is reported in [52] for a preliminary QRFH design for Band 1 of SKA-mid, which covers a 3:1 bandwidth from 0.35 to 1.05 GHz. The second throat ($Throat2$) consists of the dimensions reported in [2] for a QRFH with a 6:1 bandwidth from 2 to 12 GHz. The parameter values of these ridged waveguides are given in Table 3.1. Note that the dimensions reported for $Throat1$ are scaled from its lowest frequency $f_{lo} = 0.35\ GHz$ to the band of interest where $f_{lo} = 2\ GHz$.

Table 3.1: The coaxial-fed impedances and ridged waveguide dimensions (as depicted in Fig. 3.10) of $Throat1$ and $Throat2$.

Parameter	$Throat1$	$Throat2$
Z_0	100 Ω	50 Ω
a_{th}	33.55 mm	28.05 mm
g	1.87 mm	1.3 mm
t	2.15 mm	3 mm
w	0.61 mm	0.51 mm

These two particular throat sections are chosen for a few reasons. Firstly, both have a similar cut-off frequency of the fundamental TE_{11} mode, while secondly the diameter of $Throat1$ is larger than $Throat2$ and allows the propagation of a larger number of higher-order modes. Finally, both are designed to be excited by coaxial feeds and achieve good input matches, with a characteristic impedance of 100 Ω for $Throat1$ and 50 Ω for $Throat2$. The utilisation of these different characteristics will become clearer as the chapter progresses.

3.3.2 Equivalent circuit model

The equivalent circuit model – derived for one differential excitation of the quadraxial feed – is shown in Fig. 3.11. As discussed, the exact same circuit also holds for the second differential excitation of the quadraxial feed, which is simply the first excitation rotated by 90°. The circuit consists of an impedance transformer with winding ratio K:1 which transforms the impedance of the differential TEM mode (Z_0) in the quadraxial line to the impedance of the TE_{11} mode (Z_w) in the QRWG, and shunt elements L_p and C_p which models the reactive fields generated at the discontinuity formed by the transition from the quadraxial line to the QRWG. Note that this model is only valid if the implementation of the quadraxial feed adheres to design rules (i) to (iii), as listed in Section 3.2.2.

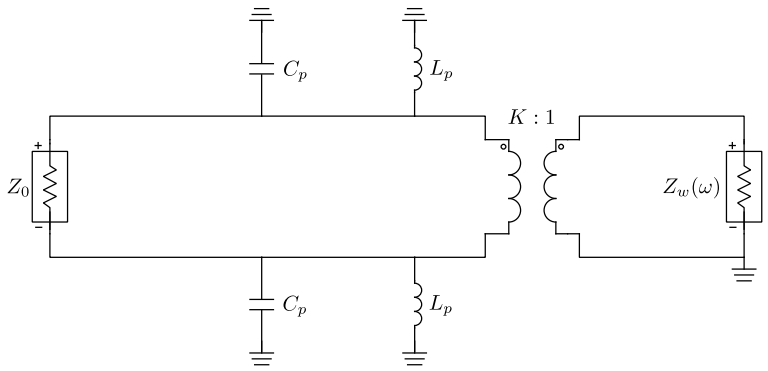

Figure 3.11: Equivalent circuit model for the transition from the differential TEM mode in the quadraxial line to the TE_{11} mode in the QRWG. The circuit represents the transition only, found at plane C-C in Fig. 3.10(b).

The transformer ratio is simply calculated as

$$K = \sqrt{\frac{R_{eq}}{\eta_0}}, \tag{3.3}$$

where

$$R_{eq} = \frac{1}{\mathfrak{Re}\{Y_e\}} \tag{3.4}$$

and Y_e is the input admittance as seen from port 1, referred to plane C-C, and averaged over the frequency range of single-mode TE_{11} propagation. This admittance typically has a frequency dependent susceptance while the conductance is near constant over frequency and mostly influenced by the dimensions of the ridged waveguide. The parameter η_0 represents the intrinsic wave impedance of free-space which is 377 Ω. The latter is chosen due to the fact that as the

frequency increases above cut-off the wave impedance of a mode tends to 377 Ω. This is found to be more effective than using the actual wave impedance of TE_{11}, which would result in a frequency dependent transformer.

Table 3.2: The quadraxial feed dimensions as depicted in Fig. 3.10.

Parameter	Value
a_{pin}	0.5 mm
a_{cyl}	11.4 mm
L_{cyl}	3.5 mm
a_{sep}	equation (3.5)

To illustrate the dependencies of the different circuit components on the physical dimensions, the quadraxial feed is implemented in $Throat1$ and $Throat2$. The dimensions are chosen according to Table 3.2 and the length of the line is de-embedded in order to consider the transition alone. The pin offset is calculated as

$$a_{sep} = (g/2 + t/4 + a_{pin}) \tag{3.5}$$

to ensure that design rule (i) in Section 3.2.2 is satisfied.

The values of the equivalent resistance R_{eq} are plotted in Fig. 3.12(a) for different values of the ridge dimensions g and t. Here it is clearly seen that as the gap narrows between the ridges the equivalent resistance becomes smaller, while a thinner ridge ensures overall larger values. Note that the only geometrical differences here between $Throat1$ and $Throat2$ are the cylindrical diameters a_{th} (i.e. respectively 33.55 and 28.05 mm) and the tip widths of the ridges w (i.e. respectively 0.61 and 0.51 mm). Thus, $Throat1$ has a smaller equivalent resistance than $Throat2$ due to its larger distributed capacitance caused by the larger tip width of the ridges, observed in Fig. 3.12(a). As expected, the equivalent resistances of these two throat sections are almost equal to the respective characteristic impedances of their designed coaxial feeds given in Table 3.1 – i.e. $Z_0 \approx R_{eq}$. Furthermore, it is found that only the dimensions of the ridged waveguide have a significant influence on R_{eq}.

The inductance L_p in the circuit model is almost linearly dependent on the diameter of the outer conductor of the quadraxial line a_{cyl}, whereas C_p is essentially constant, as shown in Figures 3.12(b) and (c). Therefore, the physical interpretation of L_p is that the section of the back of the ridge where the quadraxial line terminates – i.e. between a single pin and the outer conductor [see Fig. 3.10(a)] – forms a distributed inductance which is dependant on the length $(a_{cyl} - a_{sep})$. The ridge thickness also has some influence on this inductance. The slight differences between the values obtained for the two throats can be ascribed to the fact that the ridge gap is larger in $Throat1$, and therefore effectively reduces the inductance L_p compared to $Throat2$.

This simple inductance model is valid for short transition regions only. For longer regions, Fig 3.12(d) shows the dependence of L_p on the physical length L_{cyl}, for the instance where $a_{cyl} = 11.4\ mm$. The different values for t have similar influences on L_p as in Fig. 3.12(c). Therefore, it is reasonable to conclude that the inductance component is dependent on the physical path of the current from the point where the pins terminate in the ridges to the grounded

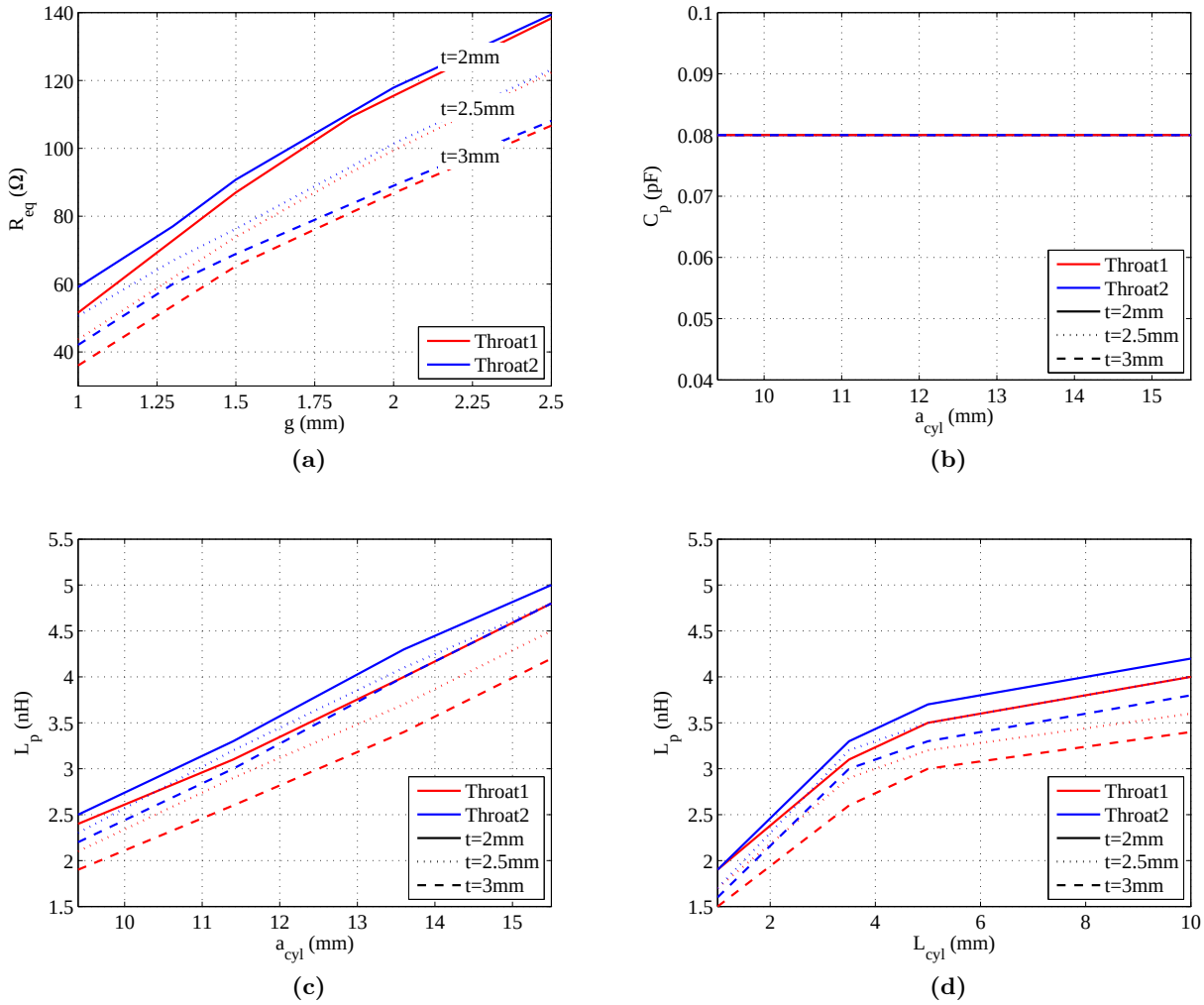

Figure 3.12: The values of the circuit components (a) R_{eq}, (b) C_p and (c)-(d) L_p for different simulation dimensions.

part of the multi-pin port, as illustrated by the current distribution in Fig. 3.13.

Finally, a_{pin} and a_{sep} do not have any significant influence on the equivalent circuit as long as the design rules in Section 3.2.2 are applied. The throat length L_{th} can be of arbitrary length due to the ideal modal termination of the waveguide port. In the simulation setup this should however be long enough so that the reactive power of the evanescent modes does not influence the S-parameter results.

To illustrate the accuracy of the equivalent circuit model, Γ_{in} of a few different quadraxial-fed throat sections is plotted in Fig. 3.14. The dimensions in Tables 3.1 and 3.2 are used with variations of a_{cyl} and t. Good agreement is found between the CST-MWS simulation and the circuit model; however, at the highest frequencies there exist some deviations and more significantly so for the instance where $a_{cyl} = 15.5\ mm$. This is due to the excitation of higher-order modes as discussed in Subsection 3.3.4.

To model the effects of higher-order modes, the simple single-mode circuit model evidently becomes insufficient, and models incorporating higher-order modes become necessary. One such

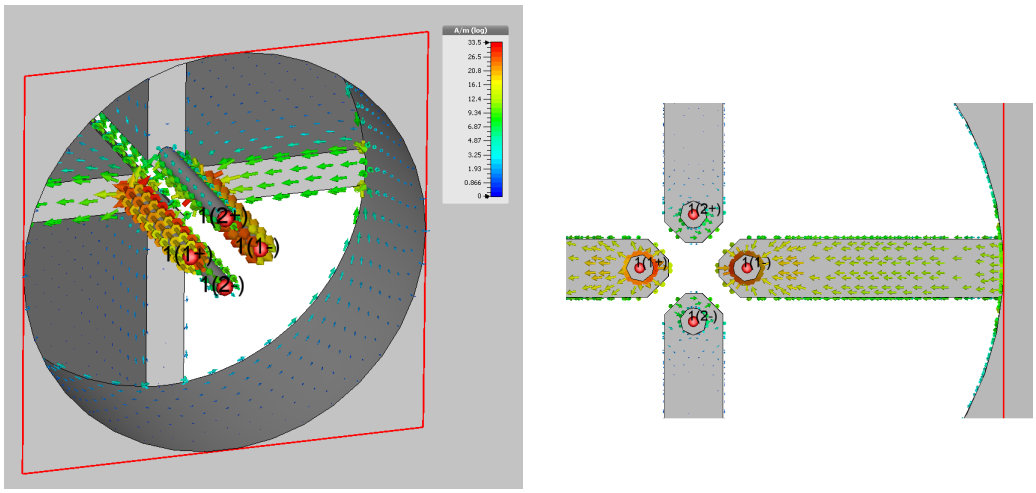

(a) **(b)**

Figure 3.13: Current distribution in the quadraxial feed at 2 GHz. (a) The 3D view of the quadraxial line. (b) The enlarged view of the back of the ridges, where the highest current distribution is seen on the ridges excited by the differential pin-pair depicted by port 1(1).

model represents each mode as a separate waveguide port, with possibly complex transformer ratios [53]. For the purposes of this work – where single-mode excitation of the throat sections is desired over wide bandwidths – the proposed circuit model is however more useful for optimisation with less complexity.

3.3.3 Quadraxial transmission line

In the previous subsection many of the key dimensions are discussed with regard to the input match; however, some implicit assumptions are made concerning the dimensions of the quadraxial feed. One of these dimensions is the length of the quadraxial line L_{cyl}. Up to this point the line length has been de-embedded from all the results in order to investigate the transition rather than the line itself. For a good match, however, it should be clear that Z_0 of the line should in theory equal R_{eq}, or be as close as possible in value. However, physical restrictions exist which makes this very difficult.

The quadraxial transmission line with the differential excitation of the pin pairs can effectively be reduced to a twinaxial line. The differential impedance of a shielded twinaxial line can be described analytically as [54]

$$Z_0 = \frac{276}{\sqrt{\epsilon_r}}\, log\left[2\frac{a_{sep}}{a_{pin}}\frac{\left(a_{cyl}^2 - a_{sep}^2\right)}{\left(a_{cyl}^2 + a_{sep}^2\right)}\right] \qquad \text{for} \quad a_{cyl} \gg a_{pin},\ a_{sep} \gg a_{pin}. \tag{3.6}$$

The dimension parameters of the quadraxial line as depicted in Fig. 3.10 are used for the twinaxial configuration here. The parameter ϵ_r is the relative permittivity of the material inside the line – for the quadraxial feed it is just equal to 1. Thus it is clear that for an increased permittivity the impedance is lowered. Note that equation (3.6) is valid for two conditions of which the first is generally satisfied with the quadraxial feed. Due to design rule (i) in Section

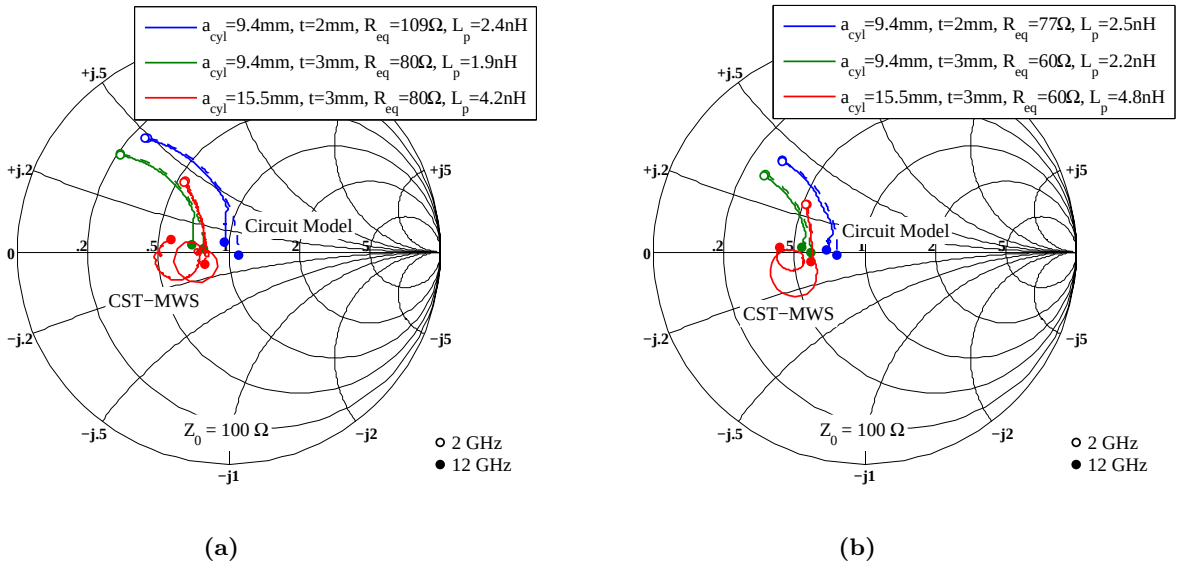

(a) **(b)**

Figure 3.14: The input impedances of (a) *Throat*1 and (b) *Throat*2 for different dimension sets. The CST-MWS simulation is depicted by the solid line and the corresponding circuit model by the dashed line.

3.2.2 the value for a_{sep} is bounded by the ridge gap and therefore it is difficult to obtain a large enough value to satisfy the second condition. The deviation caused by the latter is seen in Fig. 3.15(a), where the full-wave simulated impedances are indicated by the markers and compared with that of the impedances calculated with (3.6), depicted by the solid lines. Here the deviation is largest where $a_{sep} \to a_{pin}$, although still relatively small. Furthermore, it is clear that the differential impedances in Fig. 3.15(a) are generally large compared to the values for R_{eq} given in Fig. 3.12(a). These large values are restricted by the specific throat dimensions that dictates the values for a_{pin} and a_{sep}.

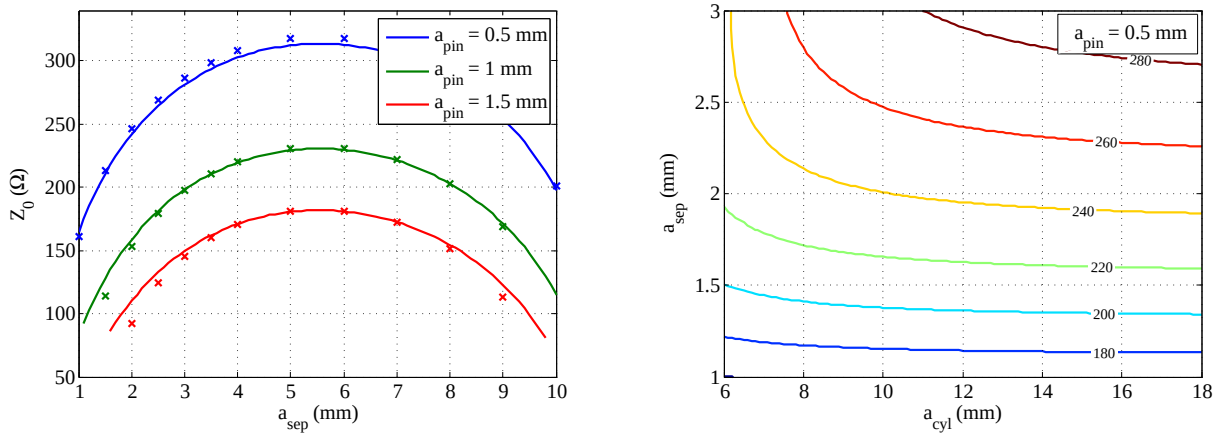

(a) **(b)**

Figure 3.15: Differential impedances of a twinaxial line for various dimensions.

In Fig. 3.15(b) the twinaxial line impedances are given for different values of a_{sep} and a_{cyl}, as

calculated with (3.6). Here the pin diameter is chosen as $a_{pin} = 0.5\ mm$ which is suited for the ridge thickness of $Throat1$ – a smaller value will only result in an unwanted higher impedance. It is clear that the diameter of the cylinder a_{cyl} has less of an influence on the impedance for a decreasing pin separation radius a_{sep}. Therefore, either a small a_{sep} or a larger a_{pin} is required to match the quadraxial line to the equivalent resistance of $Throat1$, i.e. $R_{eq} = 100\ \Omega$. None of these are however possible due to the physical restrictions caused by the ridge gap ($g = 1.87\ mm$) and ridge thickness ($t = 2.15\ mm$) on a_{sep} and a_{pin}, respectively. Thus the compromise is to take $a_{pin} = 0.5\ mm$ and then by using equation (3.5) we obtain $a_{sep} = 1.97\ mm$. From Fig. 3.15(b) it is clear that this transmission line has a characteristic impedance of 240 Ω. The result of this is illustrated in Fig. 3.16 where Γ_{in} of the equivalent model is given for different lengths of the high impedance quadraxial line. Note that for the case $L_{cyl} = 0$, the physical line which is de-embedded in simulation has a length of 3.5 mm. It is clear from Fig. 3.16 that the inclusion of the line length causes a significant mismatch. From an input match perspective, it is therefore imperative that L_{cyl} be as short as possible.

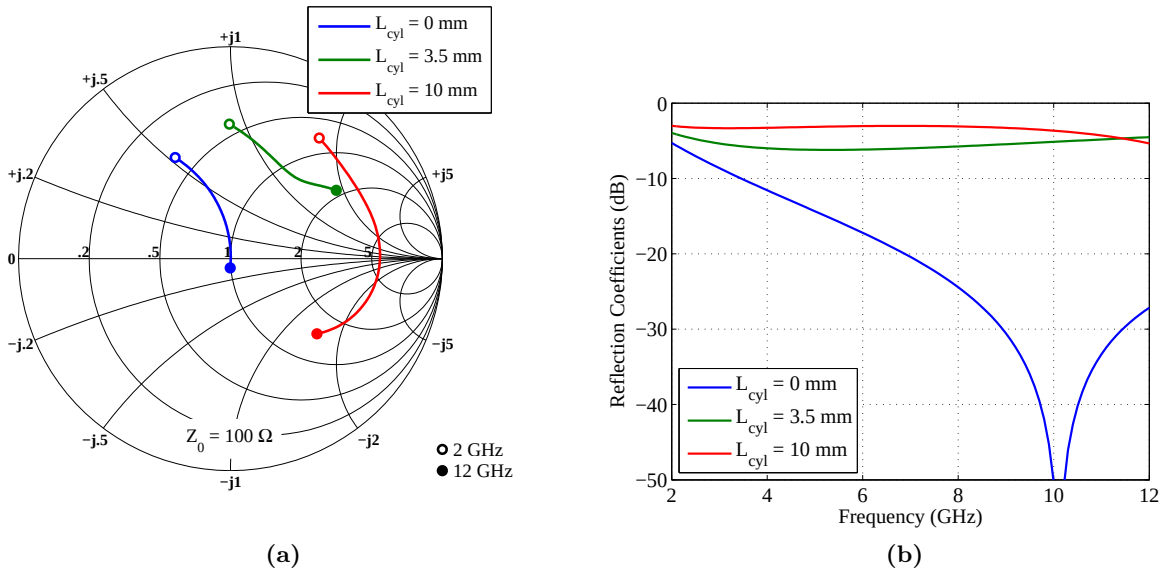

Figure 3.16: The input impedance of the equivalent circuit of $Throat1$ with the quadraxial feed for different transmission line lengths.

3.3.4 Modal considerations

As modal purity in the throat section is of a QRFH is very important, this section investigates the quadraxial feed in terms of the excitation of modes, as a function of the geometrical dimensions.

The dimensions of $Throat1$ and the quadraxial feed given in Tables 3.1 and 3.2, are used for the investigation of the geometrical influences on the modal content of the throat section. The modal content is obtained by considering the simulated magnitudes of the transfer coefficients, shown in Fig. 3.17(a), from the quadraxial excitation (port 1) to each significant ridge-loaded cylindrical mode in the throat (port 2), as discussed in Subsection 3.3.1. Note that only the differential mode of a single polarisation is excited in port 1 and therefore the notation of each S_{21} result indicates the specific excited mode in port 2. E.g. '$S_{21}[TE_{12}]$' refers to the transfer

coefficient from the differential TEM mode at port 1 to the ridge-loaded TE_{12} mode at port 2. The reference impedance for port 1 is taken as 75 Ω and the quadraxial line is de-embedded, in order to obtain a good input match as seen by S_{11}, so as to achieve an accurate representation of the modal excitations.

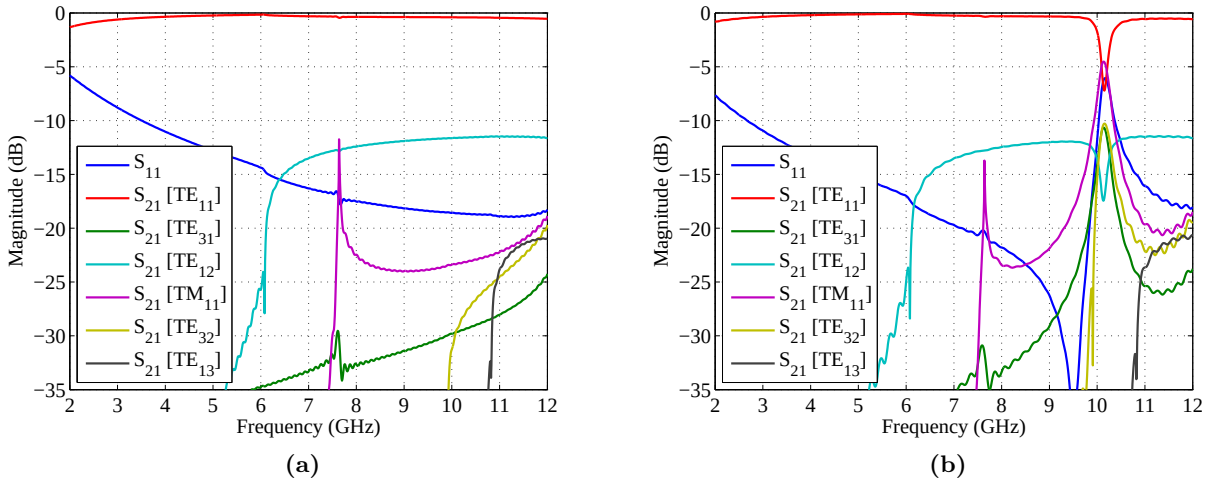

Figure 3.17: The simulated S-parameters of $Throat1$ excited with the quadraxial feed, where the dimensions in Table 3.2 are used. (a) $L_{cyl} = 3.5\ mm$ and (b) $L_{cyl} = 20\ mm$.

As expected, the TE_{11} mode is most strongly excited over the wide frequency band in Fig. 3.17(a), where $|S_{21}[TE_{11}]|$ is close to 0 dB. The second strongest mode is TE_{12} and has its cut-off at 6.1 GHz. In Chapter 4 it will be shown that the required field distribution in the aperture, for reflector feed applications, consists of modes with azimuthal dependence $m = 1$. Also, although the TE_{12}, TE_{13} and TM_{11} modes should be present in the aperture, these are not desired in the throat section (see Chapter 4). From Fig. 3.17(a) it is clear that all of these unwanted modes except for TE_{12}, are excited with $|S_{21}| < -15\ dB$.

As discussed in Subsection 3.3.3, L_{cyl} should be sufficiently short to avoid mismatching due to the high-impedance quadraxial line. This notion is also in favour of the modal performance. In Fig. 3.17(b) it is shown that with $L_{cyl} = 20\ mm$ a significant drop in $|S_{21}[TE_{11}]|$ exists at 10.2 GHz. Upon further investigation it is found that this resonance always coincides with $L_{cyl} \approx \lambda_g^{TE11}/2$ – where λ_g^{TE11} is the guided wavelength of TE_{11} in the quadraxial line. Therefore, to move this resonance outside of the operational band, it is imperative that $L_{cyl} < 16\ mm$ with $a_{cyl} = 11.4\ mm$.

A significant increase is observed in the excitation of higher-order modes with a larger size of the outer conductor a_{cyl}. The modal amplitudes of TE_{31}, TM_{11}, TE_{32} and TE_{13} are presented in Fig. 3.18 for different values of a_{cyl} over the frequency range from 6 to 12 GHz . It is clearly seen that for a larger value of a_{cyl} all of these modes have increased $|S_{21}|$ values. For $a_{cyl} = 15.5\ mm$ a peak in $|S_{21}|$ of these modes – except for TE_{13} – occurs around 11 GHz. Therefore it is established that $a_{cyl} = 11.4\ mm$ is a good trade-off between the modal purity and the input match – a smaller a_{cyl} decreases the distributed inductance L_p in the equivalent circuit, resulting in an increased mismatch at the lowest frequencies [see Fig. 3.14(a)].

Up to this point equation (3.5) is assumed for the distance between the opposing centre

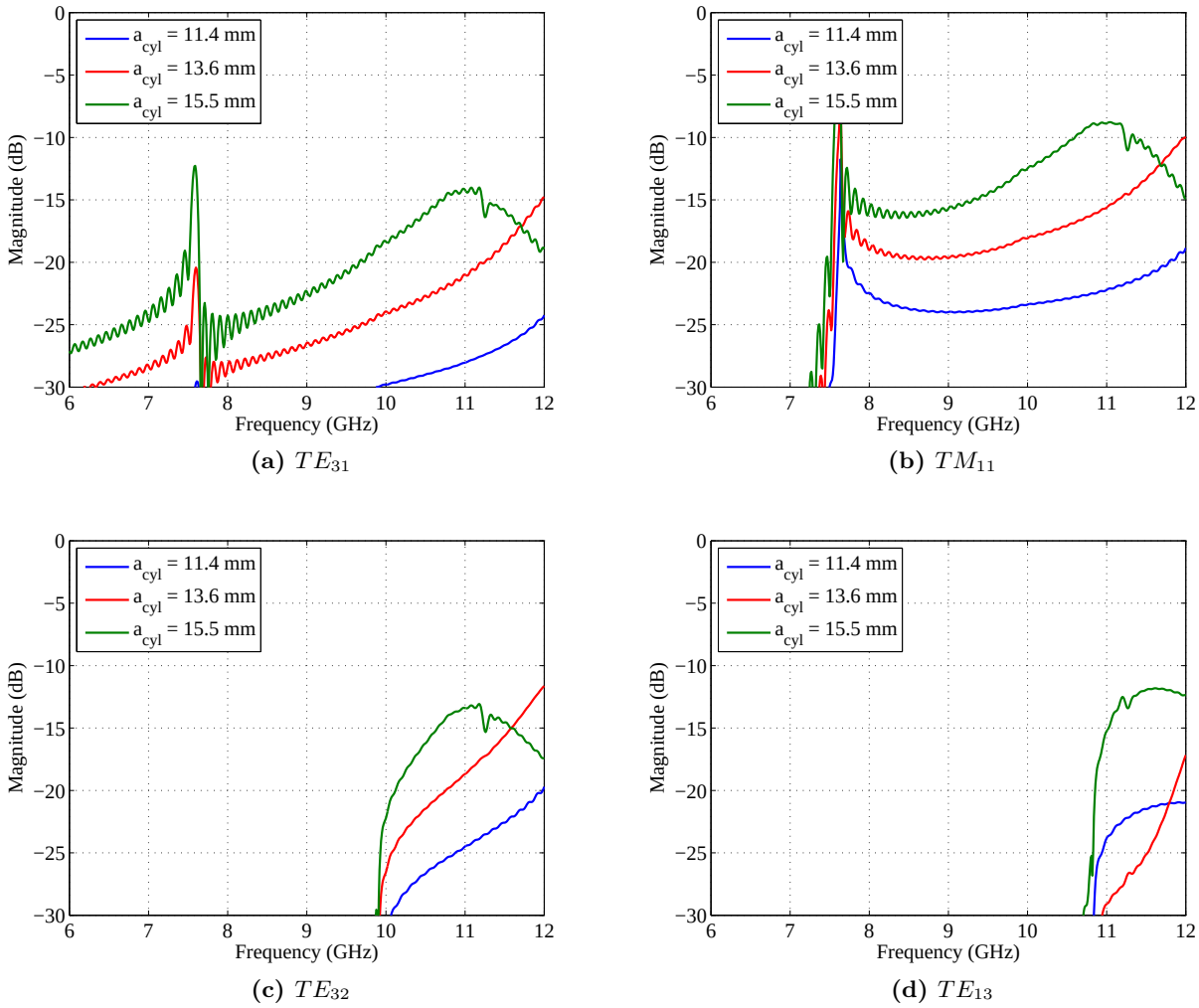

(a) TE_{31} **(b)** TM_{11}

(c) TE_{32} **(d)** TE_{13}

Figure 3.18: The transfer coefficients of different modes for varying values of a_{cyl}.

conductors of the quadraxial feed. In Fig. 3.19(a) the influence of a_{sep} on the modal content is illustrated for a fixed throat. Only the modes significantly affected by a larger pin offset, i.e. TM_{11} and TE_{32}, are shown here. It is clear that for the cases where a_{sep} is larger than the value calculated by equation (3.5), the two unwanted modes are comparable with the largest unwanted mode in Fig. 3.17(a), i.e. TE_{12} where $a_{sep} \approx 2\ mm$. It is also found that for a large a_{sep} the input impedance have a low resistance ($\pm 7\ \Omega$) and is highly inductive – therefore undesired for practical matching.

In Fig. 3.19(b) the magnitudes of S_{21} of TE_{12} and TE_{13} are given for different values of t. It follows therefore that a larger ridge thickness is beneficial for the suppression of both of these unwanted modes. It is worth mentioning that a thicker ridge also yields a larger bandwidth between the cut-off of the fundamental mode and the higher-order modes that are strongest excited in the throat section. The reason why thinner ridges are preferred with QRFHs, is because of the higher input impedances it produces with heavy loaded ridges to ensure wide single-mode operation – as seen from the values of the equivalent resistance in Fig. 3.12(a). E.g. if $t = 10\ mm$ is chosen with $Throat1$ it is found that $R_{eq} = 40\ \Omega$, and therefore a single-ended

termination of 20 Ω would be required.

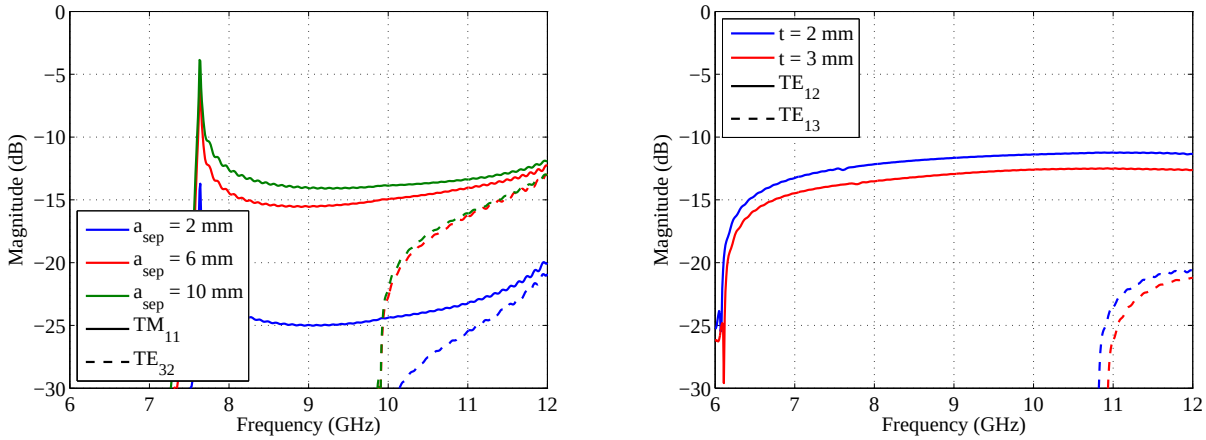

(a) (b)

Figure 3.19: The transfer coefficients of different modes for varying values of (a) a_{sep} and (b) t.

3.4 Modal evaluation of proposed excitation technique

The operational bandwidth of a waveguide is typically characterised by the separation between the cut-off frequency of the fundamental mode and that of the first excited higher-order mode. In a QRWG fed by a coaxial line, this higher-order mode is TE_{12} [49]. Therefore in many applications this limits the operational bandwidth to a ratio of about 3:1. Instead of applying modal suppression techniques [49] – which are typically narrowband solutions – new feeding techniques that do not excite the unwanted modes are desired.

In this section the modal performance of the proposed quadraxial feed is compared to that of the conventional feeding technique for QRFHs discussed in Subsection 3.2.1, which consists of a coaxial line as shown in Fig. 3.8. Thus, $Throat1$ and $Throat2$ are used to compare these two feeding techniques. The dimensions of the quadraxial feed in Table 3.2 are implemented with both of these throats.

The S-parameters of $Throat1$ are given in Fig. 3.20, with the coaxial feed used in (a) and the quadraxial feed in (b). Note that only the transfer coefficients above $-25\ dB$ are presented. In both cases TE_{11} is most strongly excited over the operational bandwidth; however, with the coaxial feed $|S_{21}[TE_{11}]|$ drops below 0 dB above 6.1 GHz. This drop is mostly caused by the transfer of energy from the TE_{11} mode to the TE_{12} mode, between 6.1 and 10.8 GHz, and to other higher-order modes above this range. The TE_{13} mode has its cut-off frequency at 10.8 GHz – which directly correlates with the sudden deterioration seen in the figure – and is evidently the strongest unwanted mode above this frequency. The TM_{ϕ} modes also have a large presence in the throat at the higher frequencies with a peak at 10.8 GHz. Recall that the TM_{ϕ} and TE_{χ} modes are combinations of degenerate modes as explained in Section 3.1. The peaks at 7.6 GHz in $|S_{21}|$ of the TM_{ϕ} modes, are due to the wave impedance of these transverse magnetic modes which are zero at the cut-off frequency.

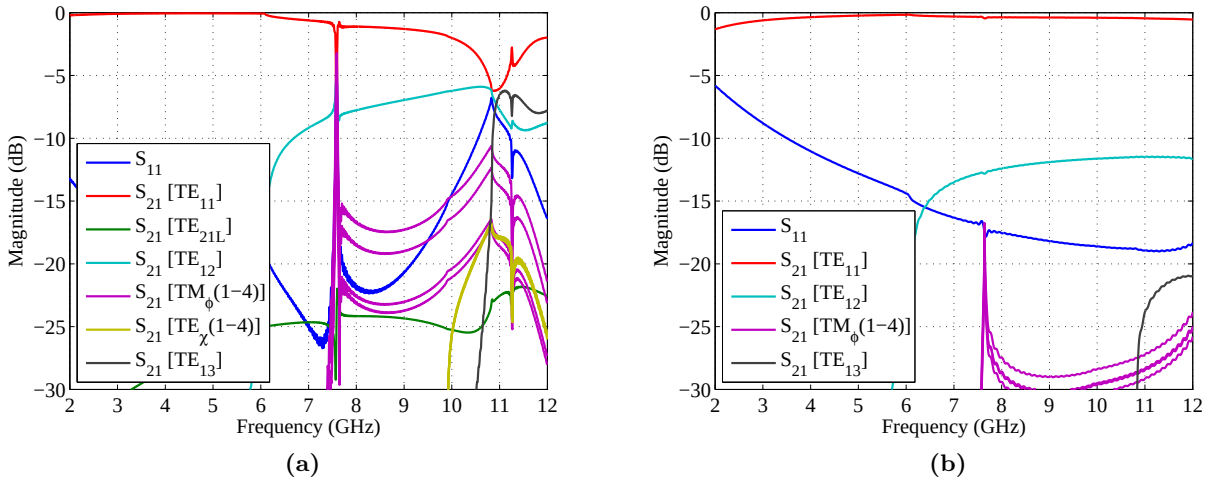

Figure 3.20: The simulated S-parameters of $Throat1$ excited with the (a) coaxial and (b) quadraxial feeds.

From the quadraxial feed results in Fig. 3.20(b) it is clear that all of these unwanted modes are suppressed. The TE_{12} mode is suppressed with as much as 5.5 dB while the TE_{13} mode is down by 16.5 dB. Therefore the result is that $|S_{21}[TE_{11}]| \approx 0$ dB over the entire frequency range. Another significant improvement with the quadraxial feed is that the even-order TE_{21L} mode is not excited. This excitation is a common problem with the coaxial feeding technique due to its asymmetries [47]. In Fig. 3.20(a) this mode is excited over the entire bandwidth with $|S_{21}[TE_{21L}]|$ close to -25 dB above 6 GHz. For a purely differential excitation of the quadraxial pin pairs this mode will not exist.

The same quadraxial feed is implemented in $Throat2$ with the S-parameters given in Fig. 3.21. The coaxial feed in Fig. 3.21(a) clearly excites fewer modes in the throat compared to the results of Fig. 3.20(a). This is because $Throat1$ is oversized compared to $Throat2$ – having both a larger outer diameter and ridge gap (see Table 3.1). Nevertheless, due to the presence of TE_{12} in $Throat2$, the magnitude of the TE_{11} mode does also decrease at the higher frequencies (above 7.3 GHz). From the quadraxial feed results in Fig. 3.21(b) it is seen that TE_{12} is suppressed with as much as 6.5 dB in comparison. It is interesting to note that in Fig. 3.21(a) the orthogonal TE_{11} mode is excited over the entire bandwidth at -20 dB, indicated by $S_{21}[TE_{11\perp}]$. This mode is negligibly small with the quadraxial feed – therefore mitigating leakage into the orthogonal polarisation of the throat section. Furthermore, the even-mode TE_{21L} is also excited by the coaxial feed in $Throat2$, with a constant level of -21 dB over the entire bandwidth.

Following these results, it is clear that the quadraxial feeding technique improves the modal purity of both $Throat1$ and $Throat2$, compared to the performances of the coaxial feeds. In Chapter 4 the implication of a pure mode excitation for QRFHs is discussed.

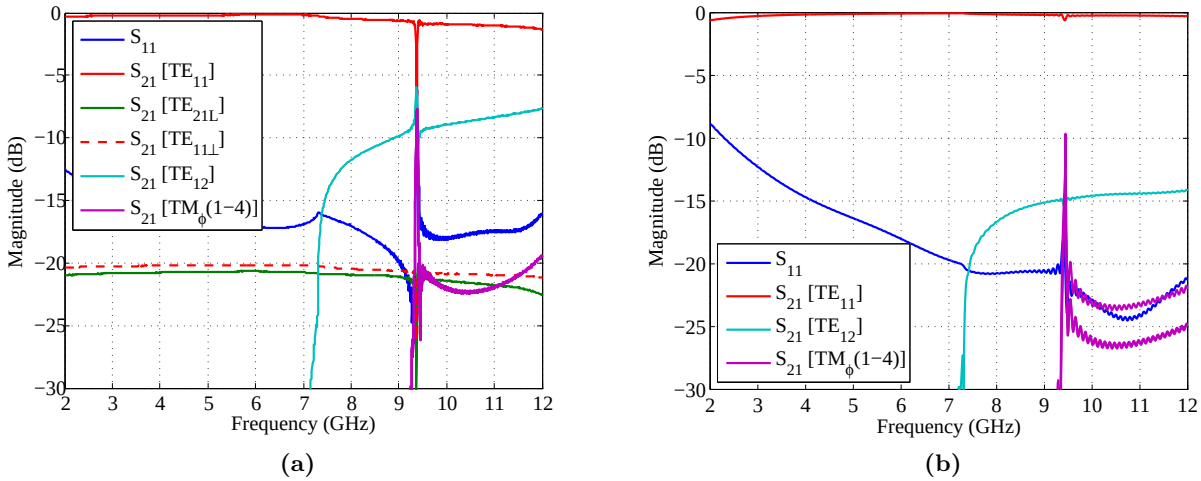

Figure 3.21: The simulated S-parameters of *Throat*2 excited with the (a) coaxial and (b) quadraxial feeds.

3.5 Conclusion

In this chapter a new feeding technique is proposed for a circular QRFH antenna. An equivalent single-mode circuit is derived that gives insight into the operation of the quadraxial feed, and also allows fast synthesis of optimal feeding designs for QRFHs.

Two different QRWGs are used to demonstrate the performance of the proposed feeding technique and are compared with the conventional coaxial feed. Following the modal analysis it is clear that the quadraxial feed suppresses all the unwanted higher-order modes – more than is achieved by the coaxial feed – and is therefore an attractive solution for the pure-mode excitation of a QRFH.

Chapter 4

Modal Properties of the QRFH Antenna

In 1974 the first quadruple-ridged horn (QRFH) was reported by King [5].[1] Since then various QRFH designs have been reported, though all utilising analytical functions for the tapering profiles which are refined through optimisation. In [2] the modal content in the aperture of a complete QRFH employed with a coaxial feed, is considered. Very few authors have explicitly made use of the properties of specific modes for the enhancement of the radiation properties.

The purpose of this chapter is therefore to explore the QRFH from a modal perspective. To control individual modes the flared section is excited with QRWG pure-modes, as discussed in Section 3.1. The resulting aperture field distribution is approximated by a series expansion of higher-order cylindrical modes. The interactions of these modes with the far-field performance are discussed and various radiation effects are considered.

4.1 Modal aspects of QRFHs

The cross-section view of the flared section of a typical QRFH is shown in Fig. 4.1. It consists of an aperture flare (which improves the match with free-space), tapered sidewall and ridges, and an input section which has the cross-section of the throat to which the feeding network, as discussed in the previous chapter, is connected. The flaring of the QRFH has two purposes – it ensures a smooth transition between the QRWG and free-space, and it generates the higher-order modes which are required for the consistent radiation over a wide bandwidth.

The beamwidth of the radiation patterns is largely determined by the flaring angle of the ridge taper towards the aperture, with the aperture diameter having a secondary influence according to [2]. In order to maintain a constant beamwidth as the aperture size increases electrically with frequency, the circumference of the field distribution in the aperture has to become smaller (assuming constant phase). One such desired distribution for a 6:1 bandwidth is reported in [2], where the modal content that would ensure this distribution is determined with a technique proposed in [55]. It is shown that only modes with first-order azimuthal dependence

[1] Before this the double-ridged horn has been used for various applications. The modal content is however rather different than with quadruple-ridged horns.

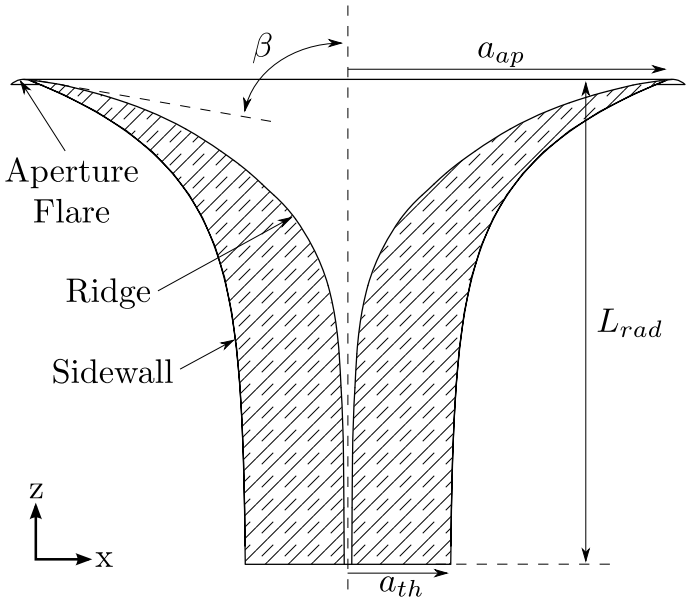

Figure 4.1: Cross-section view of the flared section of a QRFH.

(i.e. $m = 1$) are required to establish the rotational symmetry, which also corresponds to that of the multi-mode horns reported in [56]. The TE_{11} mode should be the most dominant with declining power as the frequency increases and the higher-order modes, in declining order of power, should be TM_{11}, TE_{12}, TM_{12}, TE_{13}, etc. Due to the two-fold symmetry of the required aperture field distribution, all even-order modes are undesired (i.e. TE_{mn} and TM_{mn} where $m = 0, 2, 4, \ldots$).

The aperture modal technique[55] is of interest when considering the various modes required to produce a certain radiation pattern; however, to excite such a specific distribution with a QRFH is not a trivial task. Due to the complexity of the problem – with a lack of closed-form solutions for ridge-loaded modes – no analytical approach exists in literature by which the modal excitations can be controlled. With conical smooth-wall horns, excited with a TE_{11} mode in the throat section, it is well known that abrupt or gradual changes in the diameter will cause $m = 1$ type modes to be excited exclusively [56]. These waveguide junctions have been analysed in [57, 58, 59] and are typically employed in techniques such as modal-matching, in order to synthesise the sidewall profile that would produce the desired aperture distribution [60]. In [61] spherical modes are implemented in a modal-matching procedure for a corrugated horn, in which phase cancellation is used to reduce the sidelobe levels. These mode-controlling techniques typically restricts the operation of the antenna to narrow bandwidths – e.g. a mode might be used at one frequency to suppress the cross-polarisation produced by another mode; however, at a different frequency the phases will change relative to each other and consequently may lead to the opposite effect in cross-polarisation.

In order to achieve the multi-modal wideband operation of a QRFH, analytical functions are typically used for the tapering profiles of both sidewall and ridges. The exponential function is the most widely used for ridge tapers in both dual- and quad-ridged horns operating over wide frequency ranges [62, 5, 63, 64, 49, 50]. It is reported in [3] that the elliptic function reduces the beamwidth variation of a QRFH over a 4:1 bandwidth, although this is not necessarily

applicable for the excitation of aperture modes at frequencies above this range. In [65] different profile functions consisting mainly of those reported in [66] for conical horns, are implemented for QRFH feed designs with different subtended angles over 6:1 bandwidths.[2] The optimal profile values of both sidewall and ridges are determined through search functions employed with full-wave simulations of the complete QRFH configuration, where the coaxial feeding is included from the start. According to these studies the most promising profile functions are found to be exponential, elliptical, x^p and tan^p [2].

Among the QRFHs intended as reflector feeds for radio telescopes, the present state-of-the-art is an antenna which operates from 2 to 12 GHz with a nominal 10 dB beamwidth of 85°, achieving better than 50% aperture efficiency in a shaped dual-reflector system [2]. For this design the exponential function is used for both sidewall and ridge profiles, which is defined with reference to Fig. 4.1 as

$$x = A(c_1 e^{Rz} + c_2) + (1 - A)\left[a_i + (a_o - a_i)\frac{z}{L}\right], \tag{4.1}$$

where

$$c_1 = \frac{a_o - a_i}{e^{RL} - 1} \tag{4.2}$$

and

$$c_2 = \frac{a_i e^{RL} - a_o}{e^{RL} - 1}. \tag{4.3}$$

Here the parameter A can be varied between 1 and 0 to change the linearity of the profile, a_i and a_o are respectively the radii of the input and output sections of the profile (i.e. at the throat and aperture), R is the exponential opening rate (or taper rate) and L is the length of the profile.

The linear section of the profile was first introduced in [62] for improvement of the input match of a square dual-ridged horn. This is not necessarily beneficial at all frequencies for a wide operational bandwidth and therefore $A = 1$ is assumed in this chapter to simplify the analysis. The flared angle, indicated in Fig. 4.1 for the ridge profile, can then simply be calculated as

$$\beta = tan^{-1}\left[\frac{Re^{RL}}{e^{RL} - 1}(a_o - a_i)\right]. \tag{4.4}$$

4.2 Aperture radiation

A technique which was first proposed by Ludwig [55] for the analysis and effectively the synthesis of circular aperture radiation patterns, is described in this section. The technique allows one to calculate the modal content in a radiating aperture from any set of far-fields. This is particularly useful in obtaining insight into the modal content produced by a QRFH, and is therefore used throughout the remainder of this dissertation.

4.2.1 Circular aperture technique

The electric field distribution in a circular aperture can be represented by a Fourier-expansion of cylindrical modes as

[2] With the high-gain horns bandwidth ratios up to 7:1 are achieved.

$$F(\rho,\phi) = \sum_{m=0,n=1}^{M,N} a_{mn}\, E^{TEmn} + b_{mn}\, E^{TMmn} \tag{4.5}$$

with zero fields for $\rho > a$, where a is the aperture radius defined in a cylindrical coordinate system. Here E^{TEmn} and E^{TMmn} are the transverse electric and transverse magnetic fields [41], respectively with complex amplitude coefficients a_{mn} and b_{mn}.

By applying the far-field transformation to each of these source functions the radiated fields of each mode can be derived [67]. The radiated electric fields of the transverse electric modes are given as

$$G_{\theta}^{TEmn}(u,\phi) = -a_{mn}\, j^m\, m\, J_m(\chi_{mn}^{'})\, \frac{J_m(u(\theta))}{u(\theta)}\, cos\, m\phi\ \psi(\theta) \tag{4.6}$$

and

$$G_{\phi}^{TEmn}(u,\phi) = a_{mn}\, j^m\, \chi_{mn}^{'2}\, J_m(\chi_{mn}^{'})\, \frac{J_m^{'}(u(\theta))}{\chi_{mn}^{'2} - u^2(\theta)}\, sin\, m\phi\ \psi(\theta), \tag{4.7}$$

while the electric fields of the transverse magnetic modes are

$$G_{\theta}^{TMmn}(u,\phi) = b_{mn}\, j^m\, \chi_{mn}\, J_m^{'}(\chi_{mn})\, \frac{u(\theta)\, J_m(u(\theta))}{\chi_{mn}^2 - u^2(\theta)}\, cos\, m\phi\ \psi(\theta). \tag{4.8}$$

Here

$$u(\theta) = k\, a\, sin\theta \tag{4.9}$$

and

$$\psi(\theta) = \frac{k\, a^2}{2}\,(1 + cos\theta)\,, \tag{4.10}$$

where χ_{mn} is the nth zero of the Bessel function (J_m) of the first kind of order m; while the apostrophe represents the derivative. The polarisation here is aligned with the x-axis, though the orthogonal set of modes can also be defined by simply rotating the fields. Therefore the E-plane is defined for $\phi = 0°$ and the H-plane for $\phi = 90°$. Note furthermore that equations (4.6)-(4.8) are simplified in that the propagation constant k is assumed to be equal to that of free-space [55], i.e. $k = 2\pi/\lambda_0$.

For the inverse problem, [55] shows that given a far-field $G(u,\phi)$ which radiates from an ideal circular aperture, the complex mode coefficients can be derived through algebraic manipulation as

$$a_{mn} = -A_{mn} / \left(j^m k\, J_m(\chi_{mn}^{'})\, \chi_{mn}^{'2} a^2\right), \tag{4.11}$$

$$b_{mn} = B_{mn} / \left(j^m k\, J_m^{'}(\chi_{mn})\, \chi_{mn} a^2\right), \tag{4.12}$$

where

$$A_{pq} = \frac{2}{1 + \sqrt{1 - \left(\frac{\chi_{pq}^{'}}{ka}\right)^2}}\, \frac{2\chi_{pq}^{'}}{\pi J_p^{''}(\chi_{pq}^{'})} \int_0^{2\pi} G_{\phi}(\chi_{pq}^{'},\phi)\, sin\, p\phi\ d\phi, \tag{4.13}$$

$$B_{pq} = \frac{2}{1 + \sqrt{1 - \left(\frac{\chi_{pq}}{ka}\right)^2}}\, \frac{2}{\pi J_{p+1}(\chi_{pq})} \int_0^{2\pi} G_{\theta}(\chi_{pq},\phi)\, cos\, p\phi\ d\phi. \tag{4.14}$$

4.2.2 Reference distribution for the QRFH

To illustrate the use of Ludwig's procedure, a far-field pattern, indicated by the black lines in Fig. 4.2, is chosen as a reference pattern in Chapter 5. This is obtained from a QRFH which has an aperture radius of 105 mm, that produces an aperture efficiency of 72% in the specific SKA reflector system. To determine the modal content of this reference pattern, the complex coefficients of the TE and TM aperture modes are calculated from the radiated fields using equations (4.11) and (4.12), over a frequency range from 2 to 12 GHz. The magnitudes of the coefficients are given in Fig. 4.3, where each coefficient is normalised with the sum of all the coefficient magnitudes of the modes that are above cut-off.

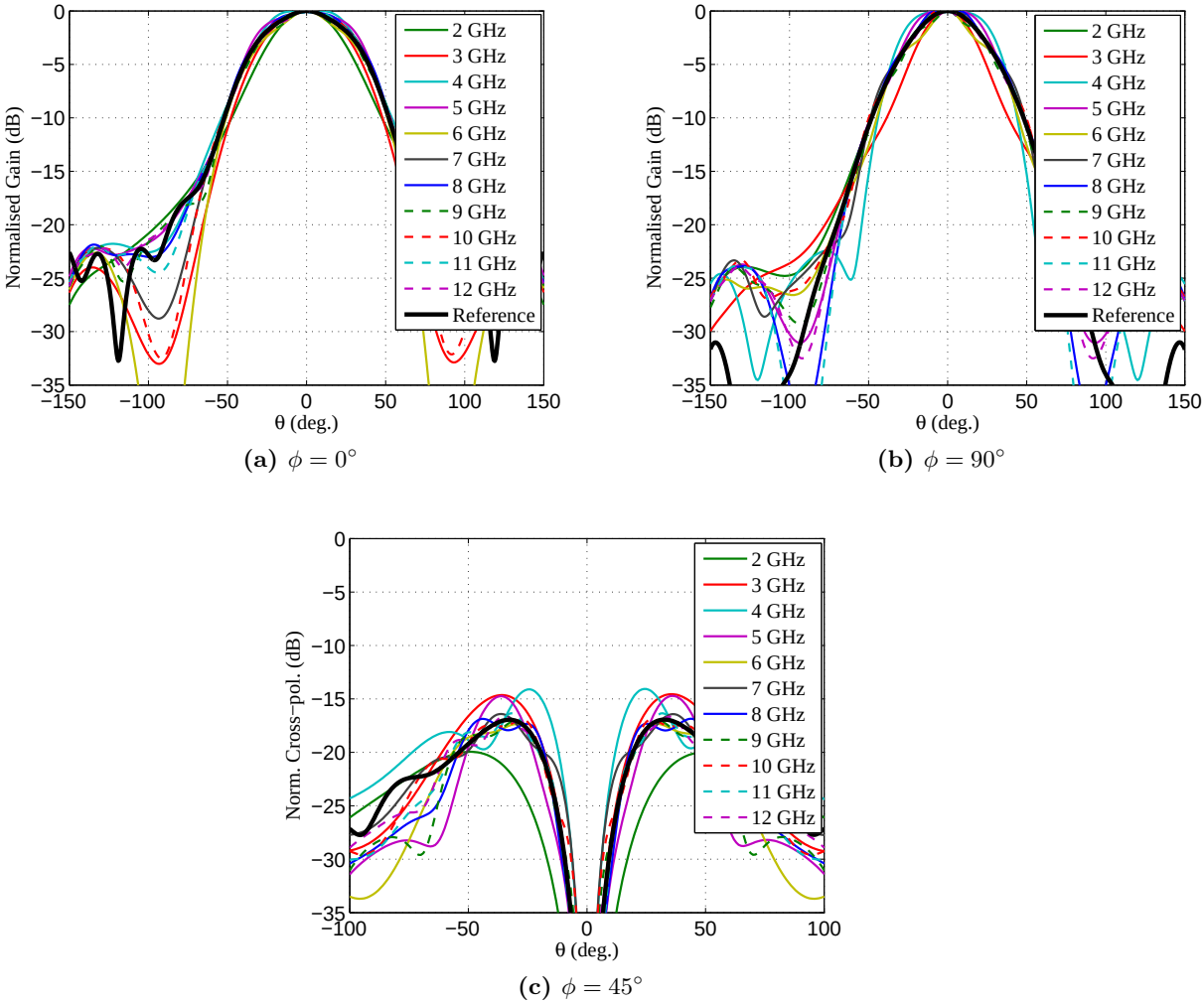

(a) $\phi = 0°$ **(b)** $\phi = 90°$

(c) $\phi = 45°$

Figure 4.2: The (a)-(b) co-polar and (c) cross-polar far-fields of the reference pattern and of the calculated complex modal coefficients, with magnitudes shown in Fig. 4.3.

From Fig. 4.3 it is clear that the TE_{11} mode is dominant over most of the frequency range, followed by TM_{11}. As expected, the modes with non-zero magnitudes are those with the azimuthal dependence $m = 1$. Because the reference pattern is produced with an actual radiator, there are also a few modes present with order $m = 3$; however, these account for less than 2.8% of the total aperture distribution at a single frequency.

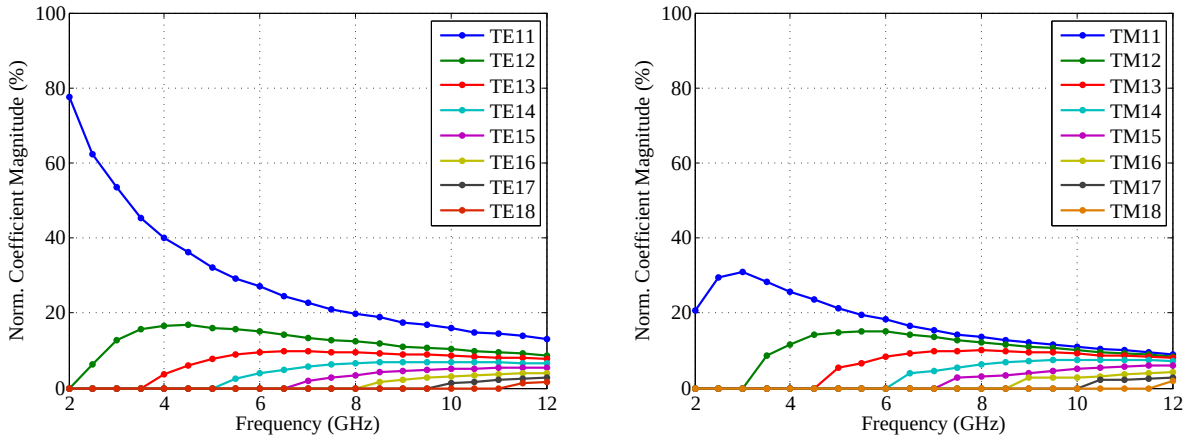

(a) TE mode coefficients **(b)** TM mode coefficients

Figure 4.3: The normalised coefficient magnitudes calculated from the reference pattern in Fig. 4.2, of modes in an aperture with a diameter of 210 mm.

To illustrate the validity of this technique, the modal coefficients of all the modes above cut-off are used in equations (4.6)-(4.8) to reproduce the far-field patterns as shown in Fig. 4.2. It is found that the largest deviations occur at the lower frequencies, compared to the original pattern depicted by the thick black line. This observation could be ascribed to a number of things. Firstly the use of free space k in equation (4.9), as proposed in [55], will incur a deviation particularly at the low frequency end, as the difference between the guided wavelength (λ_g) and the free-space wavelength (λ_0) become more marked as the cut-off frequency is approached, seen in equation (4.15).

$$\frac{\lambda_g}{\lambda_0} = \frac{f}{\sqrt{f^2 - f_c^2}} \tag{4.15}$$

Due to the decreasing power in the higher-order modes at the high frequencies, this error is less pronounced in that region.

The series expansion is also at best an approximation of the full-wave simulated horn patterns. Effects that are not included are phase changes over the aperture, numerical artefacts of calculations and diffraction. Mode coefficients are calculated by integrating the far-fields over ϕ for an angle θ_i, as seen from equations (4.13) and (4.14). This angle is obtained by satisfying the equations $\chi'_{mn} = k\,a\,sin\,\theta_i$ and $\chi_{mn} = k\,a\,sin\,\theta_i$ for the TE_{mn} and TM_{mn} modes, respectively. This reduces to the simple equation

$$\theta_i = sin^{-1}\left(\frac{f_c}{f}\right). \tag{4.16}$$

It follows that close to cut-off the integration angle becomes large (i.e. $\theta_i \to 90°$) and with it the effects of diffraction should also increase in the far-fields.

Therefore, both the effects of the assumed propagation constant and neglected aperture diffraction, prove to be more significant for modes close to cut-off. From 2 and 4 GHz the TM_{11} and TE_{12} modes carry significant power, and therefore because $f_c^{TM11} = 1.7\ GHz$ and $f_c^{TE12} = 2.4\ GHz$, the deviations found in the far-fields in Fig. 4.2 are largest at these frequencies.

Additionally there is the assumption that the aperture only contains cylindrical modes of an infinitely long cylinder. The implication is therefore that no evanescent modes are considered in the aperture. Thus, in order to ensure that there are no evanescent modes, the cut-off frequencies of all modes should decrease monotonically in the flared section from the throat to the aperture, which is indeed the case for this particular horn.

4.2.3 Example of modal radiation

To illustrate how modal content can be utilised to design antenna patterns, a simplified example of how a pattern can be improved is given in this subsection. The aperture diameter used is $2.15\lambda_0$ and corresponds to one of the QRFH designs at 3 GHz in the following section. The first four modes that are typically excited in the aperture of a QRFH, are calculated with equations (4.6)-(4.8) and shown in Fig. 4.4.

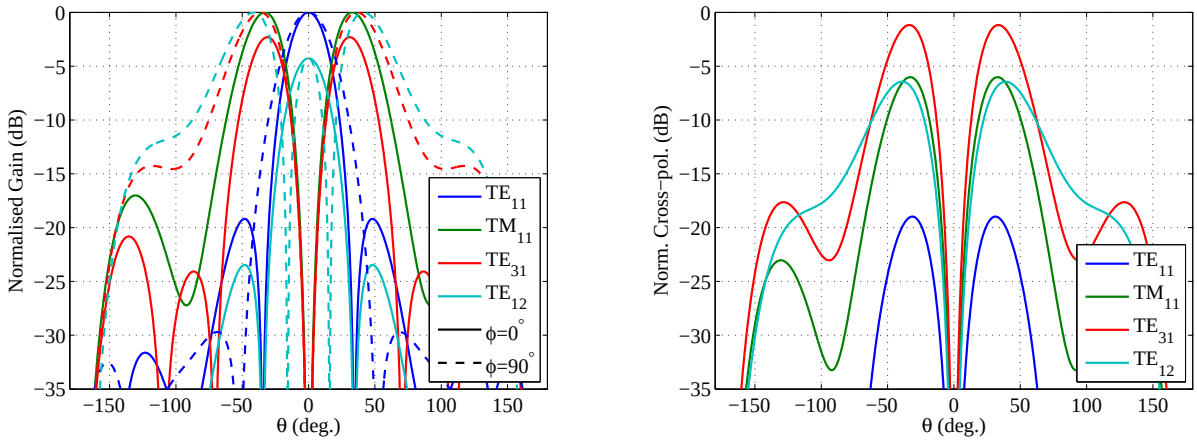

Figure 4.4: The (a) co- and (b) cross-polarisation patterns of individual modes in an aperture with diameter $2.15\lambda_0$.

From the co- and cross-polarisation patterns in Figs. 4.4(a) and (b) respectively, it is clear that the TE_{11} mode produces the best radiation characteristics, as it has its main beam at boreside, with low sidelobes. In order to obtain a wider beamwidth more modes are however required. By adding the TM_{11} mode in phase with TE_{11}, this beamwidth increase would be achieved in the E-plane. As seen from equation (4.8) the radiation of odd-mode TM field distributions have no electric fields in the H-plane. Therefore either TE_{31} or TE_{12} could be used to synthesise the beamwidth in this plane.

In Table 4.1 a few different sets of modal coefficients are given to illustrate the effects of changing the modal content in a given aperture. Note that only the relative magnitude of each coefficient is given here – with the assumption that the modes are all excited in phase at the aperture. The far-field patterns of each set are shown in Fig. 4.5. The first set is calculated from the far-field results at 3 GHz of $Horn1$ – introduced in the next section. Here the desired beamwidth is 100° and therefore in the H-plane it is not satisfied. The peak cross-polarisation is -2.9 dB and should also be lowered. By eliminating the unwanted TE_{31} mode and

redistributing its power between TE_{11} and TE_{12}, as illustrated by the second set of coefficients, the cross-polarisation is reduced as shown in Fig. 4.4(b). The H-plane beamwidth of $set2$ is still about 110° and therefore the modal distribution among the TE modes are not optimal. From the radiation patterns in Fig. 4.4(a) it is clear that by increasing the TE_{11} mode, a narrower beamwidth should be ensured. Therefore, in the third set of coefficients the unwanted TM_{31} mode is eliminated and added to TE_{11}. Note also that TM_{11} is reduced slightly in order to equalise the affect of TE_{11} on the E-plane beamwidth. The result is a beamwidth in both principle planes of 100° with a cross-polarisation below $-20\ dB$.

Table 4.1: Different sets of modal coefficients with their radiation patterns shown in Fig. 4.5. The percentages indicate the magnitude of the modal coefficient as a fraction of the summed magnitudes of all modes present.

	TE_{11}	TM_{11}	TE_{31}	TE_{12}	TM_{31}
$set1$	31%	35%	17%	7%	10%
$set2$	40%	35%	0	15%	10%
$set3$	53%	32%	0	15%	0

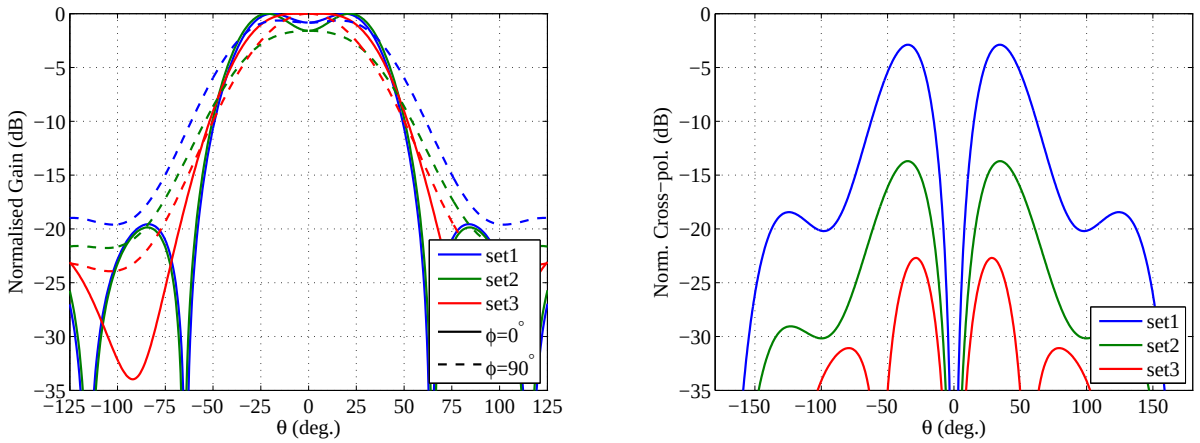

(a) (b)

Figure 4.5: The (a) co- and (b) cross-polarisation patterns of different sets of modal distributions, with coefficients given in Table 4.1, for an aperture diameter of $2.15\lambda_0$.

In conclusion, this technique proves to be helpful not only in synthesising far-fields, but also in gaining insight into the modal contributions. In the next section the focus shifts to the modal contributions of the throat in a QRFH.

4.3 Evaluation of QRFHs with different excitations

In Chapter 3 the modal content of different throat sections was evaluated with the proposed and conventional excitation techniques. The quadraxial feed showed better suppression of the unwanted higher-order modes in two different QRWGs, compared to the coaxial feed. The implication of a pure-mode excitation in a QRFH is unclear and therefore in this section it is investigated.

4.3.1 Detrimental modal effects in QRFHs

Although a QRFH is often presented in the literature as a (near-) constant beamwidth antenna with about 6:1 bandwidth [2], its beamwidth in the H-plane varies with as much as a factor of 3 over such a frequency band. From the investigations for this dissertation it was found that the rapid beam narrowing is in many cases directly correlated to the modal content in the throat section, generated by the coaxial feed. This detrimental effect cannot necessarily be corrected by standard (narrowband) mode suppression techniques – such as the metal ring introduced in the throat section of a QRFH design in order to suppress the TE_{12} mode [49].

High cross-polarisation is mostly due to certain aperture modes, as illustrated in the previous section, and not as much the difference between the principle plane patterns – as in the case of a pure BOR_1 pattern described by equation (2.11).

In [56] it is reported that the presence of the TM_{12} and TE_{12} modes in the aperture, respectively causes sidelobes in the E- and H-planes.

4.3.2 Design of evaluation horns

In order to evaluate the effectiveness of the feeding sections for QRFHs, four different horns are designed and optimised here. Following the literature review on existing QRFHs, the dimension space and relevant goals are accordingly chosen for the optimisation of the flared sections, which are executed using CST-MWS. The design choices are as follow:

(i) In order to continue the evaluation in Chapter 3, both $Throat1$ and $Throat2$ are considered with dimensions given in Table 3.1.

(ii) Different horns employed with these throat dimensions are optimised to produce different beamwidths.

  (a) The low-gain horn is optimised for a nominal 10 dB beamwidth of 100° (corresponding to the SKA requirements).

  (b) The high-gain horn is optimised for a nominal 10 dB beamwidth of 60°.

(iii) The exponential function (4.1) is used for both the sidewall and ridge profiles – corresponding to the optimal tapers used in [65].

The result is therefore four different horns as indicated in Table 4.2, which are optimised for constant beamwidths in the E- and H-planes over the entire 6:1 bandwidth. They are all excited with a pure TE_{11} mode, for which the input reflection coefficient is less than -15 dB. In order to find the optimal set of dimensions for these performance goals, the Covariance Matrix Adaptation Evolutionary Strategy in CST-MWS is used [42]. This algorithm uses a statistical model to sample the dimension space, which allows the robustness of a global search without getting stuck in a local minimum.

The initial dimensions used for the optimisations are those of the QRFH designs reported for $Throat1$ in [52] and $Throat2$ in [2, 65]. The parameter space is chosen according to the beamwidth specifications. For a narrower beamwidth the flared angle of the ridges is decreased

Table 4.2: The dimensions of the different optimised flared sections.

Description	L_{rad}	a_{ap}	R_{ridge}	R_{side}	β_{ridge}	$L_{rad}/2a_{ap}$
$Horn1$ – Low-gain, $Throat1$	202.4 mm	107.7 mm	0.0454	0.0350	78°	0.94
$Horn2$ – Low-gain, $Throat2$	140.0 mm	92.7 mm	0.0460	0.0309	76°	0.76
$Horn3$ – High-gain, $Throat1$	323.7 mm	116.1 mm	0.0153	0.0169	60°	1.39
$Horn4$ – High-gain, $Throat2$	278.2 mm	124.6 mm	0.0159	0.0146	63°	1.12

while the aperture size a_{ap} is increased. In [3] it is shown with the elliptic taper function, that a smaller horn length to aperture diameter ratio ($L_{rad}/2a_{ap}$) widens the beamwidth. This is also in agreement with smooth-wall conical horns, where the optimal gain decreases with smaller length-to-aperture ratios [68]. Therefore, the first four parameters in Table 4.2 are optimised for each horn with the resulting values as listed. The ridge thickness is naturally determined by the throat section.

It is interesting to note that for both low- and high-gain horns, the ones employed with $Throat2$ are smaller than their counterparts using $Throat1$, which evidently also corresponds to the difference in throat sizes. Furthermore, the flared angles are smaller in the high-gain horns as expected. In the next subsection the performances of these horns are discussed.

In Table 4.3 the results are summarised for each of the optimised horns fed with the TE_{11} mode. The mean value of the beamwidth in each principle plane is calculated and given here. In order to illustrate the beamwidth variation over frequency, the standard deviation is calculated with 21 frequency samples that are linearly taken over the bandwidth.

Table 4.3: The results of the different horns fed with the TE_{11} mode is listed column wise as, the 10 dB beamwidths in the E- and H-planes, the normalised peak cross-polarisation levels in the D-plane, and the difference between the maximum to minimum phase centres. These results are all calculated with 21 frequency samples over the operational bandwidth.

	E-plane beamwidth		H-plane beamwidth		D-plane peak X-pol.		Phase centre
	μ	σ	μ	σ	μ	σ	Δ
$Horn1$	113°	6.6°	73°	20.3°	−10.6 dB	2.7 dB	18 mm
$Horn2$	109°	7.5°	74°	20.9°	−10.3 dB	2.7 dB	37 mm
$Horn3$	68°	6.0°	57°	17.0°	−12.5 dB	2.5 dB	106 mm
$Horn4$	74°	5.3°	57°	16.0°	−12.4 dB	2.0 dB	80 mm

The standard deviation is defined as

$$\sigma = \sqrt{\frac{1}{N}\sum_{n=1}^{N}(x_n - \mu)^2}, \tag{4.17}$$

where the mean value is

$$\mu = \frac{1}{N}\sum_{n=1}^{N} x_n. \tag{4.18}$$

Here x indicates the sample value, n is the index for each sample and N is the total number of samples. In Table 4.3 there is a notable difference in the beamwidths between the principle planes, where the H-plane values for the low-gain horns are significantly lower than the required optimisation goals. It is also noted that the standard deviation is about 3 times that in the

E-plane. This is mainly due to a significant drop in beamwidth above about 5 GHz. Note that all of these horns attained $|\Gamma_{in}| < -15$ dB for the pure-mode excitations, with the exception of $Horn4$ which peaks at -13 dB. If this constraint is lowered to -10 dB it is found that better beamwidth stability is achievable.

Furthermore, it is seen from the second to last column in Table 4.3 that the high-gain horns have lower peak cross-polarisation over the bandwidth, compared to the low-gain horns. Overall the high-gain horns have better far-field performance; however, their phase centres vary more than with the low-gain horns and are therefore not that desirable as reflector feeds. It is interesting to note that as the flare angle of each horn decreases (see Table 4.2), the variation of the resulting phase centre increases. The largest variation is normally at the lowest frequencies – specifically at 2 GHz as shown in the next subsection – where only the TE_{11} mode is excited in the horn.

In conclusion, the low- and high-gain horns respectively have very similar results regardless of the throat section. Therefore without being redundant, only $Horn1$ and $Horn3$ are evaluated in the next subsection with the different excitation techniques. Recall that $Throat1$ is over-moded and therefore the modal affects are more pronounced. As shown in Fig. 3.21, the cut-off frequencies of the unwanted modes in $Throat2$ are higher and also slightly more suppressed.

4.3.3 Far-field performance for different excitation techniques

To evaluate the quadraxial and coaxial feeds – with dimensions respectively given in Table 3.1 and [52] – both are connected to $Horn1$ and $Horn3$ to form four QRFH antennas. Note that the quadraxial feed is only excited in one differential-mode. The length of the uniform waveguide in the throat is specified in [52] as 7.5 mm. This length has secondary effects in the far-fields and is mostly of significance to the input match. Therefore, 7.5 mm is used for both of these feeding structures.

The 10 dB beamwidths in the E- and H-planes of these four QRFHs are shown Fig. 4.6. The low-gain horn in Fig. 4.6(a) has large variations as a function of frequency, and even more so as a result of the coaxial feed. With the quadraxial feed the beamwidth in the H-plane has a constant offset over the frequency range with that of the E-plane, while the coaxial feed yields rapid variations with frequency in both planes. The latter is directly correlated with the unwanted modes propagating in the throat above 6 GHz. The high-gain horn in Fig. 4.6(b) shows similar variations, with the quadraxial feed showing more stability.

In Fig. 4.7 the gain and normalised peak cross-polarisation levels are shown. The gain of $Horn1$ is above 10 dB for both excitations, except around 3 GHz, while the coaxial feed yields rapid variations above 6 GHz. The cross-polarisation obtained with the coaxial feed peaks with -2.7 dB at 3 GHz and at 10.25 GHz it is as high as -1.2 dB. The former is mostly due to the strong presence of TE_{31} in the aperture, as illustrated in Section 4.2.3. The latter is difficult to ascribe to a single cause due to the large amount of excited modes. With $Horn3$ the TE_{11} mode is strongly excited at the lowest frequencies and therefore the cross-polarisation is much better than obtained with $Horn1$. The quadraxial feed maintains a cross-polarisation level below -10 dB over the entire bandwidth as seen in Fig. 4.7(b), while the coaxial feed peaks at 11 GHz with -2.6 dB. The results of the latter are in agreement with the results in [2] for a

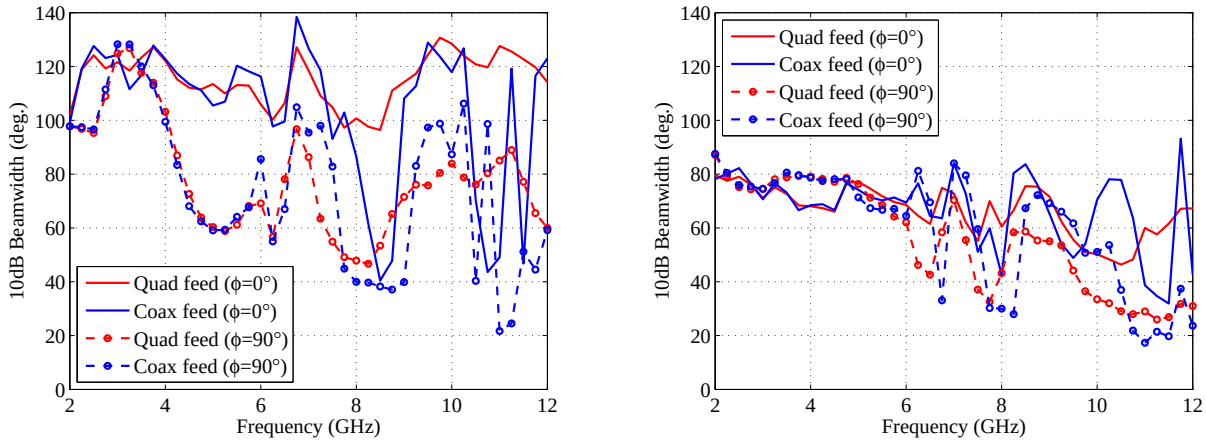

(a) $Horn1$ **(b)** $Horn3$

Figure 4.6: The 10 dB beamwidths in the E- and H-planes of $Horn1$ and $Horn3$. Both horns are fed with either the quadraxial or coaxial feed.

slightly different design of the coax-fed QRFH; the data from this work is added to Fig. 4.7(b) for comparison. This design is however employed with $Throat2$ which contains fewer unwanted modes.

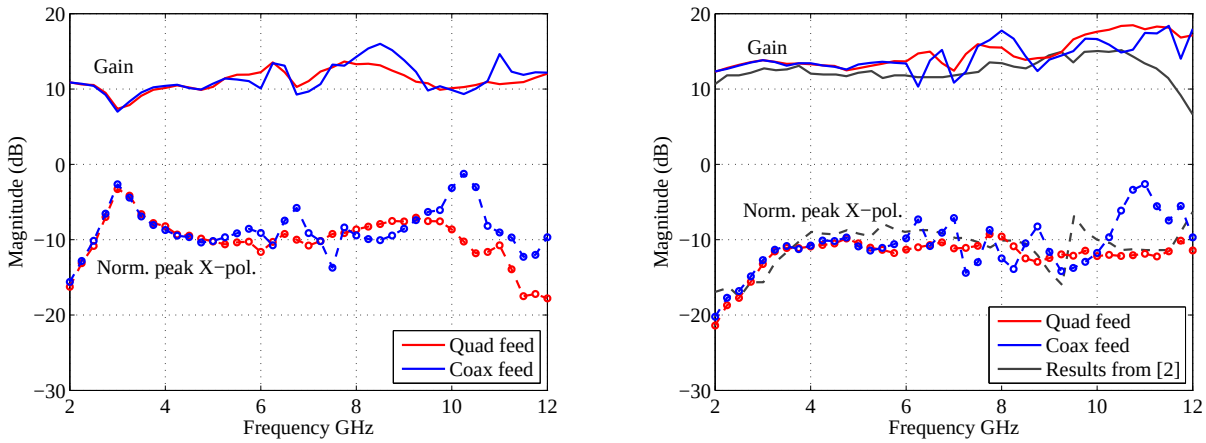

(a) $Horn1$ **(b)** $Horn3$

Figure 4.7: The gain and normalised peak cross-polarisation levels of the different horns.

The phase centre is determined for every frequency sample by finding the optimal position of the horn along the z-axis where the phase efficiency is a maximum. The results are given in Fig. 4.8 with respect to the aperture plane, and as expected, the phase centre does vary with frequency inside the horn. With the quad-fed low-gain horn variation in the position is within 20 mm, while the coaxial-fed horn corresponds to the reported value of 50 mm in [2]. The high-gain horn with the coaxial feed in Fig. 4.8(b) has much larger variation (i.e. $\Delta \approx 180$ mm); however, at the lower frequencies the effect is less pronounced due to the longer wavelength. For example, if the phase centre of this horn is taken as -160 mm (corresponding to 12 GHz) and positioned at the focus of the reflector, the phase centre deviation at 11 GHz is $2.4\lambda_0$ whereas

at 2 GHz it is only $0.8\lambda_0$ – with λ_0 being the wavelength of free-space. Therefore the quadraxial feed improves the phase centre of both horns.

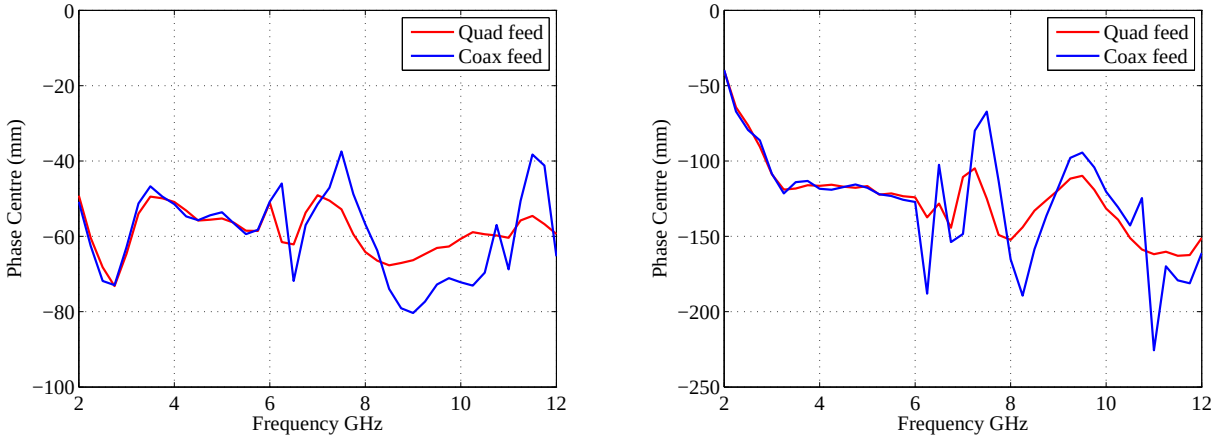

(a) $Horn1$ **(b)** $Horn3$

Figure 4.8: The phase centres of the different horns with respect to their apertures. Each phase centre is determined by moving the aperture of the horn relative to the focus of the reflector, in order to achieve maximum phase efficiency.

It is worth noting that the edge taper that produces an optimal trade-off between η_{sp} and η_{ill} in a reflector system, is also dependent on the specific radiation pattern – in Subsection 2.4.1 the optimal taper for the SKA optics is calculated as 10 dB with the ideal radiation pattern given by equation (2.20). Therefore, patterns obtained with the QRFHs which do not achieve this edge taper, are not inherently sub-optimal and one also needs to consider the overall pattern shapes. Smooth-shaped and constant beam patterns over the frequency range are desirable for radio telescope interferometry. Large areas of the sky are typically imaged with multiple antenna beams which are computationally expensive and requires complex calibration procedures to correct the imperfections of the beam shapes [69, 70].

In Figs. 4.9 and 4.10 the gain patterns of the co-polarised far-fields of $Horn1$ and $Horn3$ are given, respectively. The frequencies are specifically chosen to illustrate the main pattern variations. Firstly, note in graphs (a)-(b) of both Figs. 4.9 and 4.10 how the beamwidth narrows in the H-plane, while the E-plane beamwidth remains fairly constant over the frequency range. According to the calculated aperture modes, not shown here for brevity, there is a lack of power in the higher-order TE modes, compared to the reference distribution in Fig. 4.3.[3] As previously shown, these are required to maintain the beamwidth as frequency increases. The E-plane beamwidth however is sustained by the sufficient higher-order TM modes present in the aperture.

The coaxial feed causes large ripples in the main beam as well as significant sidelobes, as seen from Figs. 4.9(c)-(d). The pattern variation across the frequency range is also worse than with the quadraxial feed, with the poor radiation at 11 GHz directly related to the large excitation of unwanted modes in the throat section (see Fig. 3.20). The non-ideal coaxial transition to

[3]Note that the modal coefficients of the reference pattern are calculated for a smaller aperture; however, similar distributions are found for the aperture sizes of both $Horn1$ and $Horn3$.

the ridged waveguide is also clearly observed in the asymmetry of the E-plane patterns. With $Horn3$ similar effects are found in the far-fields as seen from Fig. 4.10.

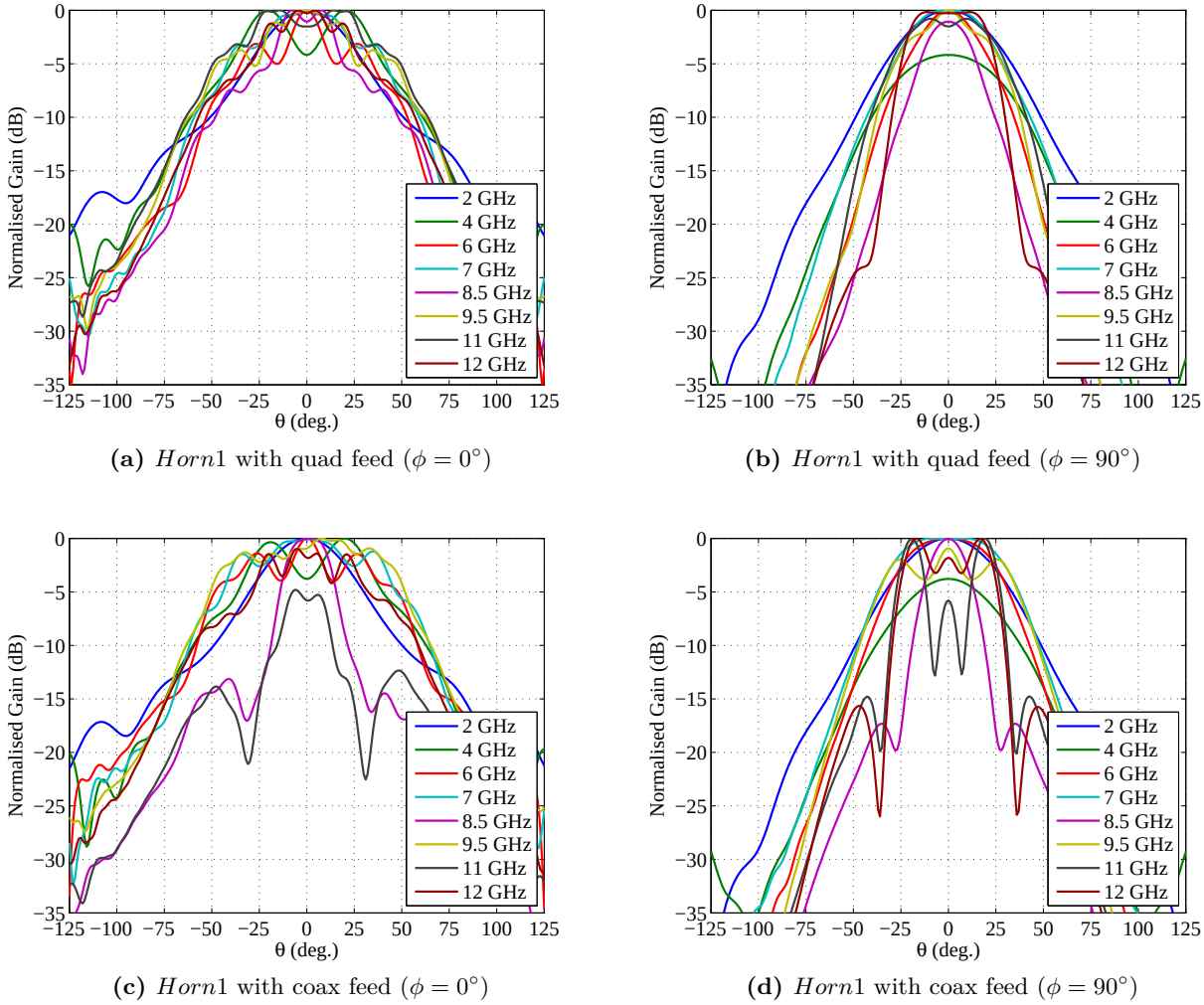

(a) $Horn1$ with quad feed ($\phi = 0°$)

(b) $Horn1$ with quad feed ($\phi = 90°$)

(c) $Horn1$ with coax feed ($\phi = 0°$)

(d) $Horn1$ with coax feed ($\phi = 90°$)

Figure 4.9: The normalised gain patterns of the co-polar far-fields.

In Fig. 4.11 the input reflection coefficients are shown. Overall the flared sections are found to be good matching networks between free-space and their throat sections. Due to the high impedance of the quadraxial line with length $L_{cyl} = 3.5\ mm$, an average input match of $-6.8\ dB$ is achieved, with peaking at $-4\ dB$, for a 150Ω termination. The coaxial feed in both horns, however, achieves an input match better than $-10\ dB$ over most of the bandwidth, while some peaking occurs at the highest frequencies. The strong resonances at about 6.1 GHz and 10.8 GHz correlates directly with the cut-off frequencies of the excited TE_{12} and TE_{13} modes in the throat section; however, this is not present in $Horn1$. Another resonance is found at 7.6 GHz which is exactly at the cut-off frequency of TM_{11} in the throat section. Therefore at this point the wave impedance of TM_{11} is zero and the effect is present in both horns with coaxial feeds. Interestingly enough, at all of these resonant frequencies it is found that sudden phase centre shifts occur, as seen from Fig. 4.8.

Furthermore, the isolation between the coaxial ports, including that of $Throat2$, is found to

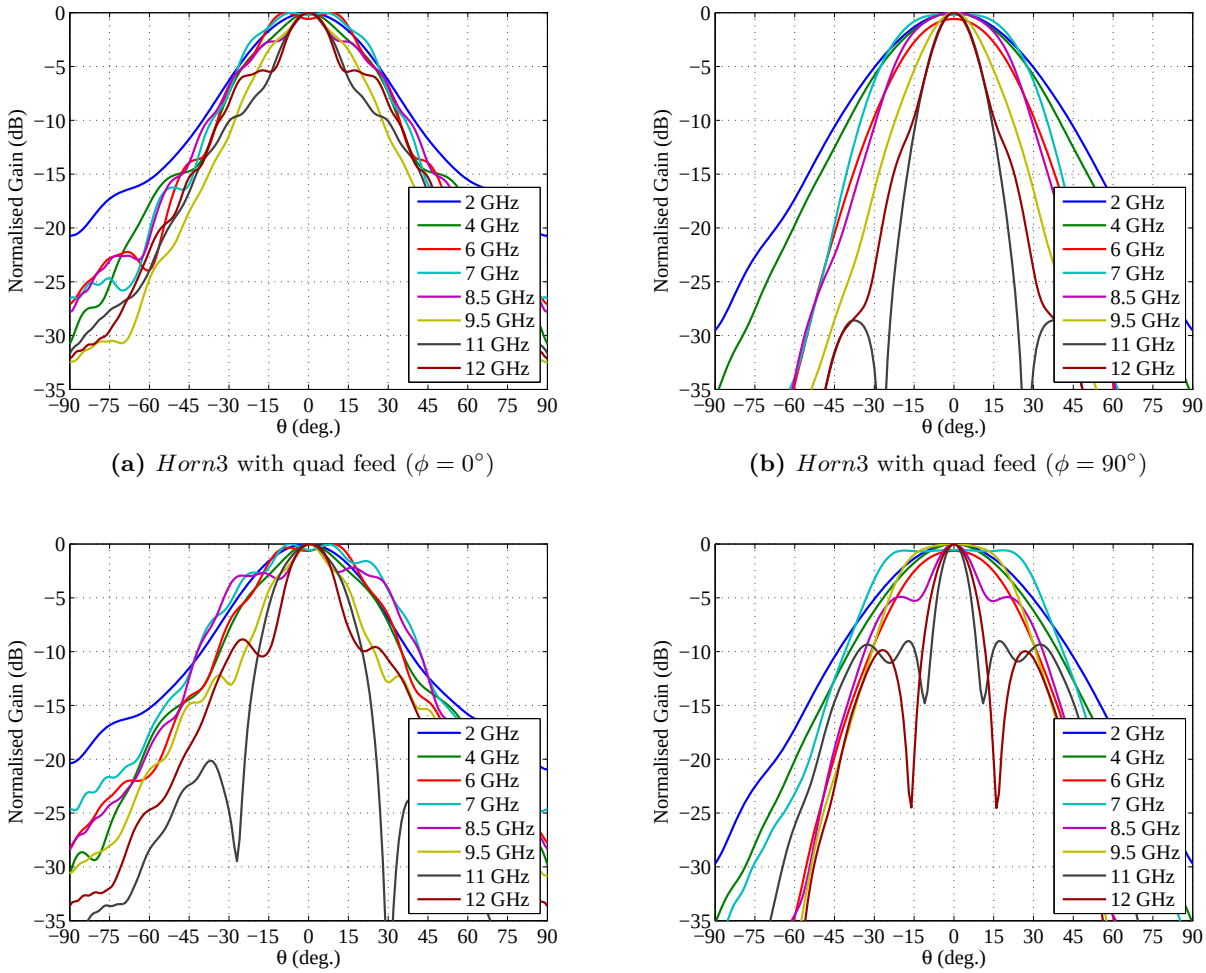

(a) *Horn*3 with quad feed ($\phi = 0°$)

(b) *Horn*3 with quad feed ($\phi = 90°$)

(c) *Horn*3 with coax feed ($\phi = 0°$)

(d) *Horn*3 with coax feed ($\phi = 90°$)

Figure 4.10: The normalised gain patterns of the co-polar far-fields.

be greater than 40 dB. In both practical implementations in [2, 3], the measured isolation is just over 30 dB. The performance of the second port – a coaxial probe with offset towards boresight – are not presented here for brevity. In both *Throat*1 and *Throat*2, the second ports have slightly poorer input matches and cross-polarisation levels at the highest frequencies, although the other far-field results are similar.

In conclusion, the simulated results of the QRFH antenna, excited by the quadraxial feed, shows improvement in the overall shape of the radiation patterns – their symmetry in the azimuthal planes and frequency dependency over the ultra-wide 6:1 bandwidth. The cross-polarisation levels and phase centre variations are also significantly reduced in comparison with the coaxial feed. A relative improvement in the cross-polarisation of as much as 9 dB, in the problematic region of the high frequencies, is obtained.

4.3.4 Higher-order mode excitations

The inter-modal coupling in a QRFH is complex and difficult to model. This is even more so over a wide bandwidth, as modes which add in phase at one frequency do not at another.

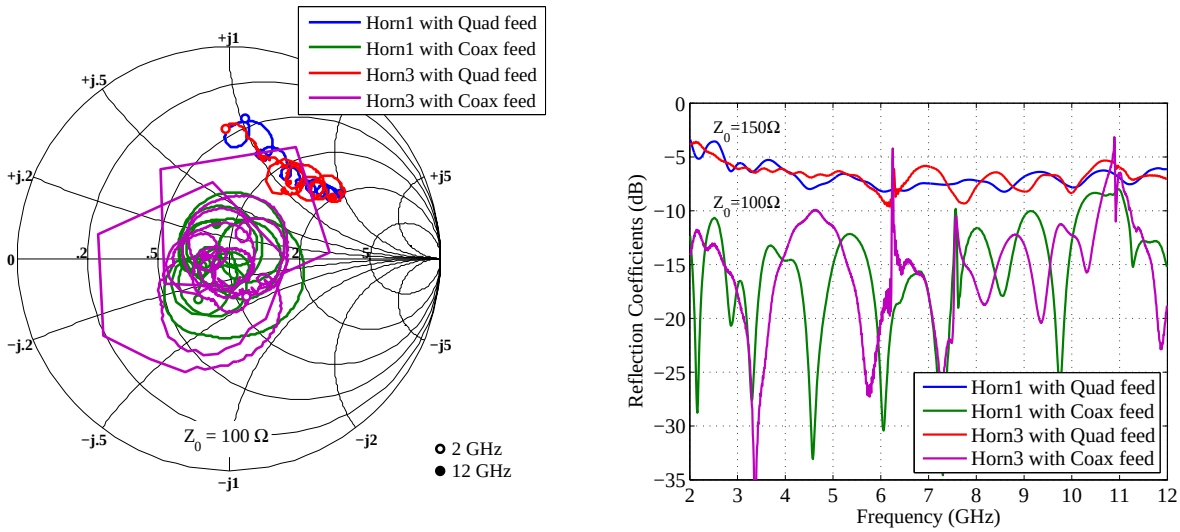

(a) **(b)**

Figure 4.11: The input reflection coefficients of the different horns, where Z_0 is the source impedance.

Therefore, to suppress all the higher-order modes in the throat section does not only allow for better control over the modal content, as illustrated in the design of Chapter 5; but should also minimise unwanted modal interaction.

In order to understand these effects, $Horn1$ is exclusively fed by each of the sub-ordinate modes excited with the coaxial feed in $Throat1$ – i.e. TE_{12}, TM_{11} and TE_{13} – and the resulting patterns are compared. In Fig. 4.12 the far-field patterns are shown for these pure-mode excitations at 11 GHz. The pattern shapes produced by these excitations are similar at other frequencies and thus for brevity not shown here. Note also that these modes are all well matched with $\Gamma_{in} < -20\ dB$ over the entire frequency range. Resemblance in the sidelobes of the patterns of the horn fed by TE_{13} in Fig. 4.12, are found in that of the coax-fed horn at 11 GHz as seen from Figs. 4.9(c) and (d). This is in agreement with the modal content of the throat section given in Fig. 3.20(a), where TE_{13} is almost equal in magnitude to TE_{11}. Furthermore, it is clear that the sidelobes and beam ripples are strongly coupled to the higher mode excitations.

In Fig. 4.13(a) the phases of the far-fields in Fig. 4.12 are given along with that of the TE_{11}-fed horn. As expected the phase fronts of all of these higher-modal excitations differ. It is therefore clear that the phase centres should have less variation over frequency in a horn with a pure-mode excitation.

The cross-polarisation levels are given in Fig. 4.13(b), where the TE_{11}-fed and coax-fed horn results are also included. It is difficult to see from these results exactly why the cross-polarisation of the coaxial feed varies over frequency; however, we know that there are phase differences among these excitations and therefore rapid variations are expected. Even if $Throat2$ is preferred for its better modal performance, the TE_{12} and TM_{11} modes are still excited by the coaxial feed and therefore similar peaks are found.

It is interesting to note that, only TE_{11} is excited with the coaxial feed below 6.1 GHz in the throat section; however, from 4.5 GHz there is a notable difference between the cross-

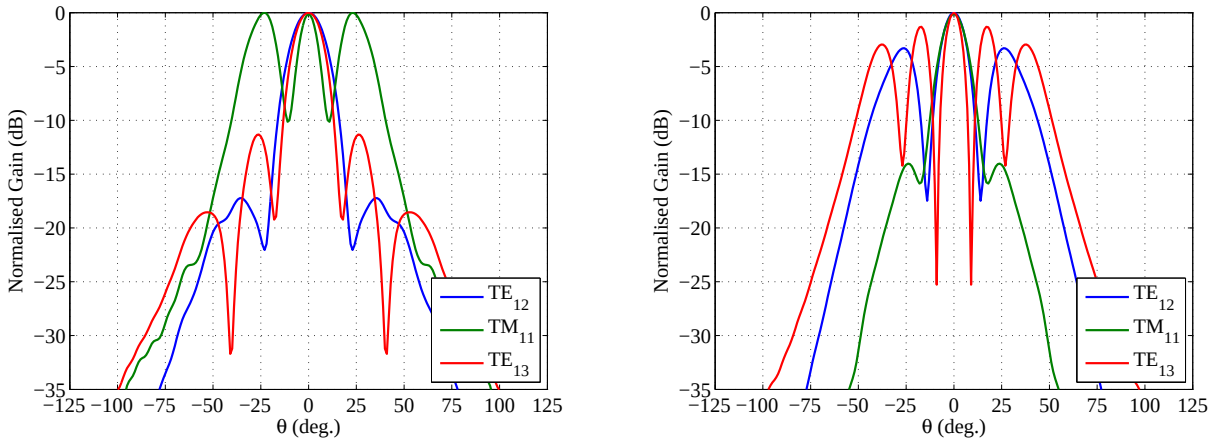

(a) $\phi = 0°$ **(b)** $\phi = 90°$

Figure 4.12: The gain patterns of $Horn1$ excited with different modes at 11 GHz.

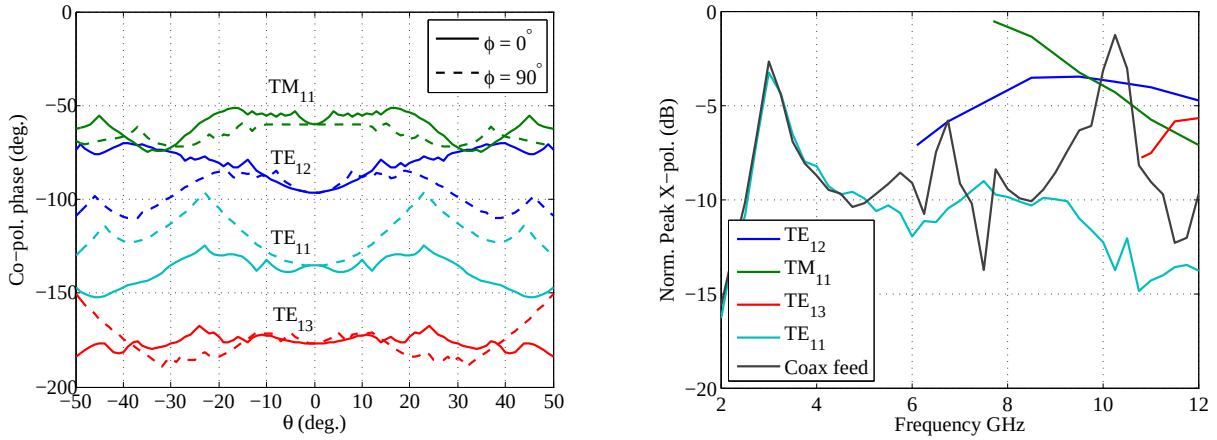

(a) **(b)**

Figure 4.13: The (a) phase and (b) normalised peak cross-polarisation levels of $Horn1$ with different excitations.

polarisation levels produced by the coaxial and TE_{11} feeds. This difference does not exist between the latter and the quadraxial feed. Therefore, it is reasonable to conclude that this effect is due to the back-short of the coaxial feed, which only acts at a single frequency as a complete open-circuit to the coaxial transition.

4.4 Parameter study of flared section

In the next chapter a prototype antenna is designed for the SKA requirements, using a modal approach for the QRFH design. In order to obtain a starting point for the design, a parameter sweep is executed here to evaluate the flared section for a pure TE_{11} mode excitation. The process is implemented in MATLAB [71], where a dimension set is first sent to CST-MWS to run a full-wave simulation, followed by the far-field results being imported into MATLAB, after which the different efficiencies, phase centres, peak cross-polarisation levels and modal coefficients in

the aperture are calculated, as defined in Section 2.3, equation (2.28) and Subsection 4.2.1.

The efficiency equations given in Section 2.3.2, are slightly changed for the effective evaluation of the QRFH. These equations were defined for the ideal case where there are only A_m and C_m coefficients present with the y-polarised far-fields [see equation (2.9)]. With a practical radiator the B_m and D_m components could also be present for the y-polarised excitation (and vice versa); therefore to consider the complete radiated power these need to be included in the $BOR1$ efficiency [72]. Thus equation (2.14) becomes

$$\eta_{BOR1} = \frac{\pi \int_{\theta=0}^{\pi} \left[|A_1(\theta)|^2 + |B_1(\theta)|^2 + |C_1(\theta)|^2 + |D_1(\theta)|^2\right] sin\theta d\theta}{\int_{\phi=0}^{2\pi}\int_{\theta=0}^{\pi} \left[|G_\theta(\theta,\phi)|^2 + |G_\phi(\theta,\phi)|^2\right] sin\theta d\theta d\phi}. \tag{4.19}$$

The spillover efficiency is also amended to include the total power and therefore equation (2.16) is changed to

$$\eta_{sp} = \frac{\int_{\theta=0}^{\theta_e} \left[|A_1(\theta)|^2 + |B_1(\theta)|^2 + |C_1(\theta)|^2 + |D_1(\theta)|^2\right] sin\theta d\theta}{\int_{\theta=0}^{\pi} \left[|A_1(\theta)|^2 + |B_1(\theta)|^2 + |C_1(\theta)|^2 + |D_1(\theta)|^2\right] sin\theta d\theta}. \tag{4.20}$$

In order to complete the factorisation of the feed efficiency defined in (2.13), the denominator of the polarisation efficiency in equation (2.17) is changed to

$$\eta_{pol} = \frac{\int_{\theta=0}^{\theta_e} \left[|CO(\theta)|^2 + \frac{1}{2}|XP(\theta)|^2\right] sin\theta d\theta}{\int_{\theta=0}^{\theta_e} \left[|A_1(\theta)|^2 + |B_1(\theta)|^2 + |C_1(\theta)|^2 + |D_1(\theta)|^2\right] sin\theta d\theta}. \tag{4.21}$$

In order to evaluate the parameter sweep, the specific SKA optics are chosen to have $\theta_e = 49°$, $D_s = 5\ m$ and no sub-reflector extension. The smallest subtended angle is more applicable for QRFH feeds, because in [65] it is shown that the QRFH performance deteriorates significantly for large beamwidth designs. Amongst the three possible sub-reflectors the mid-size is chosen. The closed-form equations of the feed efficiency along with the diffraction approximation for the offset Gregorian system do not include the effects of the physical structure, other than the offset reflectors, and therefore the sub-reflector extension is not considered here.

The dimension space of the parameter sweep is chosen according to results of the optimised horns in Subsection 4.3.2. The throat dimensions of the horn are fixed to $a_{th} = 34\ mm$, $g = 2.5\ mm$, $t = 3\ mm$ and $w = 1$, with the motivation of these given in the design of the next chapter. In order to reduce spillover, the aperture size of the horn is chosen to ensure that the beamwidth at f_{lo} is equal to the full-subtended angle of 98°. As we are interested only in $m = 1$ modes in the aperture, the TE modes alone contribute to the H-plane pattern. In order to avoid unnecessary phase errors in the aperture, it is better to limit the amount of aperture modes at the lowest frequencies. Therefore, only the TE_{11} mode is used to determine the aperture size that would ensure the required beamwidth in the H-plane. This is calculated from equation (4.7) as $a_{ap} = 105\ mm$. In the E-plane the beamwidth is too narrow with only TE_{11} present and

therefore TM_{11} is also required. This results in the modal coefficients $a_{11} = 0.79$ and $b_{11} = 0.21$ at 2 GHz.

Three dimensions remain for the parameter sweep, namely the horn length (L_{rad}), the ridge taper rate (R_{ridge}) and the sidewall taper rate (R_{side}). The horn length is varied between that of the low-gain horns given in Table 4.2, which is chosen as $L_{rad} = [140, 160, 180, 200]$ in millimetres; while the taper rates are also varied around the values of the horns as $R_{ridge} = [0.035, 0.04, 0.045, 0.05]$ and $R_{side} = [0.025, 0.03, 0.035, 0.04]$.

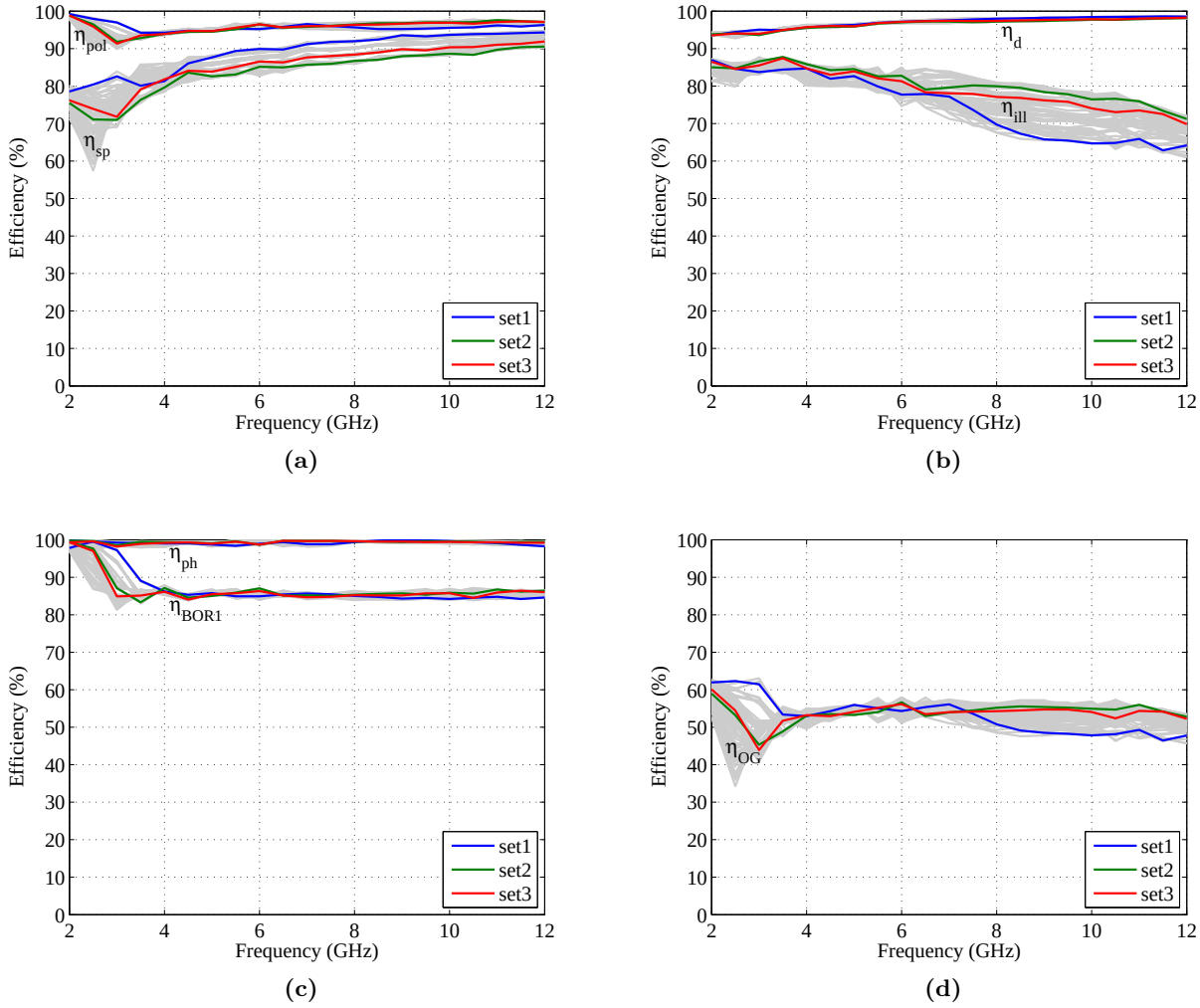

Figure 4.14: The different efficiencies calculated by the closed-form equations of the 64 flared sections. These are (a) the polarisation and spillover; (b) the diffraction and illumination; (c) the phase and $BOR1$; (d) the complete aperture of the offset Gregorian system. Here 3 sets are highlighted with the remaining results depicted by the grey lines.

This leads to a total of 64 different sets of horns, where 3 specific sets are highlighted in the efficiency results presented in Fig. 4.14. The collection of the remaining 61 sets are indicated by the grey regions on the graphs. The dimensions of the highlighted sets are given in Table 4.4. The first set has the highest overall spillover efficiency (η_{sp}) as shown in Fig. 4.14(a); however, due to the typical beamwidth narrowing, $set1$ consequently falls into the range of the lowest illumination efficiencies (η_{ill}) as seen from Fig. 4.14(b). The opposite effect is true for

the second set where η_{ill} is highest. Consequently the result is that the aperture efficiency of the offset Gregorian system (η_{OG}) varies over the bandwidth for these two sets. Note that the highest η_{OG} value of the parameter sweep is found at the lowest frequencies, where it is also the easiest to control the modal content due to the few modes present in the horn. Therefore, a compromise between the first two sets are found in $set3$, where the spillover is slightly better than $set2$ though η_{OG} is not lowered at the highest frequencies. The sudden drop at 3 GHz can be improved in order to obtain good overall performance – as illustrated through the taper synthesis technique proposed in the next chapter.

Table 4.4: Three different sets of dimensions from the parameter sweep of the horn.

	L_{rad}	R_{ridge}	R_{side}
$set1$ – high η_{sp}	160 mm	0.035	0.04
$set2$ – high η_{ill}	200 mm	0.05	0.04
$set3$ – potential	160 mm	0.045	0.035

The remaining efficiency factors – polarisation (η_{pol}), diffraction (η_d), phase (η_{ph}) and $BOR1$ (η_{BOR1}) – are very similar among the 64 horn sets. The latter is almost constant at 85% over the mid and high frequency ranges, shown in Fig. 4.14(c). As expected the diffraction increases towards the lower frequencies – noted from the diffraction efficiencies in Fig 4.14(b).

Lastly, the gain and normalised peak cross-polarisation levels are given in Fig. 4.15. Deviations are found with both these results at the lowest frequencies. At the mid and higher frequencies the cross-polar levels are around -10 dB. Note that all of the horns in the parameter sweep have $\Gamma_{in} < -14$ dB for the TE_{11} excitation.

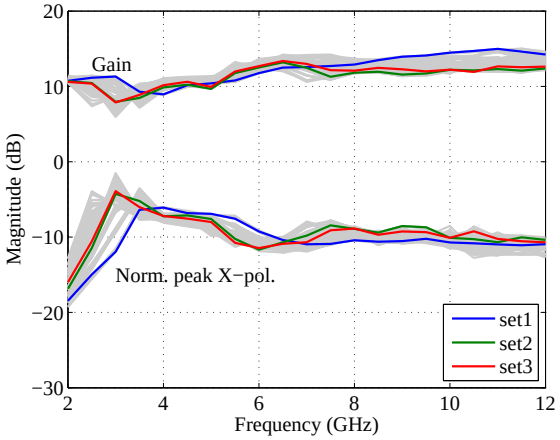

Figure 4.15: The gain and normalised peak cross-polarisation levels of the 64 flared sections. Here 3 sets are highlighted with the remaining results depicted by the grey lines.

4.5 Conclusion

In this chapter it was shown that the quadraxial feed significantly improves the far-field results compared to the coaxial feed. The known radiation issues of the QRFH, as listed in Section 1.1, have been addressed by the quadraxial feed. One main drawback of the quadraxial feed however

is that the input match is poorer than with the conventional feeding. In future work this could possibly be improved by incorporating strategic matching networks with dLNAs.

To maintain the beamwidth at the mid and highest frequencies with the oversized throat sections, which are easier to manufacture, the aperture should in general be larger than that of $Horn2$ (see Table 4.2), where the latter also corresponds to the QRFH design in [2] employing the same small throat. The larger aperture, however, has the effect of strongly exciting the TM_{11} and TE_{31} modes at the lowest frequencies, which reduces the power in the TE_{11} mode and thus results in an increased cross-polarisation and widened beamwidth. In the next chapter these problematic effects are dealt with through the shaping of the ridge profile.

Chapter 5

Prototype Development

5.1 Introduction

The most widely used approach for designing a QRFH antenna is to employ simple analytical functions for the tapering of the ridge and sidewall profiles [65]. A search function is typically used to find an optimal solution for the defining parameters of these tapering profile functions from full-wave electromagnetic simulations [2]. This approach is not only very time consuming, but it also does not necessarily guarantee an optimal geometry for the radiating structure.

Mode-matching is a well established technique that is used to analyse as well as synthesise smooth-wall and corrugated horns [61]. Attempting to apply this approach to the design of ridged waveguide structures is however quite complex, due to a number of factors. Firstly, there is no analytical solution of the modes in a quad-ridged waveguide, though numerical solutions for the ridge-loaded transverse modes have been reported [43]. Secondly, a sufficiently large number of modes need to be solved in order to reduce the truncation error in the modal set of the QRFH. For the typical operational bandwidth of 6:1 this amount becomes very large. Although present day computational capabilities and EM solvers allow for fast solutions of large numbers of modes over wide frequency spectra, each cylindrical mode undergo different changes with the loading of ridges and therefore still need to be assessed for each section with a differing ridge-to-sidewall ratio.

In this chapter a design technique is presented to enhance the radiation properties through the profiling of the ridge taper based on the cut-off frequencies of specific modes. The technique is used to design a prototype antenna for the proposed offset Gregorian system of SKA. Measured results confirm the validity of this approach, where good agreement is found with the simulated results.

5.1.1 General design technique

The proposed design technique could be summarised in the following steps:

(i) Determine the ridge thickness and gap width between opposing ridges in the throat section according to mechanical feasibility, as well as to ensure a specified input impedance.

(ii) Calculate the aperture diameter at the lowest operational frequency in order to allow the

lowest number of propagating modes required to achieve the specified beamwidth – more modes introduces more phase errors.

(iii) Choose the length of the flared section such that the length-to-aperture ratio (i.e. $L_{rad}/2a_{ap}$) ensures good performance for the specified beamwidth – the larger this ratio the narrower the beamwidth. (Refer to the results in Table 4.2 as well as in [3, 68].)

(iv) Use an exponential function for the sidewall taper and determine the opening rate either for a known flared angle or through a coarse parameter sweep. For a wider beamwidth the flared angle is typically also wider and therefore the taper rate is larger [see equation (4.4)].

(v) Synthesise the ridge tapering profile with the cut-off frequencies of modes throughout the structure, to ensure a desired field distribution in the aperture. This is achieved by feeding the flared section, consisting of the dimensions obtained in the previous steps, with the fundamental TE_{11} mode in one polarisation.

(vi) Finally, employ the feeding network to ensure a pure-mode excitation of the horn.

These steps are followed throughout this chapter for the systematic design of a QRFH antenna.

5.1.2 Design strategy

In the parameter sweep of Section 4.4 it was shown that good performance can be achieved with the exponential tapering function, although only over limited parts of the 6:1 bandwidth. The highest aperture efficiency obtained over the largest part of the bandwidth is 55%; however, the trade-off for this is a sudden drop at the lowest frequencies, which in some cases are as low as 35%. Therefore, the tapering of the flared section should be changed to an arbitrary profile that would allow $\eta_{OG} \approx 55\%$ over the entire bandwidth.

To illustrate the proposed technique a prototype is designed that deals with the aforementioned performance limitations. It is designed for the specific offset Gregorian reflector system where $\theta_e = 49^\circ$ and $D_s = 5\ m$ – identified in Section 4.4 as a reasonable choice for the QRFH. Following the general performance capabilities obtained through the parameter sweep of Section 4.4, an average aperture efficiency of 55% is set as the aim, with a minimum value above 50% at any frequency. A spillover efficiency of higher than 75% is set as a goal to minimise the spillover noise and $\Gamma_{in} \leq -15\ dB$ over the bandwidth as input match target.

A far-field pattern is chosen as a reference for the design process. This is obtained by identifying a pattern from the set of flared sections simulated for the parameter sweep in Section 4.4, which produces the highest η_{OG} with good cross-polarisation at a single frequency. The reference pattern is shown in Fig. 5.1 and produces an aperture efficiency of 72% at 3.25 GHz in the OG system. The co-polarisation cut patterns in Fig. 5.1 have an edge taper ranging between -8.7 and $-10.4\ dB$, which corresponds well with the optimal taper value of $-10\ dB$. The peak normalised cross-polarisation is $-17\ dB$.

The next important step in the design process is the determination of the cut-off frequencies of modes applicable to that of the horn. In Fig. 5.2 the frequencies are plotted for a QRWG –

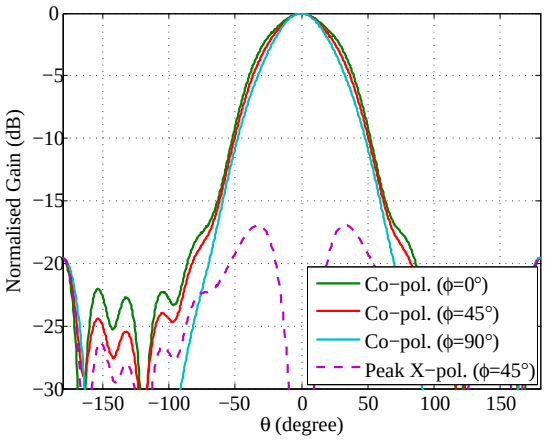

Figure 5.1: The normalised co- and cross-polarisation cuts of the reference far-field pattern.

with dimensions of the throat section in Table 5.1 – for different ridge-to-sidewall ratios. Only the applicable modes for the QRFH are shown in the figure. The chamfering of the ridges are fixed to the position of the smallest gap, where $g = 2.5\ mm$ and the tip width is $w = 1\ mm$. Therefore, when the gap is above 4.5 mm the 45° chamfer on the edges of the ridges disappear.

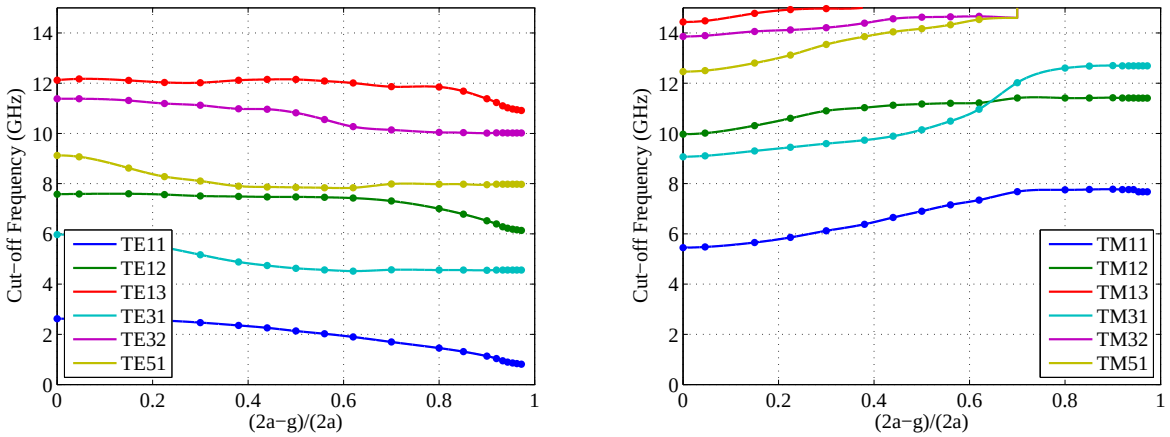

Figure 5.2: The cut-off frequencies of modes in a QRWG with diameter 68 mm and varying ridge-to-sidewall ratio. The ridges has a constant chamfer at the narrow ridge gaps, with reference dimensions $g = 2.5\ mm$, $t = 3\ mm$ and $w = 1\ mm$.

By applying the cut-off frequency data of Fig. 5.2 to the profile of a QRFH, either the sidewall diameter, ridge gap or cut-off frequency of a specific mode can be calculated at any point in the longitudinal direction, given the other two values. Due to the fixed diameter of the cylinder used in Fig. 5.2, the assumption is therefore that the ridge thickness becomes larger with an increasing sidewall diameter. This is not the case with a normal QRFH; however, due to the weaker loading of the ridges at larger diameters, this is found to be an acceptable approximation.

5.1.3 Determination of basic geometry

The ridge geometry in the throat section as depicted in Fig. 5.3(a), must be manufacturable, and ensure a high impedance that are preferable for the quadraxial transition. These two aspects are complementary in that a larger ridge gap allows for a higher impedance. The increased gap however decreases the bandwidth between the fundamental and higher-order modes. A ridge thickness $t = 3\ mm$ is used due to the larger suppression of the TE_{12} and TE_{13} modes compared to the instance where $t = 2\ mm$, as illustrated in Fig. 3.19(b). The cylinder radius is $a_{th} = 34\ mm$ to ensure a low f_c^{TE11} with a larger ridge gap. The gap is $g = 2.5\ mm$ with a tip width $w = 1\ mm$, and produces $R_{eq} = 100\ \Omega$ and a cut-off frequency close to that in the aperture resulting in $f_c^{TE11} = 0.824\ GHz$.

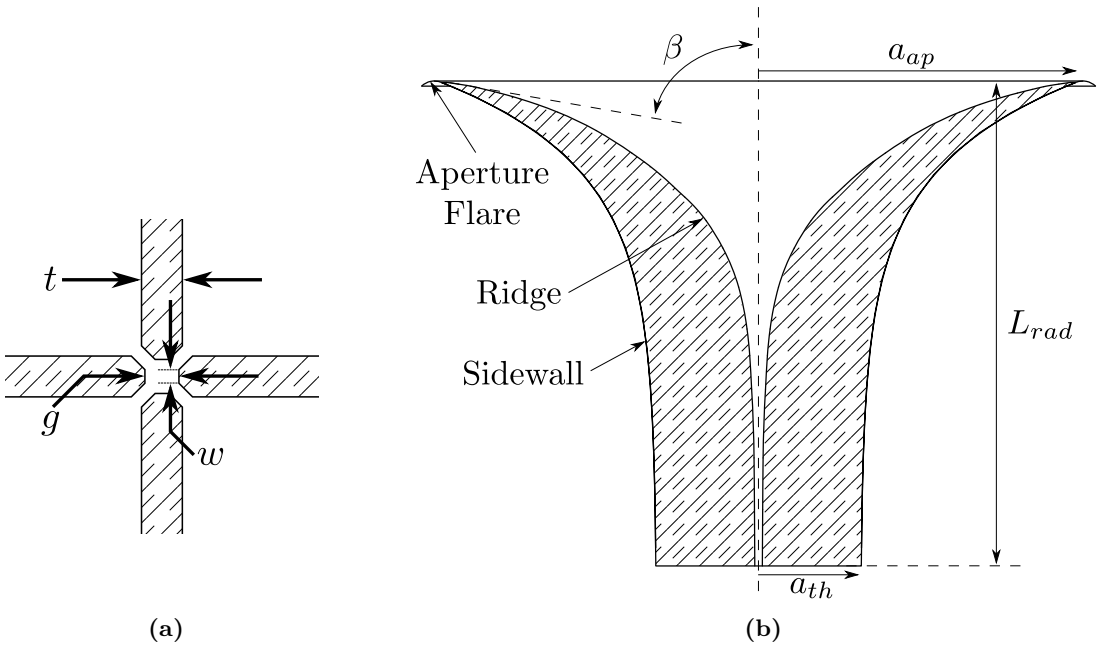

Figure 5.3: Cross-section views of (a) ridges in throat and (b) flared section of QRFH.

Table 5.1: Dimension values of the initial flared section.

Parameter	Value	Parameter	Value
a_{th}	34 mm	a_{ap}	105 mm
g	2.5 mm	L_{rad}	160 mm
t	3 mm	R_{side}	0.035
w	1 mm		

The geometry of the flared section is illustrated in Fig. 5.3(b) and the dimensions are adopted from $set3$ in the parameter sweep of Section 4.4, where $a_{ap} = 105\ mm$, $L_{rad} = 160\ mm$ and $R_{side} = 0.035$. This set of dimensions is chosen in order to obtain maximum aperture efficiency over the entire bandwidth. As shown, the exponential ridge taper rate $R_{ridge} = 0.045$ produces good performance except at 3 GHz where there is a sudden drop. Because the degradation is at the lowest frequencies, where only a small number of modes are above cut-off, the performance becomes easier to control through the tapering of the ridges. The sidewall tapering is however

still realised by the exponential function, as this is a good reference profile for the ridge-to-sidewall ratio.

Furthermore, the aperture size is calculated to obtain a beamwidth of 98° at 2 GHz with only the TE_{11} and TM_{11} modes present in the aperture. The aperture flare part indicated in Fig. 5.3(b) is implemented to ensure a smooth transition to free-space by minimising diffraction of the aperture edge. This aperture-matching technique is described in [73] and it is found in this work that a radius of 6 mm is sufficiently large to ensure a smooth main beam.

The dimensions of the flared section are summarised in Table 5.1 and are used throughout the design process of this chapter.

5.2 Synthesis of ridge tapering profile

The preceding design strategy is applied in this section to shape the ridge profile according to the modal requirements [8]. The final profile is accomplished in three steps and the consecutive solutions are referred to as $Horn1$ through $Horn3$ – each horn excited by the TE_{11} mode alone.

5.2.1 Horn1: constant TE_{11} cut-off

The cut-off frequency of TE_{11} is 0.824 GHz in the throat section while it is 0.837 GHz in the aperture. In the previous section the specific dimensions are chosen for several reasons, amongst these are the fact that similar cut-off frequencies of the fundamental mode are obtained in the throat and aperture. In order to have a smooth transition from the throat to the aperture throughout the flared section, a linear profile for f_c^{TE11} in the longitudinal direction from 0.824 to 0.837 GHz is used, as illustrated in Fig. 5.4(a).

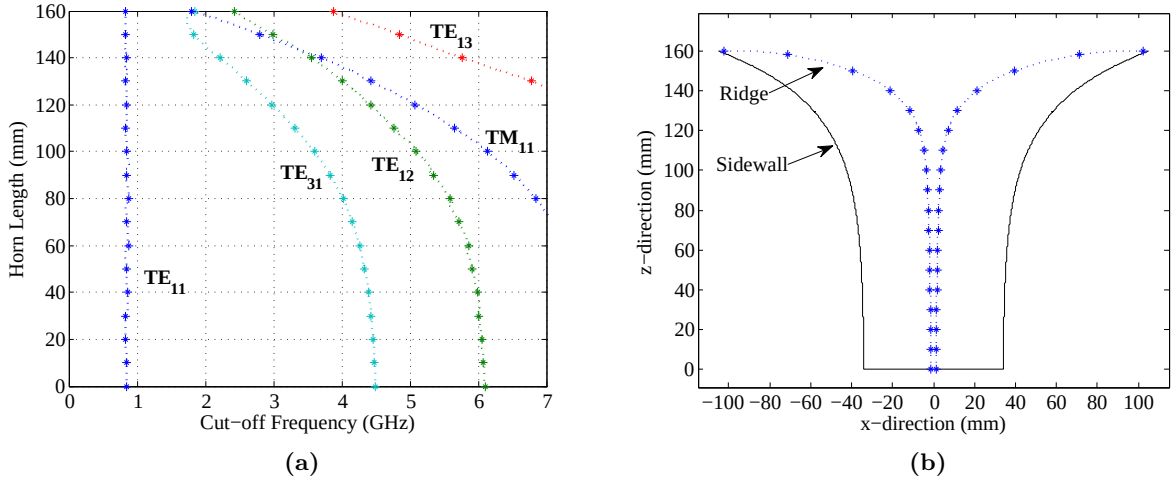

Figure 5.4: The cut-off frequencies in (a) of the significant modes in $Horn1$ with taper profiles given in (b).

Using the frequency profile in Fig. 5.4(a) along with the profile of the sidewall, as proposed in the previous section, the ridge gap is calculated from Fig. 5.2 throughout the horn. This synthesised taper profile is shown in Fig. 5.4(b) and to some extent is similar to the exponential

function. Note how all the other cut-off frequencies in Fig. 5.4(a) are monotonically decreasing towards the aperture. This is desirable in the horn as it eliminates the possibility of a mode excited at one point and becoming evanescent further along the waveguide – referred to as a trapped-mode.

Following the results of the flared sections presented in Chapter 4 – where most achieved $\Gamma_{in} \leq -15\ dB$ – it is evident that this type of structure is inherently well matched between the TE_{11} mode in the throat section and free-space. Because TE_{11} is dominant at the lowest frequencies where mismatch easily occurs, it is expected that the proposed ridge profile in Fig. 5.4(b), where the f_c^{TE11} value is almost constant and much lower than $f_{lo} = 2\ GHz$, would ensure minimum reflections throughout the horn.[1] This is confirmed with the results in Fig. 5.5(a) where an input reflection below $-20\ dB$ is achieved over the entire bandwidth.

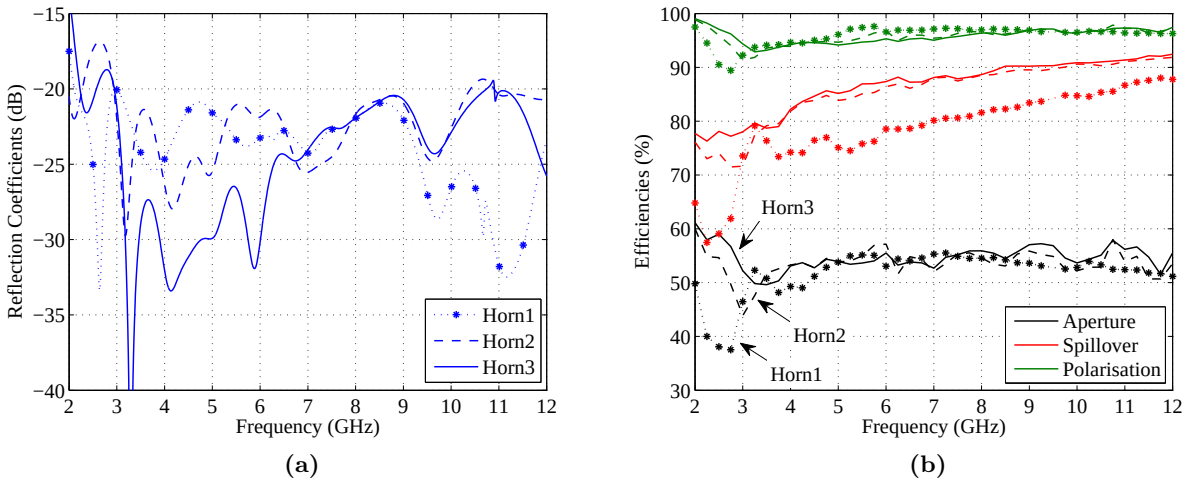

Figure 5.5: The (a) input reflection coefficients and the (b) sub-efficiencies of the three horn designs.

The aperture (η_{OG}), spillover (η_{sp}) and polarisation (η_{pol}) efficiencies are calculated for this horn in the OG system and plotted in Fig. 5.5(b). It is clear that a good performance is achieved above 3 GHz; however, around 2.5 GHz the aperture efficiency is below 40% and does not meet the required 50% specification. The poor performance in this region is dominated by the spillover efficiency as seen from Fig. 5.5(b). In order to gain more insight into this effect, the modal distributions in the aperture are calculated from the far-fields. The first few significant coefficients of the TE and TM modes are respectively plotted in Figs. 5.6(a) and (b), along with the desired distribution of the reference pattern as indicated by the circles. The modal distributions agree well at the highest frequencies; however, at the low frequencies deviations of up to 31% are obtained. The most notable deviation is the significant drop in the TE_{11} coefficient value, depicted by the blue line in Fig. 5.6(a). This is mainly due to the unwanted larger magnitudes of the coefficients of TE_{31}, TM_{11} and TM_{31}. The magnitude of the TM_{11} coefficient peaks particularly high at 2.5 GHz and this amount should rather be contained in the TE_{11} mode. Thus, given the specific electrical size of the aperture, this causes a sudden

[1]Note that for constant f_c^{TE11} the wave impedance is also constant, and therefore the only reflections that might occur in this particular case are due to the coupling into higher-order modes. However, according to Fig. 5.4(a) there can not exist any propagating modes except TE_{11} inside the horn at f_{lo}.

increase in the beamwidth as well as the cross-polarisation level – see example in Subsection 4.2.3. These unwanted effects are clearly observed by the respective drops in spillover and polarisation efficiencies in Fig. 5.5(b).

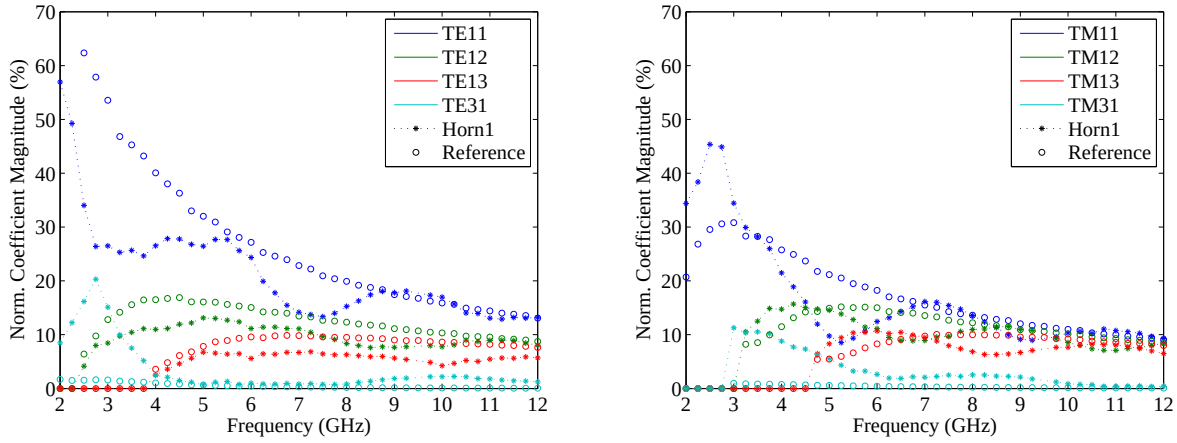

Figure 5.6: The aperture mode coefficients of $Horn1$ and the reference pattern.

5.2.2 Horn2: suppress TM_{11}

In order to improve η_{OG} of $Horn1$ it is necessary to suppress the TM_{11} mode at 2.5 GHz. It is noted from Fig. 5.4(a) that this mode can only propagate very close to the aperture at 2.5 GHz. Upon consideration of the ridge profile in Fig. 5.4(b) it is clear that this horn has a very wide flare angle, i.e. $\beta \approx 90°$. This is typically in favour of supporting transverse magnetic modes – considering the boundary conditions on the transverse E-fields – and therefore β should be reduced in order to suppress the TM_{11} mode.

A taper that achieves this, yet with marginally small deviation in the f_c^{TE11} profile, is that of the $R = 0.045$ exponential function. The new cut-off frequencies are calculated and given in Fig. 5.7(a). In Fig. 5.7(b) the corresponding ridge taper of $Horn2$ is illustrated, where β is reduced from 88.5° to 78.2°. For this profile f_c^{TE11} increases to 1.21 GHz at $z = 125$ mm and therefore due to the change in the wave impedance at the lowest frequencies, it is expected that more reflections would occur, causing a poorer input match. This is observed from the simulation results plotted in Fig. 5.5(a) with the dashed line, where Γ_{in} has a peak of -17 dB at 2.7 GHz.

The modal coefficients of the aperture fields, corresponding to the far-fields of $Horn2$, are calculated and given in Fig. 5.7(c) and (d). It is seen here that the TM_{11} coefficients at 2 GHz and 2.5 GHz are respectively suppressed by 7% and 13%, compared to that of $Horn1$. As expected the result is a narrower beamwidth and lower cross-polarisation, which leads to a higher aperture efficiency as seen from Fig. 5.5(b). Note that the spillover efficiencies are actually improved over the entire bandwidth. At the mid frequencies this could be accounted for by the improvement of the TE_{11} coefficient, while at the highest frequencies it is more difficult to explain directly from the modal content. The reason why the radiation at the higher

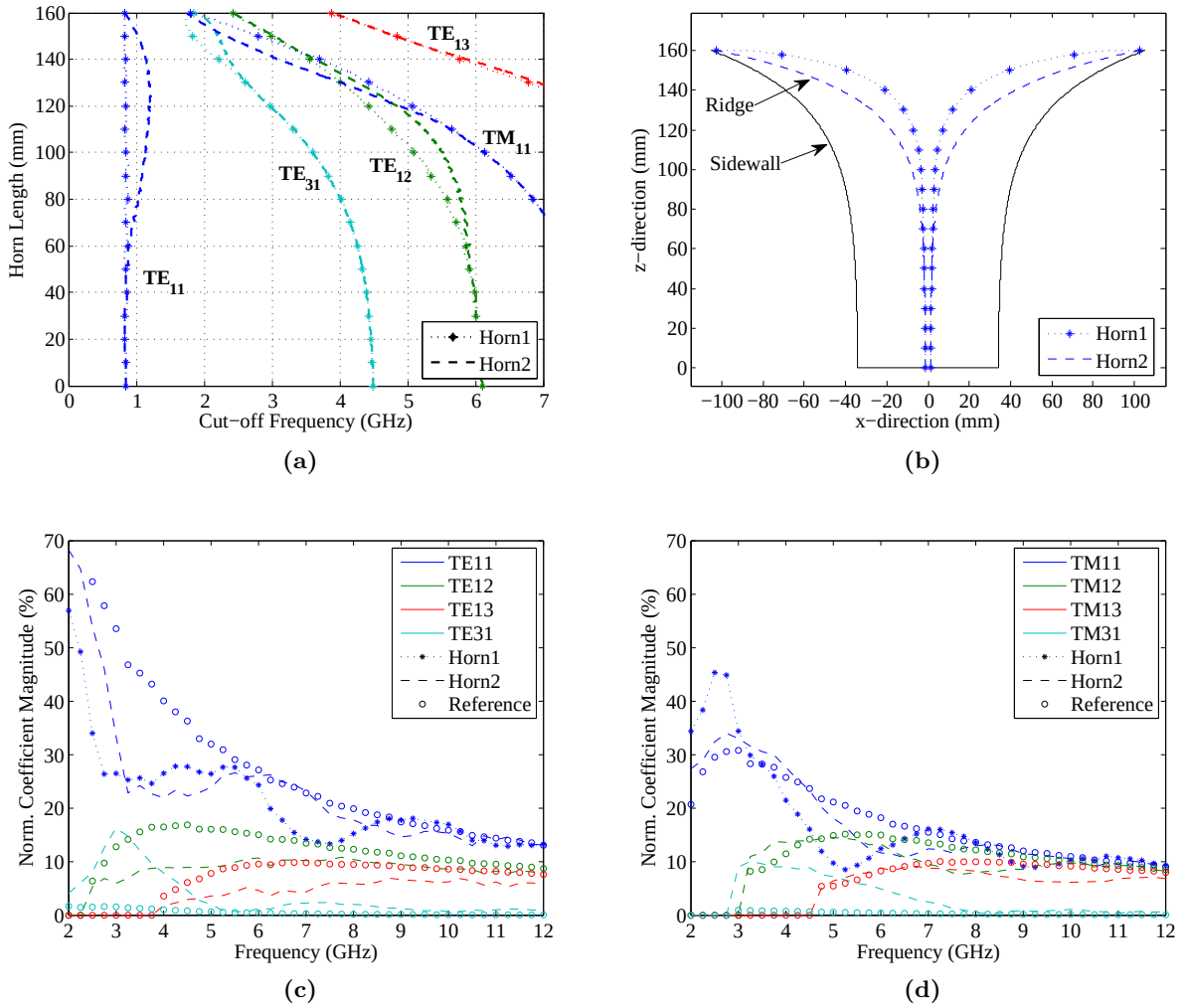

Figure 5.7: The cut-off frequencies in (a) of the significant modes in the horns with taper profiles given in (b). The corresponding aperture modal coefficients of the horns in (c) and (d).

frequencies is not influenced drastically by the change in the flare angle, is due to the significant modes being far above cut-off close to the aperture as seen from Fig. 5.7(a).

Thus the relative improvement of η_{OG} at 2.5 GHz is 17% and the overall increase in the lowest value is 6.4%. Nevertheless, at 3 GHz the aperture efficiency is still lower than 50%. This is directly related to the strong peak in the TE_{31} coefficient as seen in Fig. 5.7(c).

5.2.3 Horn3: suppress TE_{31}

The TE_{31} mode is completely unwanted in the aperture according to the reference modal distributions. This mode has a similar effect at 3 GHz in the far-field performance of $Horn2$, as TM_{11} has at 2.5 GHz in $Horn1$.

In Fig. 5.7(a) it is seen that TE_{31} can propagate at 3 GHz in $Horn2$ only from the location $z = 120$ mm towards the aperture. By increasing f_c^{TE31}, the wave impedance of the mode also increases and in doing so alters its propagation. This is done in the region $z = 120 - 140$ mm and the synthesised locus of f_c^{TE31} is shown in Fig. 5.8(a). Note that the specific region is

chosen not only to increase cut-off near 3 GHz, but it is also limited to the section where the impact of a change in the ridge-to-sidewall ratio is minimum. This is seen in Fig. 5.2(a) for the ridge-to-sidewall ratio between 0.39 and 0.65, where there is almost no change in the cut-off frequencies of TE_{12}, TE_{13} and TE_{51}. In Fig. 5.9(a) it is clear that the cut-off of TE_{12} and TE_{13} is indeed not influenced, while that of TM_{11} is slightly decreased.

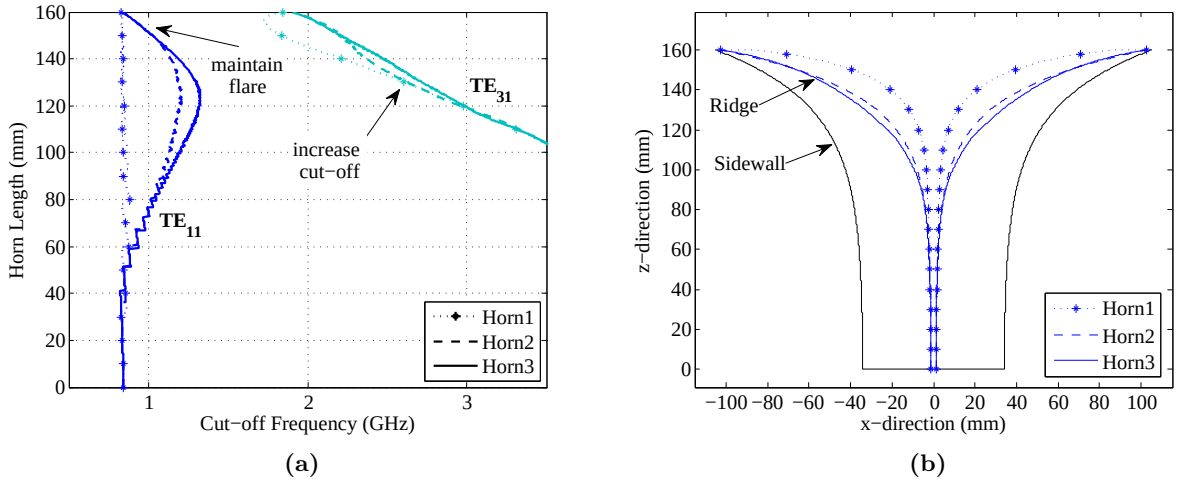

Figure 5.8: The cut-off frequencies in (a) of modes in the horns with taper profiles given in (b).

With these changes in the f_c^{TE31} locus, the resulting f_c^{TE11} is additionally altered to ensure a smooth cut-off profile while maintaining the same flared angle at the aperture as indicated in Fig. 5.8(a). Therefore, with the latter cut-off locus, the the ridge tapering profile of $Horn3$ is calculated and shown in Fig. 5.8(b), with the geometry points given in Appendix A. The geometrical change is seemingly quite small, compared to $Horn2$, though the improvement is substantial when considering the efficiencies of $Horn3$ in Fig. 5.5(b). As expected the spillover and polarisation are both improved at 3 GHz due to the 3.8% decrease of the TE_{31} coefficient in the aperture, as seen from Fig. 5.9(b). The result is an aperture efficiency of larger than 50% over the entire band, with an average value of 55%. The cross-polarisation is still poor at the lower frequencies due to the unwanted TE_{31} and TM_{31} modes; however, the sufficient suppression of these modes might only be possible by additionally altering the sidewall taper. This will most likely be at the expense of degradation at other frequencies due to the wide operational bandwidth and the complex interaction between modes.

Nevertheless, the $\eta_{OG} \geq 50\%$ specification is achieved with this synthesised ridge taper. All the sub-efficiencies are plotted in Fig. 5.10(a), with the physical optics simulation in GRASP confirming the approximated efficiency results. The input match of the final horn design is plotted in Fig. 5.10(b) and it is noted that this is poorer at the lowest frequencies compared with $Horn1$, due to f_c^{TE11} approaching f_{lo} in the region $z \approx 120\ mm$.

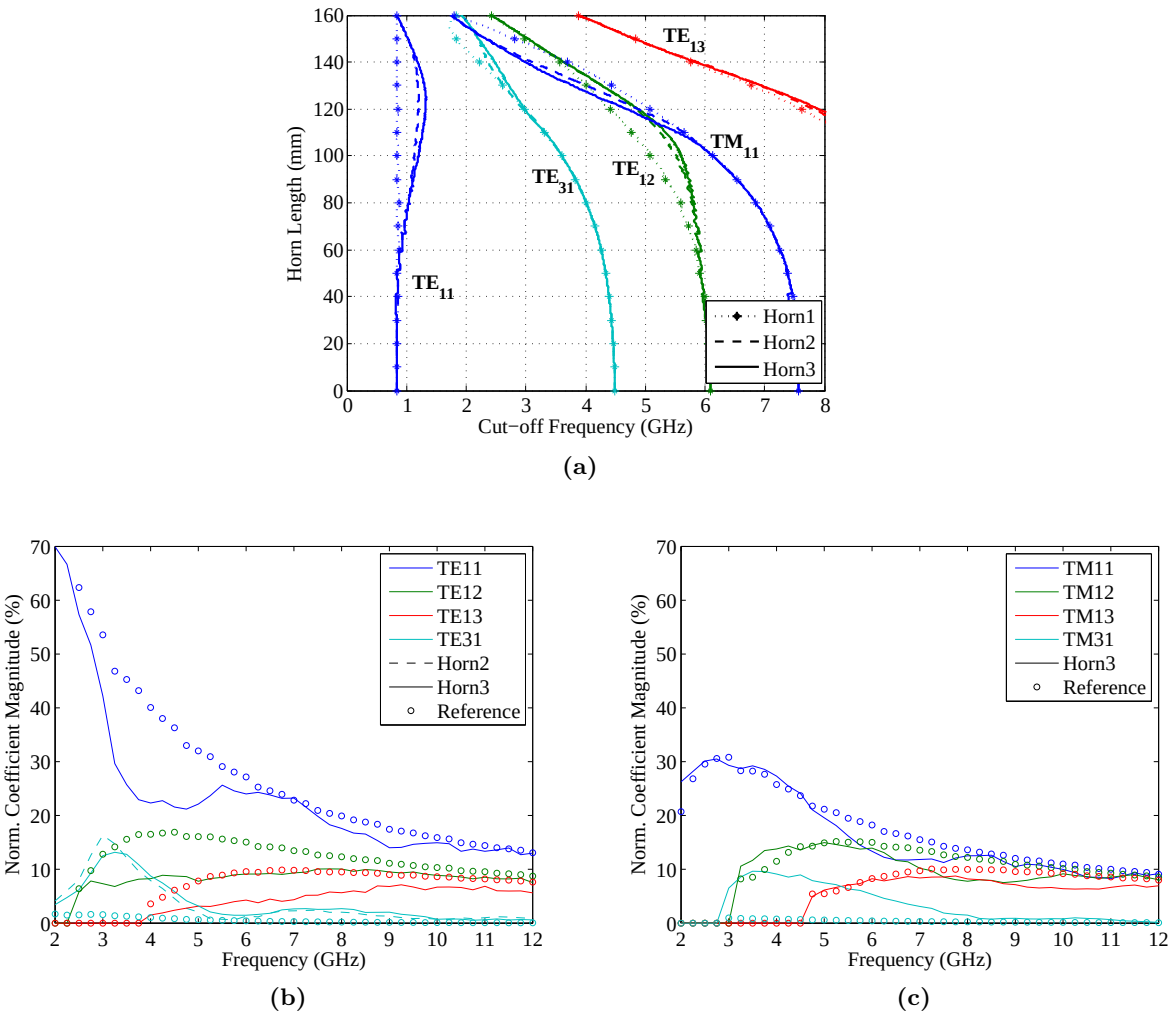

Figure 5.9: The cut-off frequencies in (a) of the significant modes in the horns with taper profiles given in Fig. 5.8(b). The corresponding aperture modal coefficients of the horns in (b) and (c).

5.3 Implementation of quadraxial feed

In the previous section a horn is synthesised that requires a pure TE_{11} mode excitation. In this section the quadraxial feed introduced in Chapter 3 is designed to ensure the required performance of this horn. The aspects which are of importance here, are the modal purity of the throat section and the input match of the quadraxial feed.

As a point of departure the basic quadraxial feed network developed in Section 3.3 is implemented in the synthesised horn. This feeding configuration (see Fig. 3.4) will be referred to as $Feed1$. Here the cylinder through the back wall has radius $a_{cyl} = 11.4\,mm$ and length $L_{cyl} = 3.5\,mm$. Each of the four pins feeding through it has a radius $a_{pin} = 1\,mm$ and is located on a radius $a_{sep} = 3\,mm$ from the centre of the cylinder, as calculated with equation (3.5). The sub-efficiencies calculated with the complete QRFH configuration – consisting of the quadraxial feed and $Horn3$ given in Subsection 5.2.3 – is shown in Fig. 5.11(a). It is clear that above 6 GHz, where the first higher-order mode in the throat section start to propagate, the efficiencies deteriorate compared to that of the purely TE_{11} fed horn in Fig. 5.10(a).

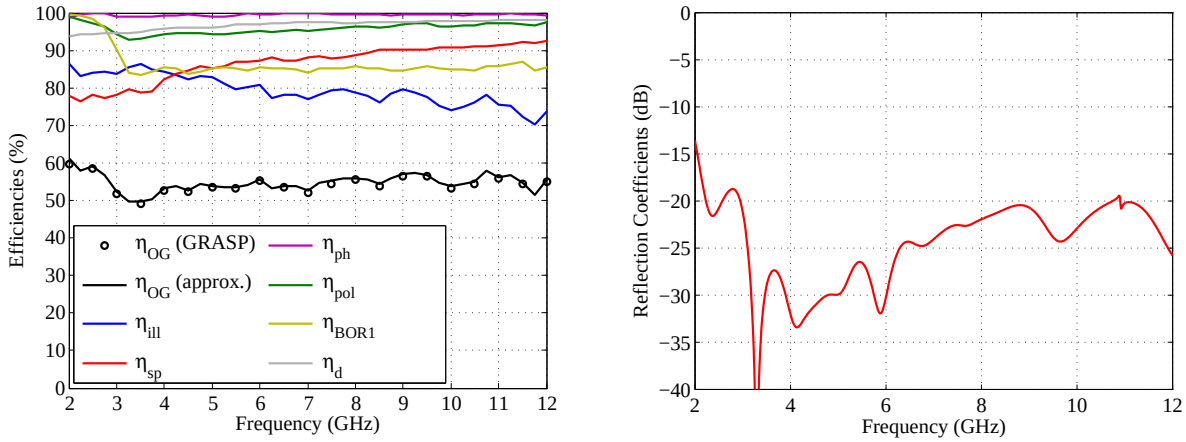

(a) **(b)**

Figure 5.10: The simulated results of $Horn3$. (a) The calculated sub-efficiencies of the illumination (η_{ill}), spillover (η_{sp}), phase (η_{ph}), polarisation (η_{pol}), $BOR1$ components (η_{BOR1}) and sub-reflector diffraction (η_d); which forms the approximated aperture efficiency of the OG system [$\eta_{OG}(approx.)$], with the confirmed results from the GRASP simulation [$\eta_{OG}(GRASP)$]. (b) The input reflection coefficient of the TE_{11} mode excitation.

The simulated S-parameters of the throat section, obtained with a similar CST-MWS setup as described in Subsection 3.3.1, are shown in Fig. 5.11(b). Clearly TE_{12} is the only unwanted mode that propagates between 6 and 7 GHz and therefore is the primary cause for the sudden drop of η_{ill} in Fig. 5.11(a). At the highest frequencies it is a combination of higher-order modes that degrades the performance.

5.3.1 Improvement of modal purity

In order to mitigate these unwanted mode excitations, the sidewall radius is reduced in two intermediate steps as shown in Fig. 5.12. The purpose of these steps are to ensure a gradual transition from the quadraxial line to the throat of the horn. The first section is implemented such that amongst the significant modes, only TE_{11} is above cut-off – with the exception of TE_{31}. The cut-off frequency of this mode cannot be increased above 12 GHz without violating the condition $f_c^{TE11} < f_{lo}$. The second higher-mode is chosen to have $f_c^{TE12} = 12.2\ GHz$ and requires a sidewall radius $a_{rim1} = 18\ mm$. The resulting cut-off frequencies are given in Table 5.2.

Table 5.2: Cut-off frequencies of the significant modes in each section of the throat with radii as indicated. The ridge dimensions are constant with $g = 2.5$, $t = 3$ and $w = 1\ mm$.

	$a_{rim1} = 18$	$a_{rim2} = 22$	$a_{th} = 34$
TE_{11}	1.74	1.36	0.82
TE_{12}	12.2	9.7	6.1
TE_{13}	21.4	17.2	10.8
TM_{11}	15.3	12.2	7.7
TE_{31}	8.9	7.1	4.5

In the second section the sidewall radius is chosen as $a_{rim2} = 22\ mm$ to ensure that the

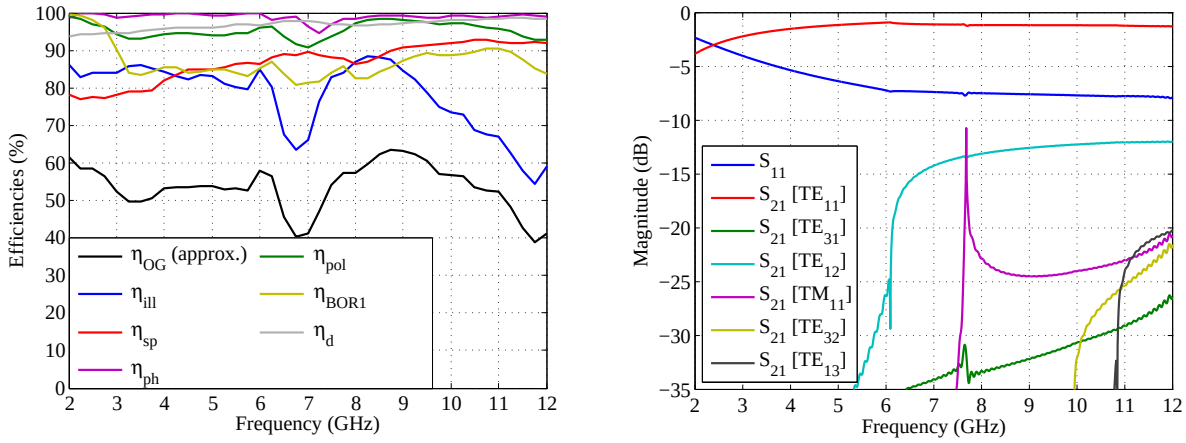

Figure 5.11: The results of $Feed1$. (a) All the approximated efficiencies of the horn in the OG system. (b) The S-parameters of the significant modes excited in the throat section by the quadraxial feed.

third higher-mode is evanescent, i.e. $f_c^{TM11} = 12.2\ GHz$. This section is empirically found to yield a more gradual transition between the first stepped section and the throat section, where $a_{th} = 34\ mm$. Finally, the lengths of the waveguide sections are $L_{rim1} = 10\ mm$, $L_{rim2} = 5\ mm$ and $L_{ext} = 3\ mm$.

The results of this QRFH configuration are shown in Fig. 5.13. It is clear that the introduction of the stepped sections does improve the modal purity and consequently also the far-field performance. The aperture efficiency at 6.75 GHz in Fig. 5.12(a) is increased from 40% to 46% in Fig. 5.13(a). The transfer coefficient of TE_{12} at this frequency is suppressed by 4.3 dB, as seen in Fig. 5.13(b). At the highest frequency η_{OG} is improved with 8% while $|S_{21}[TE_{13}]|$ is suppressed with 8 dB.

5.3.2 Quadraxial feed matching

In Fig. 5.14 the input reflection coefficient is shown for the horn with $Feed2$. Due to the high impedance quadraxial line (i.e. 186 Ω) large mismatching occurs. Practically the four pins must feed some distance through the back lid of the horn, and therefore the mismatch with this feed is unavoidable. The first stepped section with sidewall radius $a_{rim1} = 18\ mm$ causes the wave impedance of TE_{11} to increase drastically at the lowest frequencies which results in the poor Γ_{in} near 2 GHz.

Therefore, to improve this match the characteristic impedance of the quadraxial line need to be lowered either by making the pins thicker, reducing the diameter of the cylinder or inserting a dielectric material in it. The pin thickness are limited by the ridge thickness which is 3 mm and cannot be changed due to the horn design. With a reduced cylinder diameter the shunt inductance in the equivalent circuit (see Fig. 3.5) would also reduce and cause a greater mismatch at the lower frequencies. The only practical solution is therefore to insert a dielectric material. Although this would essentially increase the line length, the effect would be much less severe with a sufficiently lower impedance.

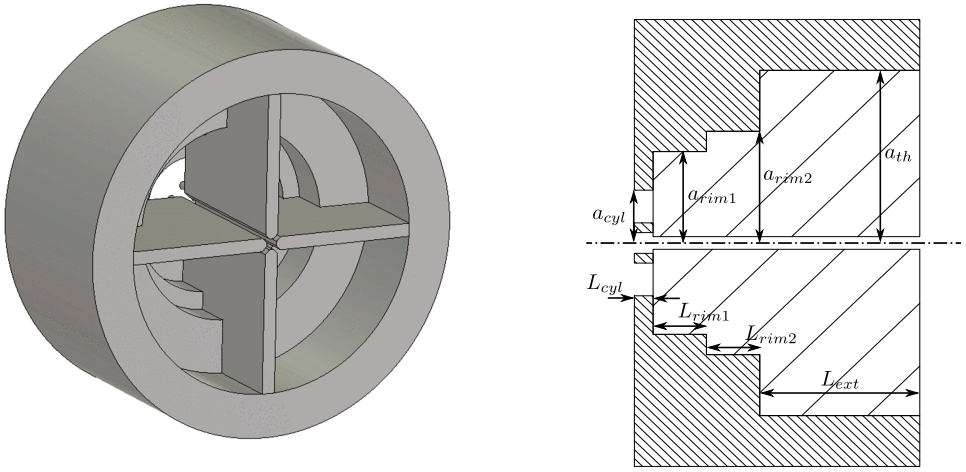

Figure 5.12: The stepped throat section proposed for the unwanted modal suppression. (a) The 3D view of the CST-MWS model. (b) The parameterised cross-section view.

Teflon is used due to its low loss and has a permittivity of 2.1. For the specific quadraxial line a characteristic impedance of 128 Ω is obtained. Although the impedance is significantly reduced, the effect of it is that the cut-off frequencies are lowered in the quadraxial line and consequently a stronger excitation of unwanted modes in the throat occur – similar to the illustration in Fig. 3.18 for the case where $a_{cyl} = 15.5\ mm$. Therefore, to mitigate this the diameter is reduced while the shunt inductance in the equivalent circuit is kept as high as possible. The result is a diameter of $a_{cyl} = 10.4\ mm$.

A standard rod size of diameter 1.92 mm is used for the pins. The sheet thickness of the back wall is chosen to be 3 mm. With this new configuration the sidewall steps in the throat are optimised in CST-MWS to improve the modal content even more. The S-parameter goals are chosen in such a way that the aperture efficiencies at the mid and highest frequencies would be increased without degrading the input match.

The input reflection coefficient of this new feed, referred to as $Feed3$, is shown in Fig. 5.14. Clearly the input match is improved with the usage of the dielectric material, with $\Gamma_{in} < -7\ dB$ over most of the bandwidth and a relative improvement of 3 dB, compared with $Feed1$. The resulting efficiencies are plotted in Fig. 5.15(a). Compared with the results in Fig. 5.13, η_{OG} is improved with 1.5% at 6.75 GHz which corresponds to the 2 dB suppression of TE_{12} in Fig. 5.15(b). Although the other unwanted modes are more strongly excited around 11 GHz, they are well suppressed at the problematic highest frequency and consequently η_{OG} is improved to above 50%. The average aperture efficiency over the entire operational band is 54% and corresponds well with that of the synthesised pure-mode horn depicted by the dashed line in Fig. 5.15(a). The dimensions for the final throat section including the quadraxial feed is listed in Table 5.3.

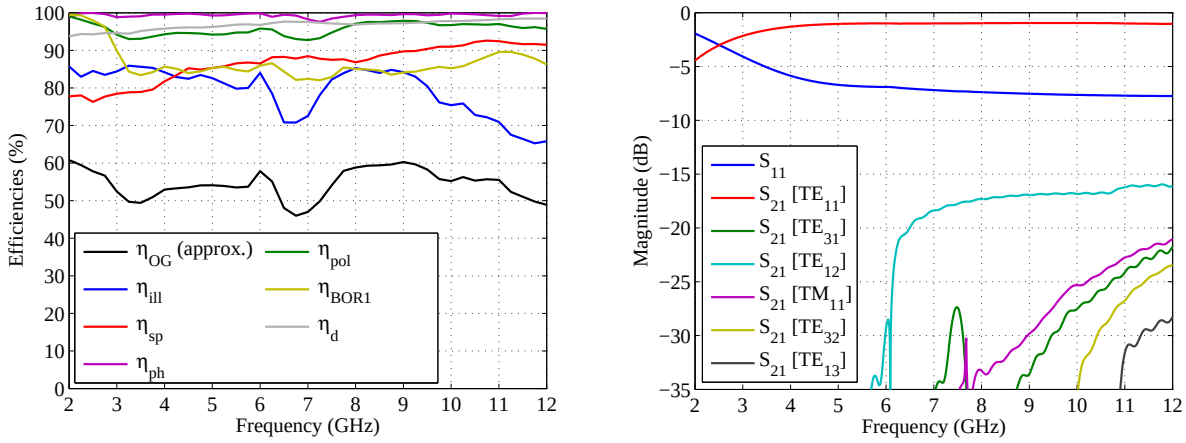

Figure 5.13: The results of *Feed*2. (a) All the approximated efficiencies of the horn in the OG system. (b) The S-parameters of the significant modes excited in the throat section by the quadraxial feed.

Table 5.3: Final dimensions of quadraxial feed and throat section (i.e. *Feed*3).

Parameter	Value (mm)	Parameter	Value (mm)
a_{cyl}	10.4	a_{rim2}	24.41
a_{pin}	0.96	L_{rim2}	8
a_{sep}	3	a_{th}	34
L_{cyl}	3	L_{ext}	5
a_{rim1}	18.67		
L_{rim1}	11.6		

5.4 Manufacturing of prototype

In order to make the prototype QRFH manufacturable and measurable with standard equipment, practical alterations of the structure are required. The manufacturing process and different parts of the antenna are discussed in this section.

5.4.1 PCB for measurement capability

For the purpose of measurements, the multi-pin port used in the design must be connected to four coaxial connectors. This is simply realised by the PCB layout in Fig. 5.16. Each pin feeds through a hole in the PCB and terminates in a 50 Ω co-planar waveguide (CPW) line, as indicated in the respective sub-figures. Each pin inside the substrate is surrounded by vias which forms a coaxial guide, in order to ensure a good transition. The gap between the grounded top layer and solder pad, where the pin will be cut off and soldered to, is kept very small as well as the size of the pad itself.

The substrate used is Mercurywave 9350 with a permittivity of 3.5. A dielectric thickness of 0.2 *mm* is used in order to keep the low impedance coaxial line inside the substrate – formed by each pin and the surrounding vias – as short as possible. The CPW lines are each 14 *mm* in length to allow for time-gating measurements.

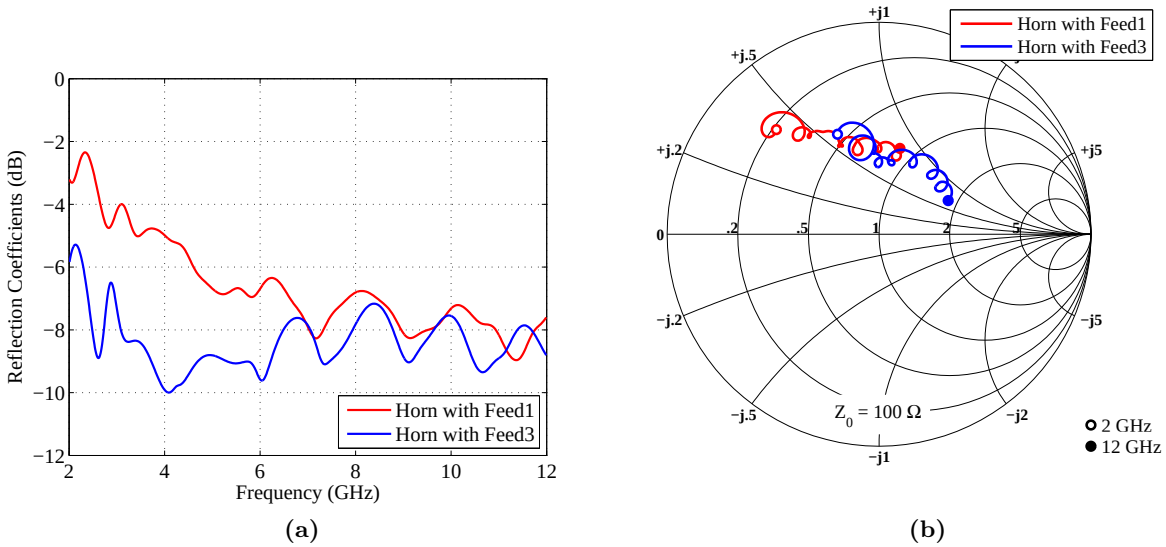

(a) (b)

Figure 5.14: The input reflection coefficients of the horn with $Feed1$ and $Feed3$.

The QRFH can be characterised by performing single-ended measurements at the termination planes of the PCB, followed by the transformation to the differential-mode. Consider the port configuration shown in Fig. 5.17 where a 180° hybrid coupler is employed per polarisation. For the normal operation of the QRFH the pins are excited in the differential-mode by ports $DM1$ and $DM2$. If it is assumed that the pin excitations are uncoupled – which is the case with the uncoupled CPW lines – it can be shown [74] that the single-ended S-parameters (S_{SE}) are related to the mixed-mode S-parameters (S_{MM}) as

$$S_{MM} = M\, S_{SE}\, M^{-1}, \tag{5.1}$$

where

$$M = \frac{1}{\sqrt{2}} \begin{bmatrix} 1 & 0 & -1 & 0 \\ 0 & 1 & 0 & -1 \\ 1 & 0 & 1 & 0 \\ 0 & 1 & 0 & 1 \end{bmatrix}, \tag{5.2}$$

$$S_{SE} = \begin{bmatrix} S_{11} & S_{12} & S_{13} & S_{14} \\ S_{21} & S_{22} & S_{23} & S_{24} \\ S_{31} & S_{32} & S_{33} & S_{34} \\ S_{41} & S_{42} & S_{43} & S_{44} \end{bmatrix} \tag{5.3}$$

and

$$S_{MM} = \begin{bmatrix} [S_{DD}] & [S_{DC}] \\ [S_{CD}] & [S_{CC}] \end{bmatrix}. \tag{5.4}$$

The mixed-mode matrix consists of four two-port matrices, where S_{DD} are the differential-mode S-parameters, S_{CC} the common-mode S-parameters and $S_{DC/CD}$ the cross-mode S-parameters.

Due to the dependence of the E-fields on the induced voltages of the QRFH, the far-fields

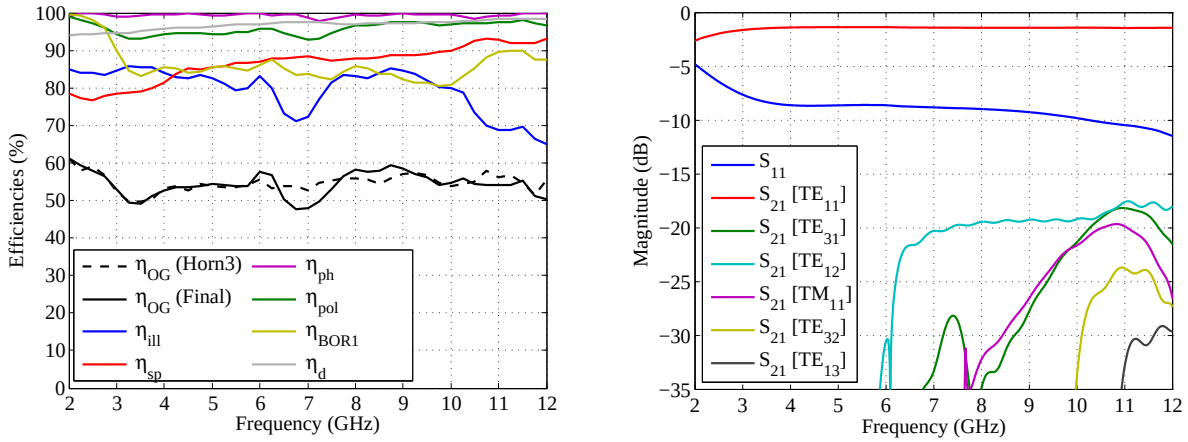

Figure 5.15: Results for the final horn with the matched quadraxial feed and optimal throat section (i.e. *Feed*3). (a) All the approximated efficiencies of the horn in the OG system. The dashed line represents *Horn*3 with the pure-mode excitation. (b) The S-parameters of the significant modes excited in the throat section by the quadraxial feed.

can similarly be transformed as

$$F_{MM} = M\, F_{SE}, \tag{5.5}$$

where F_{SE} and F_{MM} are 4×1 matrices of the single-ended and mixed-mode electric far-fields, respectively.

5.4.2 Manufactured prototype

In the design simulations the sidewall of the QRFH has only been modelled as a sheet. In Fig. 5.18(a) the sidewall of the manufactured prototype is shown with a finite thickness of more than 10 mm. The horn structure is lathed from a solid block of Aluminium 6082. Therefore, in order to avoid shuddering during this process the sidewall should be kept as thick as possible. The ridges, indicated with red in Fig. 5.18(a), are inserted as separate parts as illustrated in Fig. 5.18(b). The purpose of the stepped planes used on the outside surface is to create a reference in the cross-section for the drilling of the perpendicular holes, as seen in Fig. 5.18(a). These holes are specifically for the screws that fixes the ridges to the sidewall. The inside surface of the horn is approximated with arcs in the longitudinal direction, in order for the lathe to machine continuous smooth surfaces. This deviation from the calculated profile used in the CST-MWS model is negligible.

The ridges are laser-cut and the inner edges chamfered with a drill bit that has a 45° edge. The pins are implemented using Brass rods and press-fitted into holes in the backside of the ridges. The PCB is placed onto the back as shown in Fig. 5.16(b), with the pins sticking through the board and soldered to the top layer. The back of the horn is constructed as illustrated in Fig. 5.19(a) to accommodate a complete detachable cover for the PCB. The SMA connectors are attached to this cover alone, in order to be able to replace the PCB if required, without having to make any physical changes to the horn structure itself. Due to the large size of this

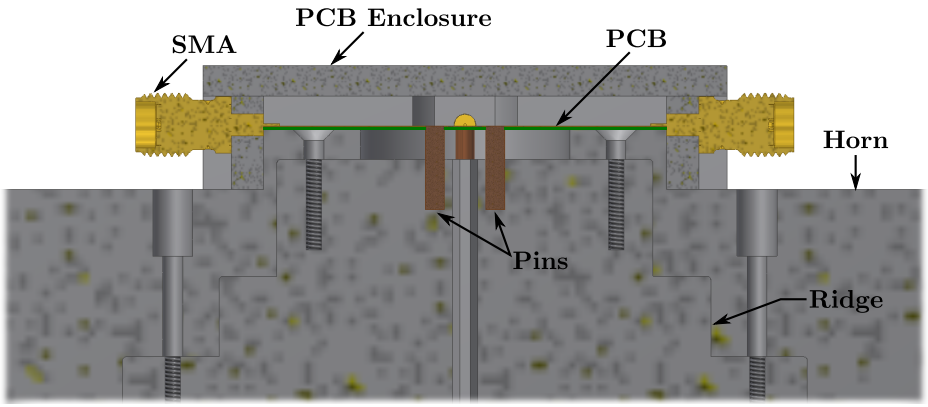

(a)

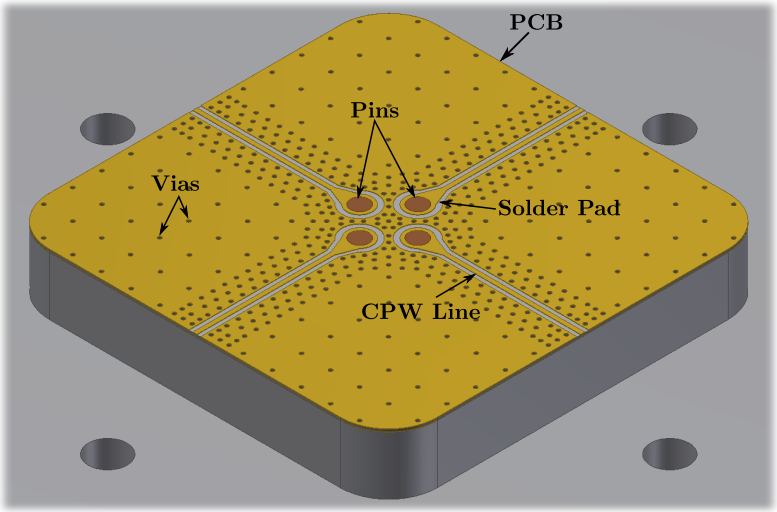

(b)

Figure 5.16: (a) Cross-section view and (b) top view of the PCB solution on the back of the horn.

PCB higher-order modes can propagate in the required cavity with dimensions $(1.6\lambda)^2 \times 0.12\lambda$ at 12 GHz. Therefore, the PCB cover has a sidewall configuration as shown in Fig. 5.19(b). The cover presses on the grounded parts of the substrate and allows for signal propagation only along the CPW lines. The complete assembly is shown in Fig. 5.19(a) with pictures of the final product in Fig. 5.20.

5.5 Simulated performance of prototype

In this section the final results of the full-wave simulated QRFH are given, where all the material losses are included and each of the four CPW lines is excited with a waveguide port in CST-MWS, unless stated otherwise.

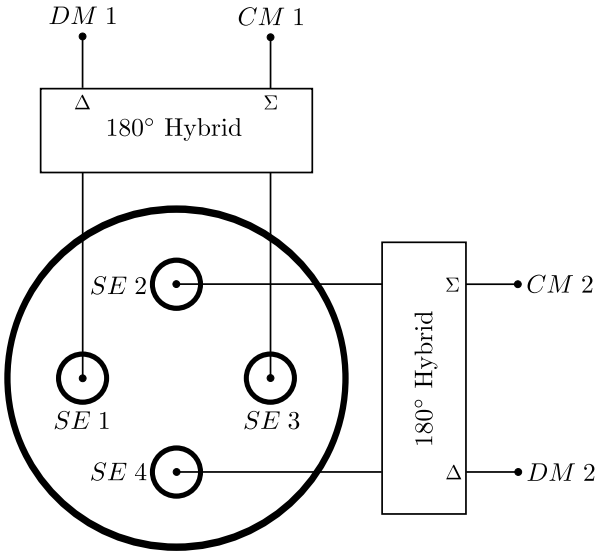

Figure 5.17: The port configuration of the quadraxial feeding.

5.5.1 QRFH results

The input reflection coefficients of the QRFH are given in Fig. 5.21. The result of the differentially excited CPW lines are plotted against that of the pin excitation. It is clear that at both the lowest and highest frequencies the PCB transition degrades the input match. The former is due to the series capacitance caused by the solder pad, while the latter is caused by the series inductance of the pins feeding through the PCB.

As shown in Subsection 2.2.3, the receiver sensitivity is directly dependent on the noise matching between the LNA and antenna. Although Γ_{in} of the pin excitation is above $-10\ dB$, which is the typical maximum value obtained with the WBSPFs currently contending for SKA (see Section 2.5), the locus in Fig. 5.21(b) has potential for an integrated dLNA design. From equation (2.4) it is seen that the typical optimal source impedance (Z_{opt}) for the noise matching of field-effect transistors, which are widely used at microwave frequencies, is inductive. Although the resistance of Z_{opt} is high at lower frequencies and low at higher frequencies as opposed to Γ_{in} of the QRFH, for future work this property may be favourable for matching a transistor more optimally to the proposed QRFH configuration for high sensitivity.

In Fig. 5.22 the far-field patterns are given for different azimuthal planes over the frequency range with 1 GHz intervals from 2 to 12 GHz. As expected the beamwidth in the E-plane is more constant over frequency compared to the H-plane. The ripples in the E-plane patterns are due to the boundary condition on the E-fields and are typically found with smooth-wall horns. The aperture flare part however reduces it to an extent. Lastly, it is seen in Fig. 5.22(d) that the cross-polarisation sidelobes peak at 3 GHz in the D-plane, with a normalised value of $-7.5\ GHz$.

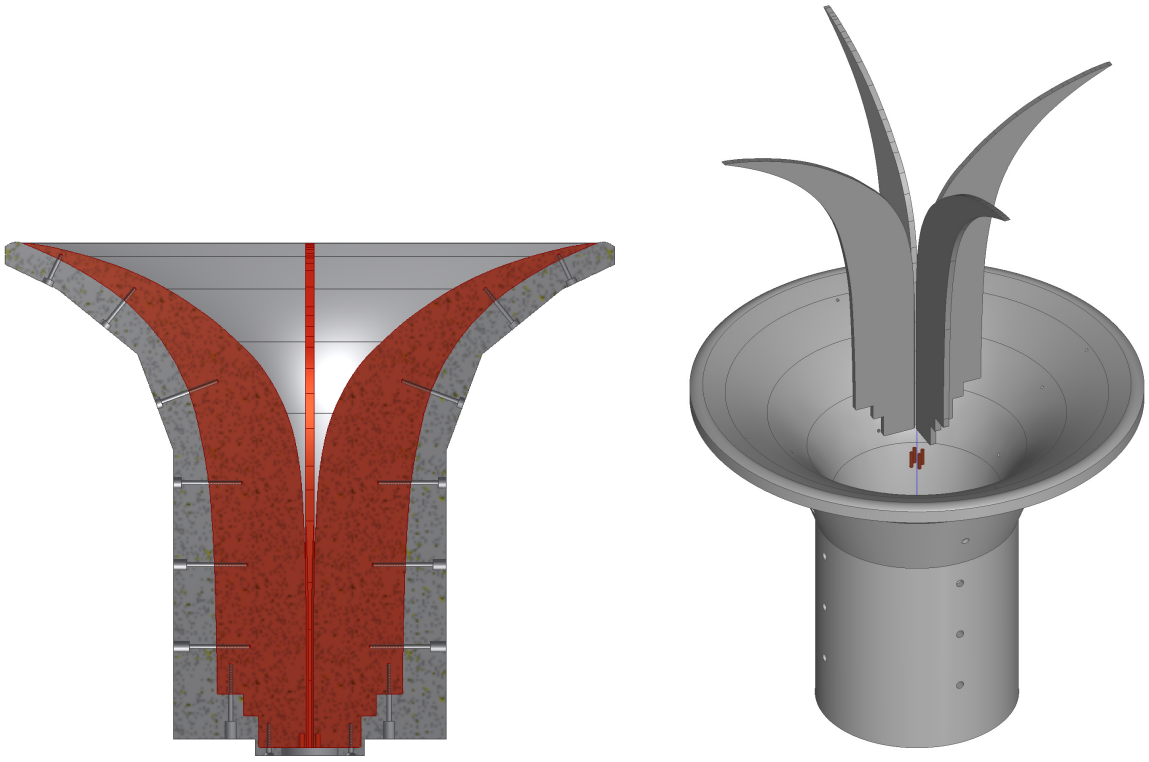

(a) (b)

Figure 5.18: (a) A cross-section view of the QRFH where the ridges are indicated with red. (b) Assembly of the horn structure with the ridges and the four pins.

5.5.2 QRFH in OG system

The far-fields of the simulated QRFH are placed in the OG system and the aperture efficiencies are calculated using physical optics in GRASP. In Fig. 5.23(a) the sub-efficiencies determined with the closed-form equations are given with the former results. Good agreement is found with the approximated aperture efficiencies, and compared to Fig. 5.15(a) the PCB has minimal effects. Furthermore, the phase centre is determined for each frequency and given in Fig. 5.15(b). Note that the variation in phase centre varies less than the reported 50 mm of the design in [2]. By considering only the upper frequency range from 7 to 12 GHz, the optimal position of the feed antenna which produces maximum η_{ph}, is determined as -64 mm from the aperture.

The prototype antenna was designed only for high aperture efficiency, however; it is appropriate to use these results to estimate the receiver sensitivity – as this is the main figure of merit for radio astronomy. Following [72], a technique proposed in [75] is used to determine the antenna noise temperature [see equation (2.7)]. The results are shown in Fig. 5.24 for different tipping angles (θ_p) of the reflector system (depicted in Fig. 2.2). The noise temperature is largest for the $\theta_p = 60°$ case, and is expected due to the contribution of the sub-reflector spillover that primarily illuminates the ground surface at this angle – hence the need for an sub-reflector extension as discussed in Subsection 2.4.1. With the reflector antenna pointing towards zenith, the antenna noise temperature is below 20 K across the operational bandwidth.

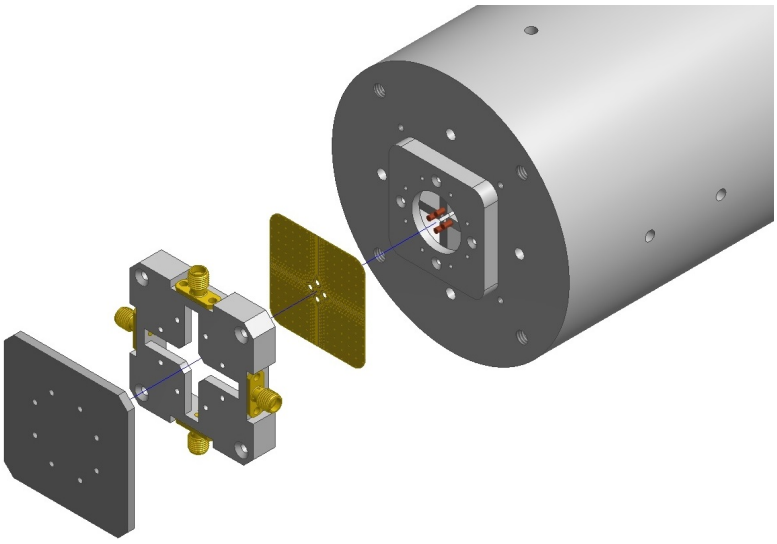

(a)

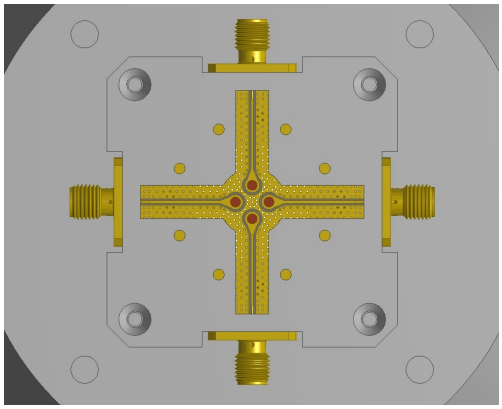

(b)

Figure 5.19: (a) The assembly of the different parts used on the back of the QRFH. (b) The PCB press-fitted to the horn with the one part of its enclosure.

The results of a widely used broadband LNA developed at Caltech are chosen for the sensitivity calculations. In [76] the measured noise temperature is reported to be less than 8 K from 2 to 12 GHz, cooled in a cryostat at 20 K. Due to the compact solution which the quadraxial feed poses, the entire active antenna should be small enough for operation inside a cryostat. Therefore, the sensitivity is calculated for a receiver also operating at 20 K.

The final parameter required for this calculation is the radiation efficiency. Through simulations this is found to vary between 80% and 90% over the bandwidth. The most significant contribution to this performance in the prototype is the ohmic losses of the Aluminium 6082 – with negligible contributions from the Teflon and Brass rods. For higher radiation efficiencies the structure could also be silver-plated.

Using all of these values the sensitivity is calculated with equations (2.2) and (2.27), and shown in Fig. 5.24(b) for three different tipping angles. For the system pointed towards zenith the sensitivity is highest, with an average value of 3.54 m^2/K over the bandwidth. This value deteriorates rapidly as the antenna noise temperature increases.

(a)

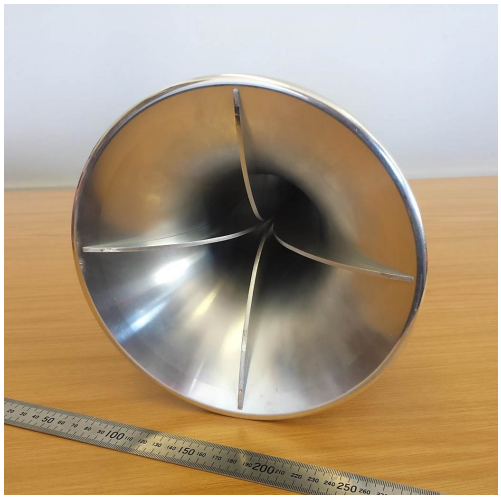

(b)

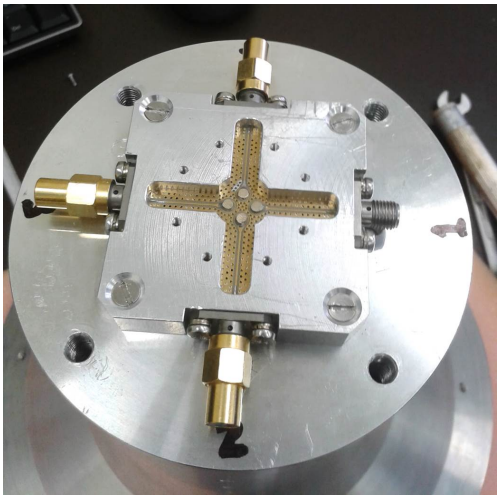

(c)

Figure 5.20: Pictures of (a) the manufactured QRFH with mounting jig, (b) the flared opening and (c) the PCB without its top lid.

Finally, the cross- and co-polar gain levels of both the QRFH alone and as a feed in the OG system, are given in Fig. 5.25. The normalised peak cross-polarisation has a mean value across the bandwidth of $-9\ dB$. In the OG system this is reduced to well below $-10\ dB$. For the FoV within the half-power beam, as typically considered for pulsar timing, the peak cross-polar levels of the OG system are around $-20\ dB$. Furthermore, the co-polar gain of the QRFH is above $10\ dB$, while in the OG system it produces between 48 and 63 dB gain.

5.5.3 Multi-mode excitation

To evaluate the effectiveness of the quadraxial feed for the purpose of integrating dLNAs, the common-mode is included in the excitation of the simulated QRFH. If it is assumed that the single-ended ports are uncoupled, which is the case with the 4-port PCB, and a hypothetical dLNA is characterised with the input impedance of the antenna, weights can be calculated

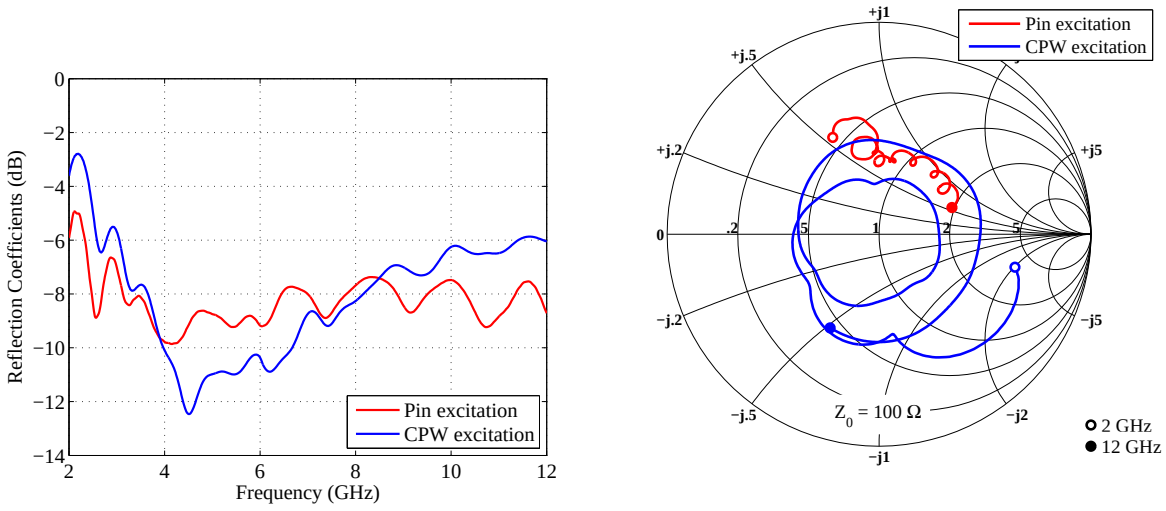

(a) **(b)**

Figure 5.21: The simulated reflection coefficients of the differentially excited QRFH with and without the PCB.

directly from the value of the common-mode rejection ratio of the dLNA and applied to the far-fields.

The common-mode rejection ratio (CMRR) is defined as the ratio between the differential-mode gain (G_{DM}) and the common-mode gain (G_{CM}). Thus if one assumes a perfect match of both these modes, the mixed-mode far-fields of a single-polarisation can be calculated using equation (5.5) as

$$F_{MM1} = \frac{1}{\sqrt{2}} \left[(w_{CM} + w_{DM}) F_{SE1} + (w_{CM} - w_{DM}) F_{SE3} \right], \tag{5.6}$$

where F_{SE1} and F_{SE3} are the E-Fields of the single-ended excitations shown to Fig. 5.17. The differential-mode weight is denoted by w_{DM} and the common-mode weight is simply calculated as

$$w_{CM} = \frac{w_{DM}}{CMRR}. \tag{5.7}$$

In order to adhere to the conservation of energy, the weights must satisfy

$$|w_{CM}|^2 + |w_{DM}|^2 = 1. \tag{5.8}$$

With equations (5.6) to (5.8) the mixed-mode far-fields are calculated and the results are shown in Fig. 5.26. From Fig. 5.26(a) it is clear that $CMRR = 20\ dB$ has a negligible affect on the far-field magnitudes. With $CMRR = 3\ dB$ the peak cross-polarisation levels are increased over the bandwidth due to the common-mode, while the gain is decreased. In Fig. 5.26(b) the efficiencies of the QRFH in the OG system are shown. As expected the $BOR1$ efficiency is decreased due to the non-ideal radiation of the common-modes, and consequently the aperture efficiency decreases over the frequency range with more than 5%, compared to Fig. 5.23(a).

In [77] a dLNA is reported for the implementation with an Eleven-feed antenna. This high

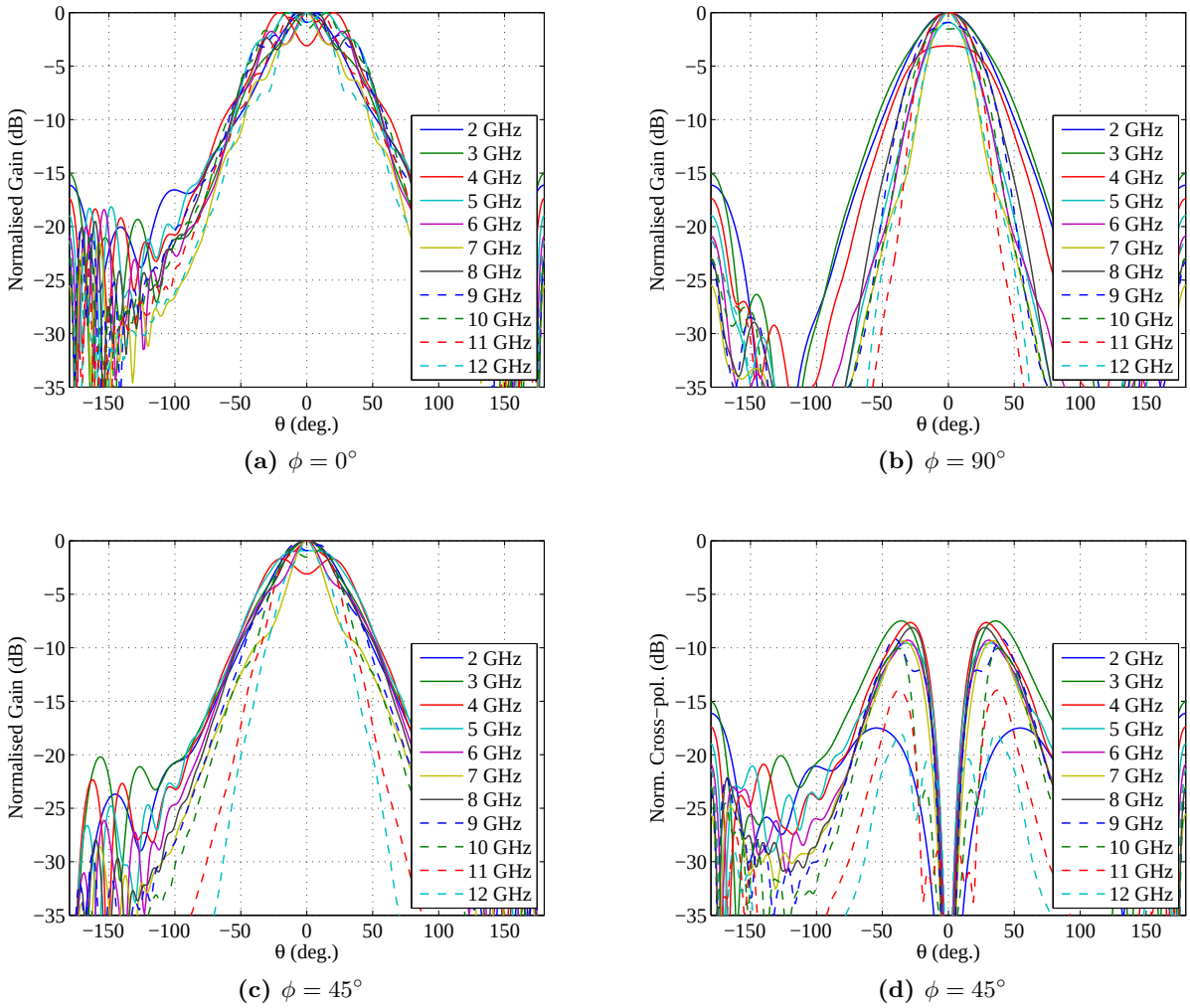

(a) $\phi = 0°$ **(b)** $\phi = 90°$

(c) $\phi = 45°$ **(d)** $\phi = 45°$

Figure 5.22: The co- and cross-polar far-field patterns of the simulated QRFH including the CPW transition.

performance MMIC design obtains a measured CMRR of more than 30 dB from 2 to 12 GHz. This value also agrees with the work reported in [78], where a dLNA is designed for operating from DC to 4 GHz. Therefore, given this CMRR value and following the results in Fig. 5.26, the premise for integrating dLNAs with a QRFH by means of a quadraxial feed seems valid; however, additional work is required to achieve a practical solution for such an integration.

5.6 Measurements

The far-field radiation of the manufactured prototype shown in Fig. 5.20, was measured in an anechoic chamber using dual-ridged horns. In Fig. 5.27(a) the realised gain is shown and agrees well with the simulated results. A sudden drop is found at 3.5 GHz – which is even more pronounced with the available gain in Fig. 5.26 – and is due to the flat top beam which has less peak gain, caused by the lower TE_{11} magnitude in the aperture. The normalised peak cross-polar levels are also shown in Fig. 5.27(a) and here the measured results are lower than with the simulation. This could be ascribed to the precision of the position of the probe horn.

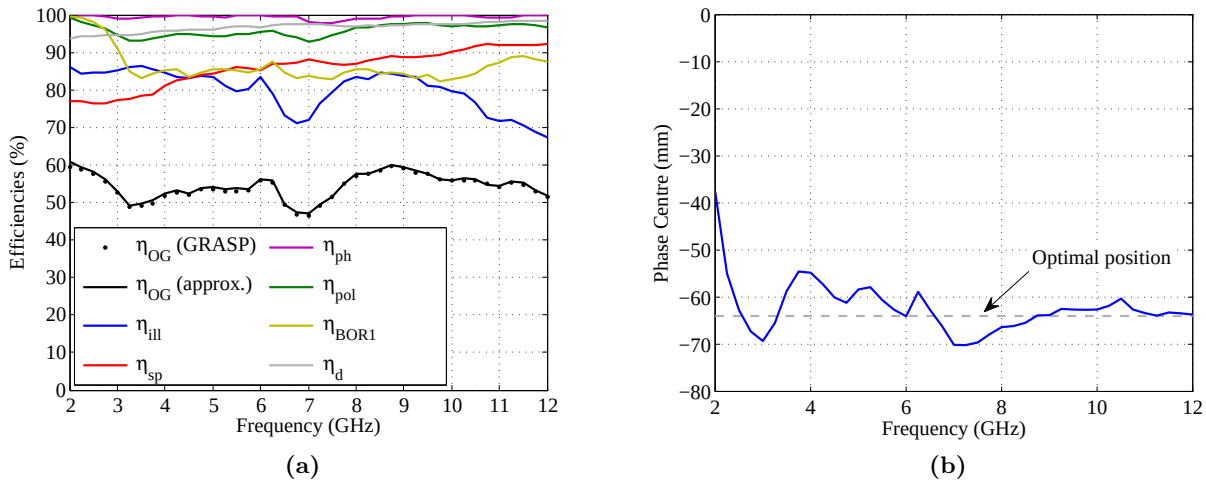

(a) **(b)**

Figure 5.23: Results of the simulated QRFH including the CPW transition. (a) The calculated sub-efficiencies of the far-fields in the OG system, including the results from the GRASP simulation. (b) The phase centres with respect to the aperture of the QRFH. Each location is determined by moving the aperture of the horn relative to the focus of the reflector, in order to achieve maximum phase efficiency.

The measurement system is rather manual and the probe horn is rotated by hand. Therefore it is easy to miss the cross-polar peak in the 45° azimuthal angle.

In Fig. 5.27(b) the S-parameters of the differential-mode excitations are shown. The measured input match across the operational bandwidth is found to be better for both differential ports 1 and 2, compared with the simulated results. The consequence of this is however an increased isolation level. In the simulation perfect two-fold symmetry is obtained and therefore the theoretical isolation is close to perfect. This however is not the case with the fabricated QRFH, as clearly seen from the $|S_{21}|$ results that peak at $-32\ dB$ in the band of operation. Note also that the S-parameters do not degrade significantly above 12 GHz. Therefore, if it is acceptable to have a narrower beamwidth, i.e. a lower η_{ill}, then this QRFH could be operated above 12 GHz.

The far-field patterns in the E- and H-planes are plotted against the simulated results in Fig. 5.28 for six different frequencies. In all of these cases the patterns agree well with the simulation. Note that only the results for the measured single-ended ports 1 and 3 are shown, although similar accuracy is obtained with ports 2 and 4. At 2 GHz beam squinting is found in the E-plane as seen from Fig. 5.28(a). At 4 and 12 GHz – shown respectively in Figs. 5.28 (b) and (f) – there exists some rotational asymmetry in the E-plane of the main beams. The backlobe radiation in most cases are lower than that of the simulation. This is largely due to the cable running down the back side of the antenna during the measurements, which causes scattering.

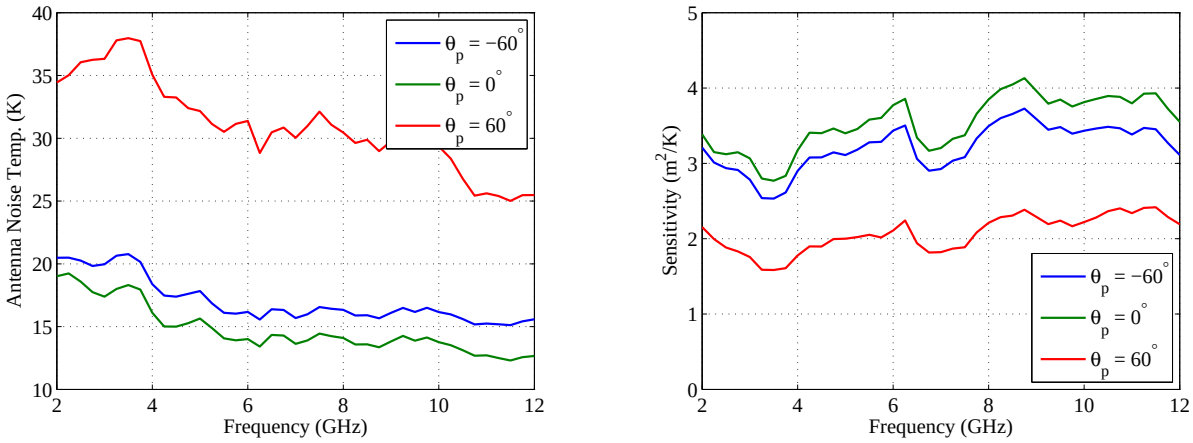

(a) (b)

Figure 5.24: The (a) antenna noise temperature and (b) estimated receiver sensitivity of the OG system employed with the simulated QRFH.

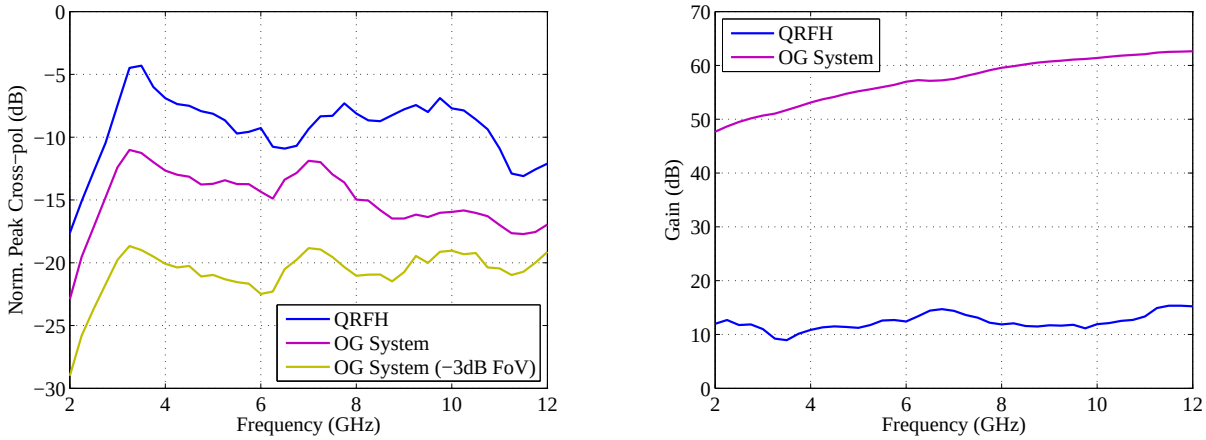

(a) (b)

Figure 5.25: The (a) normalised peak cross-polar levels and (b) gain of the simulated QRFH and OG system.

5.7 Conclusion

In this chapter a systematic approach is proposed and demonstrated for the design of a QRFH. This is done by considering the modal properties in a QRFH, as opposed to the conventional way of directly optimising the various dimensions. A prototype QRFH is designed accordingly for an OG system proposed for SKA. This prototype is successfully manufactured and good agreement is found between the measured and simulated results.

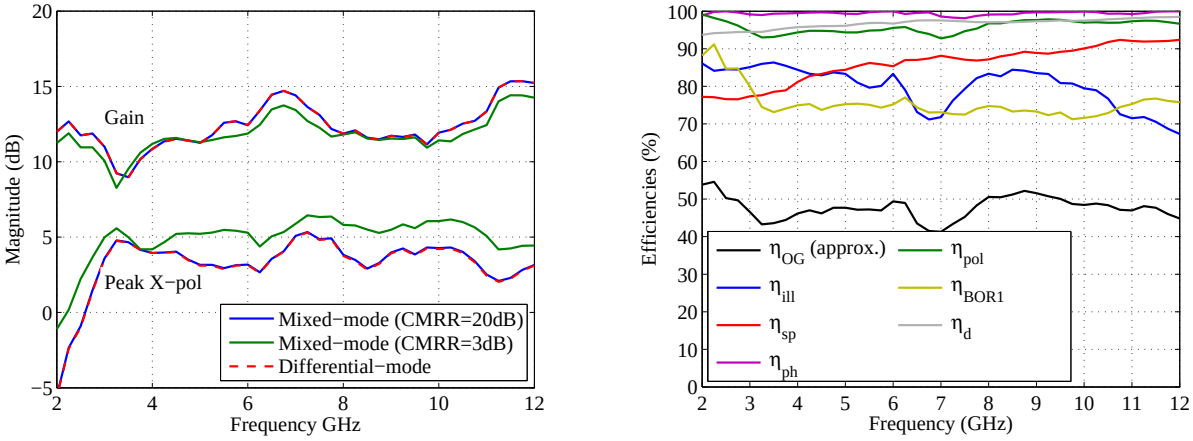

(a) **(b)**

Figure 5.26: (a) The peak co- and cross-polar gain levels resulting from different $CMRR$ values, along with that of the pure differential excitation. (b) The efficiencies obtained when the $CMRR = 3\ dB$.

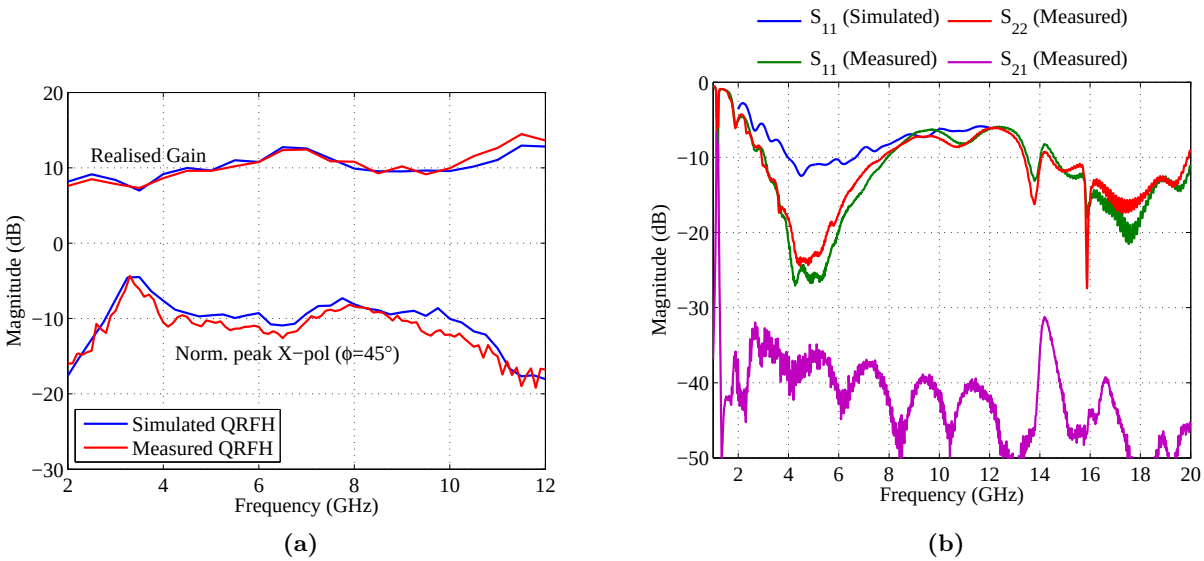

(a) **(b)**

Figure 5.27: The measured results compared to that of the simulation. (a) The realised gain and normalised peak cross-polarisation in the D-plane. (b) The differential-mode S-parameters.

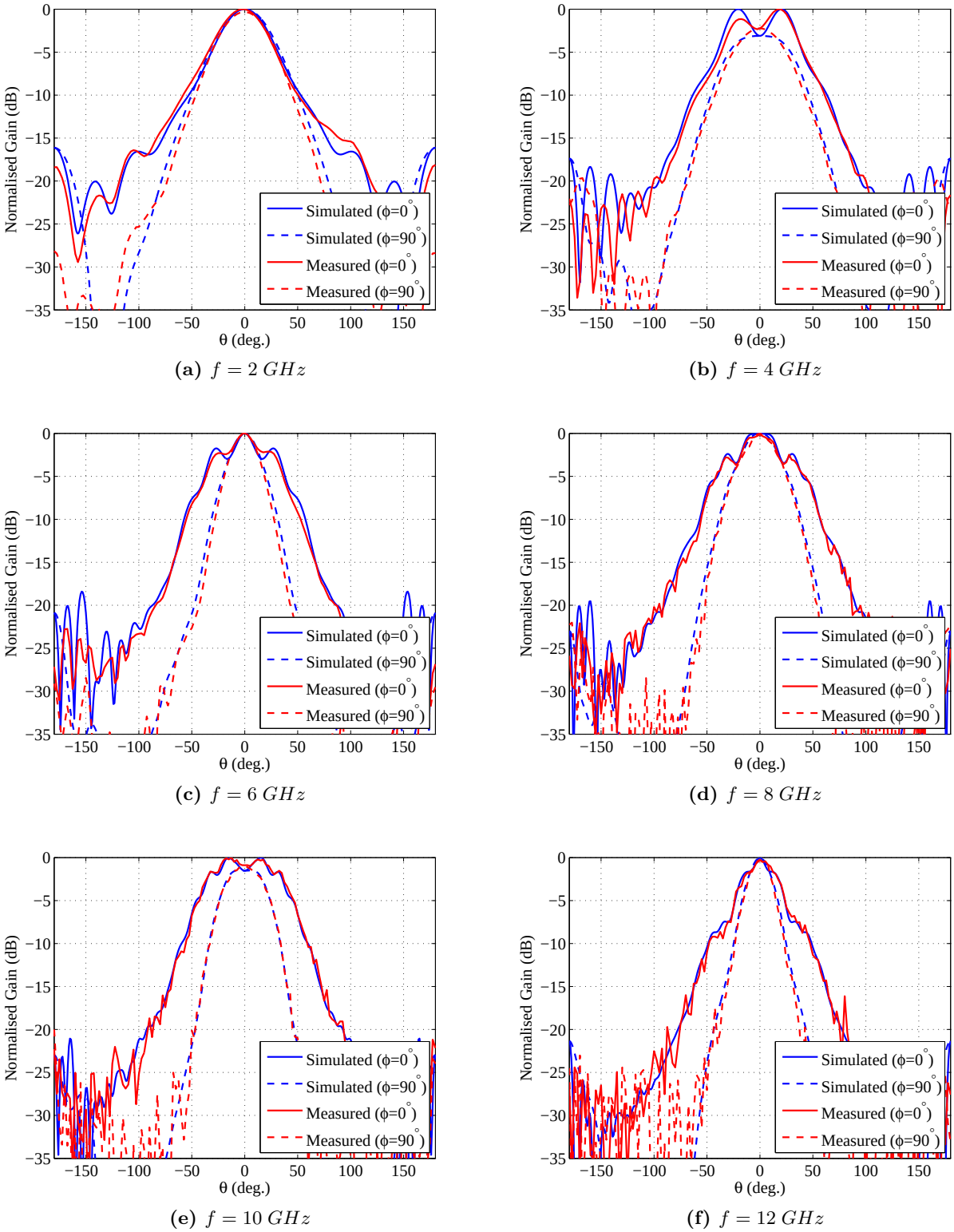

(a) $f = 2\ GHz$ **(b)** $f = 4\ GHz$

(c) $f = 6\ GHz$ **(d)** $f = 8\ GHz$

(e) $f = 10\ GHz$ **(f)** $f = 12\ GHz$

Figure 5.28: The co-polar far-field patterns in the E- and H-planes, of the simulated and measured antennas, for different frequencies.

Chapter 6

Conclusion

In this dissertation modal-based techniques are presented for the effective design of QRFHs as reflector feeds. A new excitation technique is proposed, which allows for the integration with dLNAs. An equivalent circuit of this quadraxial feed is presented that allows fast synthesis of optimal feeding designs for QRFHs. In addition, the quadraxial feeding network suppresses higher-order modes significantly. The effect of eliminating these unwanted modes are investigated and the quadraxial feed is shown to outperform the coaxial feed in the known detrimental aspects of the QRFH, as listed in Section 1.1, for the specific QRFH designs. The drawback however is that a poorer input match is obtained with $\Gamma_{in} < -7\ dB$ over most of the bandwidth. On the other hand, the inductive input impedance of the quadraxial feed does have potential for noise matching with FETs, and might possibly be more optimal than the standard 50 Ω reference impedance.

Ridge-loaded modes were analysed and a large number of cut-off frequencies presented. The pure-mode excitation of the quadraxial feed allows more effective control over the modal content in the QRFH. This is exploited in a proposed design technique where the cut-off frequencies throughout the horn are used to synthesise the ridge taper profile, in order to achieve the desired modal distribution in the aperture.

The feeding solution is compact and therefore is also attractive for use with cryocoolers. A prototype was successfully manufactured and the mechanical implementation of the quadraxial feed proved to be much more simple than that of the conventional coaxial feed – typically realised within the thin ridges.

Future expansions of this work might include the following:

- The quadraxial feed poses the potential of utilising both the differential- and common-modes, which could be used for beam-forming techniques.
- The quadraxial feed could also allow for the calibration of an antenna system. Complex weights could be applied to each of the four pin excitations to alter unwanted manufacturing defects.
- The physical integration of dLNAs and the evaluation of such active horns, compared to the typical single-ended solutions.

- This work was only concerned with circular QRFHs; however, the proposed techniques could also be expanded for square-shaped QRFHs.
- Better results might be obtained with the offset Gregorian system if the reflectors are shaped for the QRFH radiation properties – such as the high cross-polar components in the D-plane.

Bibliography

[1] P. Dewdney, W. Turner, R. Millenaar, R. McCool, J. Lazio, and T. Cornwell, "SKA1 system baseline design," SKA Organisation, The University of Manchester, UK, Tech. Rep., March 2013.

[2] A. Akgiray, S. Weinreb, W. Imbriale, and C. Beaudoin, "Circular quadruple-ridged flared horn achieving near-constant beamwidth over multioctave bandwidth: Design and measurements," *IEEE Trans. Antennas Propag.*, vol. 61, no. 3, pp. 1099–1108, March 2013.

[3] O. B. Jacobs, J. W. Odendaal, and J. Joubert, "Quad-ridge horn antenna with elliptically shaped sidewalls," *IEEE Trans. Antennas Propag.*, vol. 61, no. 6, pp. 2948–2955, June 2013.

[4] H. Lai, R. Franks, D. Kong, D. Kuck, and T. Gackstetter, "A broad band high efficent quad ridged horn," in *Antennas and Propagation Society International Symposium*, vol. 25, June 1987, pp. 676–679.

[5] F. King, J. S. Yee, and D. R. Erbach, "A broadband quadruple-ridged waveguide radiator," Army Missile Research, Development and Engineering Laboratory, Redstone Arsenal, AL, USA, Tech. Rep. RE-74-7, 1974.

[6] J. L. Kerr, "Broadband horns," Army Electronics Command, Fort Monmouth, NJ, USA, Tech. Rep. AD0712299, 1970.

[7] T. S. Beukman, M. V. Ivashina, R. Maaskant, P. Meyer, and C. Bencivenni, "A quadraxial feed for ultra-wide bandwidth quadruple-ridged flared horn antennas," in *The 8th European Conference on Antennas and Propagation (EuCAP)*, The Hague, The Netherlands, April 2014.

[8] T. S. Beukman, P. Meyer, M. V. Ivashina, R. Maaskant, and de Villiers D. I. L., "Modal considerations for synthesizing the tapering profile of a quadruple-ridged flared horn antenna," in *International Conference on Electromagnetics in Advanced Applications (ICEAA)*, Palm Beach, Aruba, August 2014.

[9] T. S. Beukman, P. Meyer, R. Maaskant, and M. V. Ivashina, "Equivalent circuit of a quadraxial feed for ultra-wide bandwidth quadruple-ridged flared horn antennas," in *The 9th European Conference on Antennas and Propagation (EuCAP)*, Lisbon, Portugal, April 2015.

[10] "IEEE standard for definitions of terms for antennas," *IEEE Std 145-2013 (Revision of IEEE Std 145-1993)*, pp. 1–50, March 2014.

[11] H. A. Haus, W. R. Atkinson, G. M. Branch, W. B. Davenport, W. H. Fonger, W. A. Harris, S. W. Harrison, W. W. McLeod, E. K. Stodola, and T. E. Talpey, "Representation of noise in linear twoports," *Proceedings of the IRE*, vol. 48, no. 1, pp. 69–74, January 1960.

[12] M. W. Pospieszalski, "Modeling of noise parameters of MESFETs and MODFETs and their frequency and temperature dependence," *IEEE Trans. Microw. Theory Techn.*, vol. 37, no. 9, pp. 1340–1350, 1989.

[13] ——, "Interpreting transistor noise," *IEEE Microwave Magazine*, vol. 11, no. 6, pp. 61–69, 2010.

[14] G. C. Medellín, "Antenna noise temperature calculations," National Astronomy and Atmospheric Center, Cornell University, Ithaca, NY, USA, Tech. Rep., September 2004.

[15] M. Ivashina, R. Maaskant, and B. Woestenburg, "Equivalent system representation to model the beam sensitivity of receiving antenna arrays," *IEEE Antennas Wireless Propag. Lett.*, vol. 7, pp. 733–737, October 2008.

[16] W. V. T. Rusch and P. D. Potter, *Analysis of Reflector Antennas.* New York: Academic Press, 1970.

[17] P. S. Kildal and Z. Sipus, "Classification of rotationally symmetric antennas as types BOR_0 and BOR_1," *IEEE Antennas Propag. Mag.*, vol. 37, no. 6, p. 114, December 1995.

[18] A. C. Ludwig, "The definition of cross polarization," *IEEE Trans. Antennas Propag.*, vol. 21, no. 1, pp. 116–119, January 1973.

[19] P.-S. Kildal, "Factorization of the feed efficiency of paraboloids and cassegrain antennas," *IEEE Trans. Antennas Propag.*, vol. 33, no. 8, pp. 903–908, August 1985.

[20] ——, "Combined E- and H-plane phase centers of antenna feeds," *IEEE Trans. Antennas Propag.*, vol. 31, no. 1, pp. 199–202, January 1983.

[21] D. I. L. de Villiers, "Offset dual-reflector antenna system efficiency predictions including subreflector diffraction," *IEEE Antennas Wireless Propag. Lett.*, vol. 10, pp. 947–950, 2011.

[22] TICRA, Copenhagen, Denmark. GRASP10, Version 10.0.1. [Online]. Available: http://www.ticra.com

[23] I. P. Theron, R. Lehmensiek, and D. I. L. de Villiers, "Towards an optics design for SKA," in *IEEE AFRICON Conference in Africa*, Mauritius, September 2013.

[24] W. Rusch, J. Prata, A., Y. Rahmat-Samii, and R. A. Shore, "Derivation and application of the equivalent paraboloid for classical offset cassegrain and gregorian antennas," *IEEE Trans. Antennas Propag.*, vol. 38, no. 8, pp. 1141–1149, August 1990.

[25] P.-S. Kildal, *Foundations of antennas: A unified approach for line-of-sight and multipath.* Compendium in Antenna Engineering at Chalmers, 2014.

[26] M. V. Ivashina, C. Bencivenni, O. Iupikov, and J. Yang, "Optimization of the 0.35-1.05 GHz quad-ridged flared horn and eleven feeds for the Square Kilometer Array baseline design," in *International Conference on Electromagnetics in Advanced Applications (ICEAA)*, August 2014.

[27] G. Foster, A. Karastergiou, R. Paulin, T. D. Carozzi, and S. Johnston, "Instrumental polarization properties and high-precision pulsar timing," *Monthly Notices of the Royal Astronomical Society*, submitted for publication.

[28] T. D. Carozzi and G. Woan, "A fundamental figure of merit for radio polarimeters," *IEEE Trans. Antennas Propag.*, vol. 59, no. 6, pp. 2058–2065, June 2011.

[29] M. V. Ivashina, "Private communications," April 2014.

[30] R. Lehmensiek and I. P. Theron, "The design of the MeerKAT L-band feed," in *International Conference on Electromagnetics in Advanced Applications (ICEAA)*, September 2012, pp. 321–324.

[31] G. Cortes-Medellin, "Non-planar quasi-self-complementary ultra-wideband feed antenna," *IEEE Trans. Antennas Propag.*, vol. 59, no. 6, pp. 1935–1944, June 2011.

[32] R. Gawande and R. Bradley, "Towards an ultra wideband low noise active sinuous feed for next generation radio telescopes," *IEEE Trans. Antennas Propag.*, vol. 59, no. 6, pp. 1945–1953, June 2011.

[33] J. Yang, M. Pantaleev, P.-S. Kildal, and L. Helldner, "Design of compact dual-polarized 1.2-10 GHz eleven feed for decade bandwidth radio telescopes," *IEEE Trans. Antennas Propag.*, vol. 60, no. 5, pp. 2210–2218, May 2012.

[34] J. Yang, M. Pantaleev, P.-s. Kildal, B. Klein, Y. Karandikar, L. Helldner, N. Wadefalk, and C. Beaudoin, "Cryogenic 2-13 GHz eleven feed for reflector antennas in future wideband radio telescopes," *IEEE Trans. Antennas Propag.*, vol. 59, no. 6, pp. 1918–1934, June 2011.

[35] J. Yin, J. Yang, M. Pantaleev, and L. Helldner, "The circular eleven antenna: A new decade-bandwidth feed for reflector antennas with high aperture efficiency," *IEEE Trans. Antennas Propag.*, vol. 61, no. 8, pp. 3976–3984, August 2013.

[36] J. Welch, D. Backer, L. Blitz, D. C.-J. Bock, G. C. Bower, C. Cheng, S. Croft, M. Dexter, G. Engargiola, E. Fields, and et al., "The allen telescope array: The first widefield, panchromatic, snapshot radio camera for radio astronomy and SETI," *Proceedings of the IEEE*, vol. 97, no. 8, pp. 1438–1447, August 2009.

[37] W. A. Imbriale, S. Weinreb, G. Jones, H. Mani, and A. Akgiray, "The design and performance of a wideband radio telescope for the GAVRT program," *IEEE Trans. Antennas Propag.*, vol. 59, no. 6, pp. 1954 –1962, June 2011.

[38] O. B. Jacobs, J. Odendaal, and J. Joubert, "Elliptically shaped quad-ridge horn antennas as feed for a reflector," *IEEE Antennas Wireless Propag. Lett.*, vol. 10, pp. 756–759, 2011.

[39] A. Akgiray, S. Weinreb, and W. Imbriale, "The quadruple-ridged flared horn: A flexible, multi-octave reflector feed spanning f/0.3 to f/2.5," in *European Conference on Antennas and Propagation (EuCAP)*, April 2013, pp. 768–769.

[40] C. S. Lee, S. W. Lee, and S. L. Chuang, "Plot of modal field distribution in rectangular and circular waveguides," *IEEE Trans. Microw. Theory Techn.*, vol. 33, no. 3, pp. 271–274, March 1985.

[41] C. A. Balanis, *Advanced Engineering Electromagnetics*, 1st ed. John Wiley & Sons, 1989.

[42] CST Computer Simulation Technology AG, Darmstadt, Germany. CST Microwave Studio, Version 2013.04. [Online]. Available: http://www.cst.com

[43] W. Sun and C. A. Balanis, "Analysis and design of quadruple-ridged waveguides," *IEEE Trans. Microw. Theory Techn.*, vol. 42, no. 12, pp. 2201–2207, December 1994.

[44] M. Chen, G. Tsandoulas, and F. Willwerth, "Modal characteristics of quadruple-ridged circular and square waveguides," *IEEE Trans. Microw. Theory Techn.*, vol. 22, no. 8, pp. 801–804, 1974.

[45] U. Balaji and R. Vahldieck, "Radial mode matching analysis of ridged circular waveguides," *IEEE Trans. Microw. Theory Techn.*, vol. 44, no. 7, pp. 1183–1186, July 1996.

[46] J. Liu and G. Lin, "Analysis of a quadruple corner-cut ridged/vane-loaded circular waveguide using scaled boundary finite element method," *Progress In Electromagnetics Research M*, vol. 17, pp. 113–133, 2011.

[47] D. I. L. de Villiers, P. Meyer, and K. D. Palmer, "Design of a wideband orthomode transducer," in *IEEE AFRICON Conference in Africa*, September 2009, pp. 1–6.

[48] J. C. Slater, *Microwave Transmission.* New York: McGraw-Hill, 1942.

[49] A. Akgiray, S. Weinreb, and W. Imbriale, "Design and measurements of dual-polarized wideband constant-beamwidth quadruple-ridged flared horn," in *Proc. IEEE Antennas Propag. Soc. Int. Symp.*, 2011, pp. 1135–1138.

[50] P. H. van der Merwe, J. W. Odendaal, and J. Joubert, "A dual-polarized ridged horn antenna," in *IEEE-APS Topical Conference on Antennas and Propagation in Wireless Communications (APWC)*, Sept 2012, pp. 595–597.

[51] M. V. Ivashina, E. A. Redkina, and R. Maaskant, "An accurate model of a wide-band microstrip feed for slot antenna arrays," in *Antennas and Propagation Society International Symposium*, June 2007, pp. 1953–1956.

[52] C. Bencivenni, "0.35-1.05 GHz quadruple-ridge flared horn feed for the square kilometre array radio telescope," Onsala Space Observatory, Sweden, Tech. Rep. Rev. 1, 2013.

[53] C. A. W. Vale and P. Meyer, "Automated intelligent mode selection for fast mode matching analysis of waveguide discontinuities," in *IEEE MTT-S International Microwave Symposium*, Phoenix, USA, May 2001.

[54] H. W. Sams, *Reference Data for Radio Engineers*, 2nd ed. New York: International Telephone and Telegraph Corporation, 1946.

[55] A. C. Ludwig, "Radiation pattern synthesis for circular aperture horn antennas," *IEEE Trans. Antennas Propag.*, vol. 14, no. 4, pp. 434–440, July 1966.

[56] A. D. Olver, P. J. Clarricoats, A. A. Kishk, and L. Shafai, *Microwave Horns and Feeds*, ser. Electromagnetic Waves. Institution of Engineering and Technology, 1994.

[57] K. Tomiyasu, "Conversion of te11 mode by a large diameter conical junction," *IEEE Trans. Microw. Theory Techn.*, vol. 17, no. 5, pp. 277–279, May 1969.

[58] K. K. Agarwal and E. R. Nagelberg, "Phase characteristics of a circularly symmetric dual-mode transducer (correspondence)," *IEEE Transactions on Microwave Theory and Techniques*, vol. 18, no. 1, pp. 69–71, Jan 1970.

[59] C. C. H. Tang, "Mode conversion in tapered waveguides at and near cutoff," *IEEE Trans. Microw. Theory Techn.*, vol. 14, no. 5, pp. 233–239, May 1966.

[60] H. Deguchi, M. Tsuji, and H. Shigesawa, "Multimode horn antenna with both high efficiency and low cross polarization," *Electronics and Communications in Japan (Part I: Communications)*, vol. 86, no. 12, pp. 36–43, 2003.

[61] A. D. Olver and X. Jun, "Optimum design of profiled corrugated horns," in *Antennas and Propagation Society International Symposium*, vol. 25, June 1987, pp. 680–683.

[62] J. L. Kerr, "Short axial length broad-band horns," *IEEE Trans. Antennas Propag.*, vol. 21, no. 5, pp. 710–714, Sep 1973.

[63] C. Bruns, P. Leuchtmann, and R. Vahldieck, "Analysis and simulation of a 1-18-ghz broadband double-ridged horn antenna," *IEEE Transactions on Electromagnetic Compatibility*, vol. 45, no. 1, pp. 55–60, February 2003.

[64] C. Y. Tan and K. T. Selvan, "Simulation study of a 4 - 28 ghz double ridged conical horn antenna," in *IEEE International RF and Microwave Conference*, December 2008, pp. 298–301.

[65] A. H. Akgiray, "New technologies driving decade-bandwidth radio astronomy: Quad-ridged flared horn & compound-semiconductor LNAs," Ph.D. dissertation, California Institute of Technology, 2013.

[66] C. Granet, "Profile options for feed horn design," in *Asia-Pacific Microwave Conference*, 2000, pp. 1448–1451.

[67] S. Silver, *Microwave Antenna Theory and Design*, ser. Electromagnetic Waves. Institution of Engineering and Technology, 1984.

[68] A. P. King, "The radiation characteristics of conical horn antennas," *Proceedings of the IRE*, vol. 38, no. 3, pp. 249–251, March 1950.

[69] O. M. Smirnov, B. S. Frank, I. P. Theron, and I. Heyood, "Understanding the impact of beamshapes on radio interferometer imaging performance," in *International Conference on Electromagnetics in Advanced Applications (ICEAA)*, Cape Town, South Africa, September 2012, pp. 586–590.

[70] A. Young, R. Maaskant, M. V. Ivashina, D. I. L. de Villiers, and D. B. Davidson, "Accurate beam prediction through characteristic basis function patterns for the MeerKAT/SKA radio telescope antenna," *IEEE Transactions on Antennas and Propagation*, vol. 61, no. 5, pp. 2466–2473, May 2013.

[71] Mathworks, Natick, MA, USA. MATLAB, Version R2009a. [Online]. Available: http://www.mathworks.com/

[72] D. I. L. de Villiers, "Private communications," August 2014.

[73] W. D. Burnside and C. Chuang, "An aperture-matched horn design," *IEEE Trans. Antennas Propag.*, vol. 30, no. 4, pp. 790–796, July 1982.

[74] D. S. Prinsloo, "Characterisation of L-band differential low noise amplifiers," Ph.D. dissertation, Stellenbosch University, 2011.

[75] D. I. L. de Villiers and R. Lehmensiek, "Rapid calculation of antenna noise temperature in offset gregorian reflector systems," *IEEE Trans. Antennas Propag.*, Accepted.

[76] S. Weinreb, A. Akgiray, and D. Russell, "Wideband feeds and low noise amplifiers for large arrays," in *General Assembly and Scientific Symposium (URSI)*, August 2011, pp. 1–3.

[77] N. Wadefalk, P.-S. Kildal, and H. Zirath, "A low noise integrated 0.3-16 GHz differential amplifier for balanced ultra wideband antennas," *IEEE Compound Semiconductor Integrated Circuit Symposium (CSICS)*, pp. 1–4, Oct 2010.

[78] J. C. Bardin and S. Weinreb, "A DC-4 GHz 270Ω differential SiGe low-noise amplifier for cryogenic applications," in *European Microwave Integrated Circuits Conference (EuMIC) 2010*, sept. 2010, pp. 186 –189.

Appendix A

Prototype Dimensions

Table A.1: The ridge profile geometry in the flared section of the QRFH prototype.

z-axis	y-axis
0	1.25
4	1.28499
8	1.30035
12	1.31942
16	1.34226
20	1.36555
24	1.39277
28	1.42404
32	1.46294
36	1.50275
40	1.55057
44	1.63465
48	1.78037
52	1.96795
56	2.17027
60	2.37402
64	2.58009
68	2.80781
72	3.09233
76	3.49724
80	4.04113
84	4.69882
88	5.49229

z-axis	y-axis
92	6.47933
96	7.73362
100	9.28881
104	11.1603
108	13.3245
112	15.7487
116	18.5935
120	22.1684
124	26.541
128	30.7594
132	35.476
136	41.0134
140	46.877
144	53.4537
148	61.2215
152	70.9574
155	80.255
156	83.8388
157	87.7057
158	91.827
159	96.0473
160	103.2